1-1-2009

A comparison of iddingsite alteration in two terrestrial basalts and the ALHA 77005 martian meteorite using Raman spectroscopy and electron microprobe analyses.

Karla Kuebler
Washington University in St. Louis

Recommended Citation

Kuebler, Karla, "A comparison of iddingsite alteration in two terrestrial basalts and the ALHA 77005 martian meteorite using Raman spectroscopy and electron microprobe analyses." (2009). *All Theses and Dissertations (ETDs)*. 926.
https://openscholarship.wustl.edu/etd/926

WASHINGTON UNIVERSITY

Department of Earth and Planetary Sciences

A COMPARISON OF IDDINGSITE ALTERATION IN TWO TERRESTRIAL BASALTS AND THE ALHA 77005 MARTIAN METEORITE USING RAMAN SPECTROSCOPY AND ELECTRON MICROPROBE ANALYSES.

by

Karla Elizabeth Kuebler

A thesis presented to the
Graduate School of Arts and Sciences
of Washington University in
partial fulfillment of the
requirements for the
degree of Masters of Arts

December 2009

St. Louis, Missouri

Acknowledgements. Many thanks to the members of the Planetary Surface Materials Research Group at Washington University: the late Dr. Larry Haskin, Dr. Brad Jolliff, Dr. Randy Korotev, Dr. Alian Wang, and Dr. Ryan Zeigler, who began his graduate studies while I was employed as the Raman Specialist and graduated just as I returned to my studies. It was with this research group that I regained the confidence I needed in myself to return to school. Many thanks also go to Dr. Bob Dymek for his guidance and infallible faith in me.

I would also like to recognize the LPI and Allan Treiman for supporting my research during the summer of 2006 and to JSC for the use of their facilities and for access to the Antarctic meteorite collection. Additional thanks go to Allan Treiman for analyzing the alteration products in Lunar Crater and Mauna Kea sample 16J-30 by Synchrotron XRD. This research was supported in part by grant NNX07AQ34G (Mars Fundamental Research Program) to Dr. Brad Jolliff.

Table of Contents. Page

Table of Contents (continued). Page

List of Tables.

List of Figures.

Figure 10. Standard spectra of a set of silicate minerals with different degrees of polymerization of SiO_4 tetrahedra, used to estimate the degree of polymerization of my “polymerized” phase.

Figure 11a. Peak positions of the Lunar Crater olivine spectra from Raman traverses 1-3 plotted on the olivine calibration curve of Kuebler et al. (2006), data points scatter away from the olivine curve, demonstrating a change in the olivine crystal structure with alteration.

Figure 11b. Peak positions of the Lunar Crater olivine spectra from Raman traverses 9-11 (same location as traverse 1-3 but with thin section rotated 90 degrees relative to laser) plotted on the calibration curve; data points scatter in different direction than observed in the original three traverses.

Figure 12. Plot of wt % FeO, MgO, Al_2O_3, CaO, and MnO from the Lunar Crater EMP traverses against wt % SiO_2.

Figure 13. Reflected light image showing the location of Raman traverse 5 across an olivine in the Mauna Kea sample with a stack of spectra showing the observed changes across the alteration front.

Figure 14. Comparison of the Raman spectra of the alteration phases in the Lunar Crater and Mauna Kea samples.

Figure 15. Olivine peak positions from manual traverse 5 on the Mauna Kea sample plotted on the calibration curve. These data points do not scatter away from the olivine calibration curve as much, suggesting that the crystal structure of this olivine suffered relatively little modification during alteration.

Figure 16. Plot of wt % FeO, MgO, Al_2O_3, CaO, and MnO from the Mauna Kea EMP traverses against wt % SiO_2.

Figure 17. Reflected light image showing the location of Raman traverse 1 across an olivine in the ALHA 77005,51 thin section with a stack of spectra showing the observed changes across the alteration front.

Figure 18. Comparison of the Raman spectra of the jarosite in the ALHA 77005 olivine and chromite to two natural terrestrial jarosites and one synthetic jarosite.

Abstract.

The objective of this study is to document the secondary mineral assemblages in two occurrences of terrestrial iddingsite and compare these with the iddingsite in the ALHA 77005 martian meteorite (a lherzolitic shergottite). Short laser Raman spectroscopic traverses (hundreds of µm long) across olivine alteration fronts provide information about changes in the mineral assemblage with alteration. Data from the Raman traverses are combined with data from electron microprobe traverses at the same locations to provide information regarding element mobility near the zones of alteration and to confirm mineral identifications made by Raman spectroscopy. This information is used along with petrographic observations to constrain the conditions of alteration on Mars and deliberate on the environments and modes of alteration.

Although the iddingsite of each sample appears similar in transmitted light, petrographic observations indicate different settings of formation. Raman spectra indicate the presence of different iron oxides or hydroxides in each and the terrestrial samples show different element mobility trends than ALHA 77005 suggesting a difference in the chemical composition of the altering fluids.

Introduction and Purpose for Research.

Recent surface investigations of Mars, such as by the Mars Exploration Rovers (MER), have focused on the acquisition of bulk rock and soil spectra and their chemical compositions, from which mineral speciation is inferred. Particular interest is placed on the identification of primary minerals in association with their secondary alteration products because these help constrain reaction pathways and the physical conditions of past aqueous activity (Wang et al., 1999). Secondary assemblages in the martian meteorites provide constraints for interpreting remote data but their use is complicated by the need to distinguish martian alteration products from potential terrestrial contaminants (Smith and Steele, 1983, 1984; Gooding, 1992; Bridges et al., 2001). Many of the secondary materials in the martian meteorites are hosted by olivine so the alteration products of this mineral are of special interest (Burns, 1993; Delvigne, 1979, 1998; Tosca, 2004; Stopar et al., 2007). Olivine is a common basaltic mineral that occurs in outcrops and soils on Mars and readily alters in aqueous environments because it consists of isolated SiO_4 tetrahedra bonded by cations that are easily oxidized (Fe^{2+}) or mobilized in solution (Mg^{2+}) (Delvigne et al., 1979). The olivine at Gusev and Meridiani Planum have estimated compositions of Fo_{50-60} by Mössbauer (Morris et al., 2004), Fo_{51-55} by norm calculation (McSween et al., 2004) and Fo_{36-60} by APXS (Christensen et al., 2004a and b).

A critical assessment of the climatic history of Mars depends on our ability to merge the evidence of the martian hydrosphere present in the secondary assemblages of the martian meteorites with that of regional (MER, Pathfinder, and Viking) and global data sets, such as those from the Compact Reconnaissance Imaging Spectrometer for Mars (CRISM); the Observatoire pour la Mineralogie, l'Eau, les Glaces et l'Activité (OMEGA); and the Mars Global Surveyor (MGS-TES). The suites of known martian meteorites are mafic and most are relatively unaltered but a few contain jarosite, Elephant Moraine (EETA) 79001 and Allan Hills (ALHA) 84001 contain carbonate, and phyllosilicates occur in the Nakhlites. A summary of the secondary minerals previously reported to occur in Antarctic martian meteorites and their presently accepted origin (terrestrial or martian) is provided in Table 1 of Kuebler et al. (2007; but see also Meyer, 2003).

Regarding the global MGS-TES data set, neither Surface types I or II contain much olivine (< 5%) and both were modeled with phyllosilicate abundances below the detection limit (15 %, Bandfield et al., 2000). Surface types I and II are both inferred to be plagioclase and pyroxene rich, but Surface type II is also suggested to contain a K-rich obsidian glass. The use of silica in the Bandfield et al. (2000) models followed from the conclusion that the Pathfinder "andesite" compositions result from a siliceous desert-varnish on the basalt cobbles at the landing site. More recent reports, however, invoke widespread aqueous alteration and the presence of phyllosilicates (Wyatt and McSween, 2002; Poulet et al., 2005; Bibring et al., 2005, 2007). Korotev (2005), who notes that we only recognized the lunar meteorites after we had the Apollo samples in hand, describes a thought experiment regarding what misconceptions we might have had of the global Clementine and Lunar Prospector data sets if we had not had the Apollo samples to provide a "ground truth" with which to calibrate the data sets (i.e., in the order that the martian data sets have been acquired), and are considerations to keep in mind. There are no known ‘regolith breccias’ among the suite of martian meteorites, whereas these dominate the suite of known lunar meteorites (Korotev, 2005), suggesting that there may be a sample bias during the ejection of the meteorites from Mars or in their delivery to (or recognition) on Earth (Warren, 1994).

Most research on Mars’ secondary mineralogy is presently focused on sulfates and phyllosilicates. Jarosite [$KFe_3^{3+}(SO_4)_2(OH)_6$] peaks are observed in the Mössbauer spectra of outcrops on Mars and the presence of kieserite [$MgSO_4 \cdot H_2O$] inferred from chemical data (Alpha Particle X-Ray Spectrometer, APXS). Hurowitz and McLennan (2007) note that chemical variation among martian surface samples (MER data) “mimic” primary igneous variation but recognize that these analyses include sulfate- and Fe-oxide rich soils, and that Fe-sulfides have not been identified in the primary assemblages (but are present in the martian meteorites). Mössbauer and APXS data from both MER landing sites indicate an inverse correlation in the amount of Fe occurring in olivine vs. that in nanophase oxides, and also with the SO_3 content (Klingelhöfer et al., 2004).

The identification of jarosite and other sulfate minerals at the MER landing sites has renewed an interest in the potential martian origin of the sulfates in the Shergottite-Nakhlite-Chassignite (SNC) meteorites (Papike et al. 2006a, 2006b; Fries et al., 2006; Treiman, 2006). Jarosite has been reported to occur in the lherzolitic shergottites ALHA 77005 and Yamato (Y) 793605 and in the Miller Range (MIL) 03346 nakhlite (Smith and Steele, 1983, 1984; Mittlefehldt et al., 1997; Kuebler et al., 2007; Fries et al., 2006) but its martian origin (as opposed to an Antarctic origin; see Gooding 1984; Wentworth and Gooding 1993; and Wentworth et al., 2005) has yet to be firmly established. Hydrous phyllosilicates are of interest because these occur in the nakhlites and may yield clues to the martian hydrosphere (Treiman, 1993, 2004). Mg-Fe smectites are suggested to occur in the Nili/Syrtis area, Al-rich species in Mawrth Vallis (montmorillonite or chlorite), and kaolinite (implying low levels of leaching) is tentatively suggested to occur in a few locations (Poulet et al., 2005; Bibring et al., 2005, 2007).

Methods.

For this study, laser Raman spectroscopy (LRS) and electron microprobe (EMP) imaging and spot analyses were made on polished thin or thick sections. All Raman spectra were collected with a HoloLab 5000® spectrometer (Kaiser Optical Systems, Inc.) using a 532.3 nm line of a frequency-doubled Nd:YAG laser, unpolarized at the sample, with a 6 µm condensed beam as the excitation source. The automated stage of the attached microscope is capable of taking steps smaller than 1 µm and is used to make 'manual' traverses on the sample. Manual traverses permit the analyst to focus on the sample as frequently as needed (as opposed to automated traverses that only permit the user to focus on the sample once). The absolute wavelength scale of the CCD camera was calibrated using the standard emission lines of a Ne arc lamp and a cubic spline routine in the Holograms® software used to smooth the spectrum and fit it with a 3rd order polynomial. The resulting calibration curve has a standard deviation of 0.003 nm/pixel. The absolute frequency of the Nd:YAG laser showed slight daily variations, ±1.6 cm^{-1}, over the time frame of data collection but was stable for several months at a time so the olivine peak positions were corrected according to the Si wafer's deviation from a standard value of 520.5 cm^{-1}. Spectral resolution (peak separation) of the CCD camera is 3 pixels or 6.2 cm^{-1}.

Most spectra were acquired using a 20x long-working distance objective (0.4 NA) and a low laser power (≤ 6.0 mW at the sample) because of the potential for oxidizing components of the alteration phases (De Faria, 1997; Wang et al. 2004). Some samples were analyzed under a dry N_2 purge to provide additional protection from oxidation (Table 1a). Spectral accumulation times varied from 50 to 100 seconds. Olivine doublets and spectral alteration features were curve-fit using a least squares fitting subroutine of the Grams software package with a mixed Gaussian-Lorentzian peak shape and linear baseline. The constraint-free iteration option in this subroutine was used for fitting all parameters until convergence or a minimum was attained. Table 1a lists the samples and parameters used to collect each Raman traverse.

Chemical compositions of the altered terrestrial samples were measured with a JEOL 733 electron microprobe at Washington University. Electron microprobe (EMP) data on thin sections ,51 and ,34 of ALHA 77005 were collected using the Cameca SX100 at the Johnson Space Center during the summer of 2006. The accelerating voltage, beam current and spot size used for the terrestrial samples were 15 kV, ~30 nA, and 1 µm, respectively. The same accelerating voltage was used for ALHA 77005 but with a lower beam current and larger spot size, 10-20 nA and 5 µm, to limit the amount of beam damage experienced by the martian alteration products, which may contain volatiles. All quantitative analyses used a combination of silicate and oxide standards. More elements (Na, K, Ni, P, S, F, and Cl) were analyzed in ALHA 77005 in order to accommodate the presence of elements recognized by prior studies (Smith and Steele, 1983, 1984). X-ray matrix effects were corrected using ZAF methods incorporated into the JEOL Probe-for-Windows control software on the JEOL microprobe at WU whereas a PAP correction routine was applied on the Cameca SX100 at JSC (Armstrong, 1988; Pouchou and Pichior, 1991). Table 1b summarizes the parameters used during the collection of each microprobe traverse.

Studying weathering reactions with Laser Raman and EMP traverses.

Raman spectral patterns provide information regarding crystal structure, crystallinity (regularity of the long-range crystal structure), and composition. Raman peaks are produced by molecular vibrations specific to the crystal structure and bonding environment so any change in the olivine structure due to alteration will be apparent in the spectra. By studying the degradation of the olivine spectral pattern in conjunction with the appearance and occurrence of alteration phases we can constrain the conditions present during alteration (T, P, fO_2, fluid composition). In addition, Raman spectra of hydrated minerals have peaks at high Raman shifts due to OH and H_2O bonds, so the presence of waters of hydration are directly detected, not inferred (Wang et al., 1999).

Electron microprobe analyses provide information on composition, which permit the evaluation of element mobility and place constraints on solution chemistry. The depth of penetration of the microprobe electron beam is shallower than that of the Raman laser so the difference in the sample volumes being analyzed by the two techniques results from the diameter of the microprobe beam and the depth of penetration of the Raman laser. The depth to which the Raman laser penetrates the sample varies with the opacity of the material being analyzed and is generally deeper than that of the focused EMP electron beam. A larger spot size was used during the EMP analysis of the ALHA 77005 alteration products so the volumes analyzed by the two techniques are most alike in this sample. The alteration products in all three samples are fine-grained intergrowths so the microprobe analyses in the alteration represent a mixture of phases. Variations in the major element compositions are used to make inferences regarding the phases present.

I used 1-2 μm steps in relatively short Raman traverses (total lengths of tens to hundreds of micrometers) to study the reactions of olivine alteration in all three samples, maintaining an optimal focus on the upper surface of the thin section throughout the traverses. The effective Raman sample volume of the alteration phases is generally small, because they are not optically transparent. The tight spacing of data points and small sample volumes provide good spatial control on the apparent reaction inside the alteration but the secondary phases are poorly crystalline and have weak Raman signals. It should be noted that standard thin sections have discrete thicknesses, ~30 μm, and should not be thought of as being infinitely thin; reflected and transmitted light images repeatedly demonstrate differences in the materials visible at the surface of the thin sections and at depth. The olivine is transparent so the spectra outside the alteration front may sample phases at depth in the thin section (including epoxy, so most of the Raman analyses were made on thick sections rather than thin sections). The olivine are more crystalline than the alteration products so the Raman spectra acquired outside of the alteration front are stronger.

Throughout this paper, changes in the Raman spectra are described as the traverses pass from unaltered olivine into patches of alteration. Spectral changes are related to the chemical trends established by electron microprobe analyses (EMPA) at the same locations. Cross cutting (petrographic) relationships constrain the timing of alteration events (i.e., multiple episodes of alteration, pre-terrestrial from potentially Antarctic alteration).

The Raman spectrum of olivine and the Fo-Fa olivine calibration.

Olivine is an orthosilicate of orthorhombic *Pbnm* space group with a complete solid solution between the Fe and Mg end-members (Papike, 1987; Khisina et al., 1995). I use the same spectral regions as Kuebler et al. (2006) to describe changes in the olivine spectra (see Fig. 1): <400 cm^{-1}, 400 – 800 cm^{-1}, and 800 – 1100 cm^{-1}. The dominant feature of the olivine spectrum is a doublet in the 800 – 1100 cm^{-1} region with peaks near 820 and 850 cm^{-1} (referred to as DB1 and DB2 by Kuebler et al., 2006) that result from the coupled symmetric (v_1) and asymmetric (v_3) stretching vibrations of SiO_4 tetrahedra (Pâques-Ledent and Tarte, 1973; Piriou and McMillan, 1983; Chopelas, 1991). Peaks in the 400 – 800 cm^{-1} region are mainly from SiO_4 internal bending vibrational modes, whereas peaks below 400 cm^{-1} arise from lattice modes: rotations and translations of SiO_4 units and translations of octahedral cations in the crystal lattice (Chopelas, 1991). Peak positions of the olivine doublet vary with composition, occurring near 815 cm^{-1} and 838 cm^{-1} for fayalite and 825 cm^{-1} and 857 cm^{-1} for forsterite, as reported by Kuebler et al. (2006). The increase in peak-position with increasing Fo content is linked to the change in cation mass between the end-members (Mg vs. Fe), the change in the polyhedral volume of the octahedral sites, and the degree of coupling between the SiO_4 symmetric and asymmetric stretching vibrational modes (Chopelas, 1991; Kuebler et al., 2006).

Kuebler et al. (2006) presented a calibration for estimating olivine compositions from the peak positions of this doublet and discussed its accuracy with low signal-to-noise data. Alteration degrades the olivine crystal structure, influences the spectral quality of the olivine doublet (peak resolution and peak height/width ratios), and may also hinder our ability to determine olivine compositions from the Raman spectra accurately. Observations of olivine peak degradation through a sequence of spectra in conjunction with the appearance of plausible secondary phases provide a useful indication of alteration.

The laser used in this study is only partially polarized after passing through the delivery optical fiber so I cannot discern the relative degrees of influence of crystal orientation and alteration on the peak heights of the doublet. However, the data from the Lunar Crater sample are sufficient to demonstrate that alteration preferentially influences the 820 cm^{-1} peak in this sample (the 820 cm^{-1} peak degrades faster than the 850 cm^{-1} peak regardless of which peak dominates the spectra in the unaltered olivine). The 820 cm^{-1} peak appears to have a stronger M1 cation contribution (Kuebler et al., 2006), suggesting that polarized Raman spectra on oriented crystals would be useful for studying the cation site-specific effects of alteration on the olivine structure.

Olivine alteration products – interpreting the local alteration environment.

Olivine is a common primary mineral occurring in mafic and ultramafic igneous rocks whose terrestrial alteration assemblages are indicative of the environment of alteration, be it deuteric, hydrothermal, surface, or metamorphic. Iddingsite is narrowly defined as the product of deuteric alteration (reaction with magmatic waters that separate from the melt upon depressurization of the magma en route to the surface; Edwards, 1938; Gay and LeMaitre, 1961; Sheppard, 1962; Delvigne et al., 1979; Eggleton, 1984; Eggleton et al., 1987; and Smith et al., 1987) but has also been used to describe surface alteration. According to Delvigne et al. (1979), surface alteration products include iron hydroxide and phyllosilicate (smectite) intergrowths where drainage is good and the water/rock ratio high, and infer nontronite or other clays to form where drainage is poor and the water/rock ratio low. Serpentine and talc commonly occur with magnetite as the products of metamorphic reactions. Multiple generations of alteration are commonly present and may complicate their interpretation. For a complete discussion of olivine alteration refer to the review paper of Delvigne et al. (1979) or his Atlas of Micromorphology of Mineral Alteration and Weathering (Delvigne, 1998). I compare the alteration products in our samples to select images from the Atlas. Figure 2 shows reference spectra of each of the phases identified in this study or suggested to be present by previous studies.

Olivine alteration products commonly occur as fine-grained intergrowths whose components are frequently only poorly constrained and ill defined. In particular, the term “iddingsite” has been used as a catchall phrase for the reddish-brown alteration products of olivine. Three of our samples contain reddish-brown alteration products that appear similar in plane-polarized light (PPL) but differ in mode of occurrence. As mentioned above, some authors ascribe a more specific mode of occurrence, that of deuteric alteration by magmatic waters (Edwards, 1938; Gay and LeMaitre, 1961; Sheppard, 1962). Only one of our samples, Lunar

Crater, fits this description of iddingsite formation (see petrographic descriptions below for justification). An alternative mechanism infers iddingsitization to occur in-situ as a magma crystallizes, that the concentrations of volatiles (H_2O, HCl, and H_2SO_4) in the residual melt increase as they are excluded from the growing crystals. When the melt becomes acidic enough, the volatiles begin to alter the primary minerals (McSween, personal communication). The mode of occurrence of the ALHA 77005 iddingsite fits this definition of iddingsite whereas that of the Mauna Kea sample suggests surface alteration. Much of the confusion between deuteric and surface alteration products is due to their optical similarity compounded by the frequent superposition of these alteration processes (Baker and Haggerty, 1967; Delvigne et al., 1979). Typically, the alteration products of both processes are poorly crystalline intergrowths of iron oxides (goethite, hematite) and phyllosilicates (smectites/saponite) that may also contain amorphous components (Sun, 1957; Wilshire, 1958; Delvigne et al., 1979; Eggleton, 1984; Eggleton et al., 1987; Smith et al., 1987). The amount of smectite produced is variable, abundant in some samples but lacking in others (Delvigne et al., 1979).

Jarosite-group minerals [$KFe_3(SO_4)_2(OH)_6$] are common secondary minerals in weathering environments and are highly variable in composition; K is commonly replaced by Na, but can also be replaced by H_3O (hydronium substitution is more common in jarosite than in alunite, the Al^{3+} end-member, and is usually inferred where chemical analyses suggest a deficiency in cations and an excess of H_2O; Ripmeester et al., 1986). Jarosite forms most commonly as a supergene product of Fe-sulfide oxidation in acidic settings, is less common in hydrothermal settings, and only rarely occurs as a hypogene mineral, even in S-rich volcanic settings (Stoffregen et al., 2000; Dutrizac and Jambor, 2000). Jarosite formation requires a lower pH and more oxidizing conditions than alunite and is therefore less common. Supergene or hypogene alunite formed at or below the water table may be replaced by jarosite if the groundwater becomes more acidic or oxidizing (e.g., when a drop in the water table exposes sulfides to weathering; Stoffregen et al., 2000). Jarosite and goethite are reported to coexist in terrestrial gossan deposits (Scott, 1987).

In the following section, I describe the petrographic differences of the iddingsite in these samples, particularly in the mode of occurrence, and provide as much geologic context as possible for the alteration setting of the terrestrial samples.

Geologic setting and sample descriptions of alteration.

Lunar Crater, NV. This sample is a vesicular and porphyritic basalt collected from a pavement in the Lunar Crater Volcanic Field (LCVF), Nevada; a 10x100 km alkali basalt field located in the center of the Great Basin, an internally drained region that includes most of Nevada and portions of Utah (see Israel, 1996, for the sample location 250 km north of Las Vegas; Bergman, 1984; Frazier and Schwimmer, 1987). The region is underlain by Paleozoic sediments and intermediate to felsic Miocene to Oligocene volcanics. The first basalt flows formed during the late Pliocene (5.7 Ma) and volcanic activity migrated north through time, with the most recent flows erupted during the Holocene (10-15 ka; Bergman, 1984; Scott and Trask, 1971). The region became increasingly arid during the Pliocene with the uplift of the adjacent Sierra Nevada Range and marked by the onset of desert conditions. Figure 9.11 of Eaton (1980) depict the thermally driven groundwater circulation beneath the Basin & Range (in the upper 8-15 km of the crust); such “vigorous” hydrothermal circulation is said to be responsible for the mineral deposits of Nevada (Frazier and Schwimmer, 1987).

The LCVF is relatively isolated in comparison to other Quaternary volcanic fields and contains some of the youngest alkali basalts in the Great Basin. The older (Pliocene) lavas have high $^{87}Sr/^{86}Sr$ ratios, lack ultramafic nodules, and have a restricted suite of phenocrysts; these are suggested to have ascended to the surface at a slower rate and to have interacted more extensively with the country rocks than the Holocene flows in the north. The younger lavas have lower $^{87}Sr/^{86}Sr$ ratios, are the most silica undersaturated, and have a different normative chemistry (Bergman, 1984). These flows contain large single-crystal olivine megacrysts and a more varied suite of xenoliths (Bergman, 1984) that derive from the lower crust and upper mantle. Some megacrysts record equilibrium temperatures of in excess of 1270°C, which Smith (2000) suggest to be samples of a plume or the asthenosphere. These high equilibration temperatures are based on the Ca-in-orthopyroxene thermobarometer of Brey and Kohler (1990) and on the high Mg content of the olivine, $Fo_{86\text{-}91}$, reported in their paper. The olivine compositions measured in our sample are more ferroan, however, and average ~Fo_{58}. Smith (1990) suggests that these flows formed by low to moderate degrees of partial melting (6-20%, assuming a pyrolitic to lherzolitic upper mantle), ascended to the surface rapidly (>50 cm/sec), and underwent relatively little differentiation (Spera, 1980 in Bergman, 1984).

The LCVF is also notable in that it coincides with the "Eureka Low," a region of anomalously low heat flow, which Sass et al. (1971) attributed to circulating ground water but could indicate a deeper source of water (hydration of the asthenosphere by the melting of a subducted slab or spreading center). Ultramafic nodules in these flows contain CO_2 – rich fluid inclusions whose compositions and densities suggest entrapment of oxidized fluids at moderate to high pressures ("volatile saturation via primary and/or retrograde boiling of basaltic magmas in the lower crust and upper mantle," Bergman, 1984).

Olivine throughout the Lunar Crater sample are altered along their edges and fractures, and fit the narrow definition of iddingsite alteration formed by deuteric waters (Fig. 3). These reddish-brown alteration products (yellowish-brown at the fringes in thick section) have irregular boundaries and are optically homogeneous (uniform extinction under cross-polarized light). In addition, the extinction angle of these materials parallels that of the host olivine, implying that the oxygen network of the goethite is inherited from the olivine (Brown and Stephen, 1959; Delvigne, 1979). The alteration products are uniformly bright in reflected light (brightness does not vary with respect to the degree of alteration, suggests that an iron oxide or oxyhydroxide is present throughout the alteration) and are also isovolumetric with the host olivine. Green alteration products are also present in the more ferroan groundmass olivine and are presumably the unoxidized equivalent of the iddingsite (Baker and Haggerty, 1967). I focus on the red alteration products in one large phenocryst (~5 mm in its longest dimension); smaller grains that contain both colors of alteration were analyzed but not studied in any great detail. The appearance of the Lunar Crater "iddingsite" is similar to that featured in plates 104 and 105 of Delvigne's Atlas.

The groundmass pyroxene and feldspar phenocrysts in this sample are relatively unaltered so it is inferred that this sample suffered relatively little surface alteration during its residence in the pavement that it was collected from. Pavements reduce surface roughness and decrease permeability so a greater proportion of the local precipitation occurs as run-off (Wells et al., 1985), inhibiting surface alteration. Coarse-grained calcite and disordered carbon (Fig. 4, identified by Raman spectroscopy) are present in amygdules but their occurrences are not spatially correlated with the iddingsite and were probably deposited by post-magmatic aqueous fluids shortly after emplacement (Rakovan, 2005). Fine-grained clays may also be present in the amygdules but the calcite is fluorescent and inhibits the detection of other phases.

Mauna Kea, HI. The Hawaiian samples were collected from the Laupahoehoe flows along the Observatory Road on the southern flank of Mauna Kea. These are 4-65 ka post-shield volcanic flows. Sample 16G-30 is from one of the younger Laupahoehoe flows emanating from Puu Keonehehee and 16J-30 is from one of the older flows 100 m east of the 16G collection site (see Table 1 of Kristall, 2000, for locations). The summit of the volcano is cold and dry. Low temperatures in the winter average around -4 °C and summer highs near 10 °C with about 15 cm of precipitation, usually in the form of snow (Canada France Hawaii Telescope online instruction manual, 2009). Eruption of these flows was separated by the Makanaka glacial episode 13 ka (Wolfe et al., 1997). Both are highly vesicular basalts but 16G1-30 is more altered than 16J-30. 16G1-30 contains fine-grained calcite, clay (montmorillonite), and hydrous (opaline) silica in its vesicles (see Fig. 5; compositions reported in Table 7 of Kristall, 2000) while the groundmass of 16J-30 contains unaltered brown volcanic glass and abundant magnetite grains in the groundmass. Altered olivine grains only occur near the red, oxidized exteriors of these two samples (within 1 cm of the edge), probably the undersides that sat and were exposed to moisture in the Mauna Kea soil. The degree of olivine alteration is highly variable from grain to grain, ranging from thin rims to almost complete replacement. In transmitted light, the Mauna Kea alteration appears similar to that of Lunar Crater in color, extinction, and morphology (Fig. 6). The alteration occurs along edges and fractures in olivine, has irregular boundaries and goes extinct uniformly. However, in the grains that exhibit well-developed alteration, the alteration is *not* uniformly bright in reflected light and is only bright in localized areas. Hematite (or maghemite) is present as grain coatings in the altered exterior of the sample as seen in reflected light, and may be the locally reflective material in the olivine alteration product of this sample. Small olivine grains with various degrees of alteration in the oxidized rims were analyzed as well as an unaltered olivine in the middle of each thin section. These occurrences are similar to plates 201 and 202 in the Delvigne Atlas.

<u>ALHA 77005.</u> ALHA 77005 is a lherzolitic shergottite consisting of two lithologies: light and dark. The olivine in both lithologies are light beige to brown in plane-polarized light, though not necessarily uniform in color (Fig. 7, Treiman et al., 2007), and are annealed colorless near impact melt veins, indicating that the brown alteration products are martian (Smith and Steele, 1983). The brown coloration is attributed to the presence of Fe^{3+} in the olivine crystal structure (Ostertag et al., 1984; Treiman et al., 2007). The brown olivine alteration is not preferentially altered along crosscutting fractures and these olivines are poikilitically enclosed by orthopyroxene, so it is likely that the brown color formed just before or during the near-surface solidification of the magma.

Four thin sections of ALHA 77005 were examined petrographically while at JSC (,34; ,46; ,51; and ,52) but only two of these (,34 and ,51) contained significant alteration features beyond the presence of the brown olivine (patchy alteration and later jarosite); and were selected for further study. The patchy alteration products are uncommon in the meteorite but appear to occur only in olivine poikilitically enclosed by orthopyroxene (i.e., in the light lithology). Likewise, the jarosite, which is relatively abundant in these two thin sections, is uncommon in the rest of the meteorite and appears to be rare among the martian meteorites (see Table 1 of Kuebler et al., 2007). The later jarosite crosscuts most of the phases in these two thin sections precluding a reflected light comparison with the patchy alteration products of the two terrestrial samples. The chromite in these thin sections are altered by the jarosite also. Both of these thin sections were cut from potted butt ,13 which Smith and Steele (1984) indicate is from the interior of the meteorite. These iddingsite occurrences are similar to plates 246 and 247 in the Delvigne Atlas (see Fig. 7).

The secondary K-Fe sulfates in thin sections ,51 and ,34 were reported to be potassium jarosite [$KFe_3(SO_4)_2(OH)_6$] and quenstedtite [$Fe_2(H_2O)_{10}(SO_4)_3$] by Smith and Steele (1983). These phases were initially suggested to be pre-terrestrial because this meteorite contains little H_2O and because its trace-element composition appears to be unaffected by weathering (Marvin, 1980; Biswas et al.; 1980). The martian status of these phases was later called into question after sulfates were reported to occur in the fusion crusts of other Allan Hills meteorites (Gooding, 1981) and because the sulfates clearly post-date the other alteration products. Similar materials coat fracture surfaces of the meteorite so a terrestrial origin was deemed likely (Smith and Steele, 1984). Discussion regarding the martian vs. terrestrial provenance of the jarosite has re-opened as a result of: (1) the discovery of jarosite on Mars by the MER Rovers and (2) the suggestion that the jarosite in the fusion crust and lining fractures in the meteorite may have been remobilized from elsewhere in the meteorite during its passage through the terrestrial atmosphere. I observed one chromite with an altered rim of jarosite enclosed in and reacting with a clear, unaltered feldspathic glass in thin section ,51 that suggests the jarosite is martian (see Fig. 8; i.e., if the jarosite was an Antarctic alteration feature the glass would be altered too). The lack of K-bearing minerals within the primary assemblage may stipulate a martian origin (Kuebler et al., 2007), assuming that little K and S are available in the brines of the encapsulating Antarctic ice (some sulfate ions may be carried inland from ocean spray). Secondary free silica, goethite, a low–Al phyllosilicate, and Mg–Fe phosphates are also reported to occur in this meteorite (Wentworth and Gooding, 1993; Treiman et al., 2006).

Sample analysis.

In this manuscript, I describe the effects of alteration along traverses as they pass from unaltered olivine across the alteration front and into the alteration products (as inferred from reflected light observations), paying attention to where each alteration phase appears and the distance over which the reaction appears to take place. These data are used to constrain the physical processes of alteration. Raman spectra obtained within a given patch of alteration are generally similar throughout, but the peak positions of the poorly crystallized materials can be highly variable. Because of this inherent variability, less effort is devoted to describing changes in the spectral patterns inside the alteration. Raman peaks of the alteration phases are usually less noisy where the alteration is better developed relative to those acquired at the alteration front.

For each sample, I present the results of the Raman analyses first, beginning with a general description of the alteration phases occurring in, or associated with, the olivine and then describe the spectral changes across the alteration front of one representative traverse (generally in the main text and in greater detail in the appendices). Outstanding issues encountered in the Raman analysis are addressed in the appendices (App. 1: relative influence of alteration versus crystal orientation on changes in peak position, App. 2: the presence of alteration at depth in the thin section and the apparent distance over which the alteration reactions occur). The Raman results are followed by a presentation of the corresponding electron microprobe analyses with a discussion of element mobility and an assessment of the mineral identifications where the Raman results are tentative or ambiguous.

<u>Lunar Crater, NV.</u> *Raman analysis.* A sequence of spectra from traverse 2 across an olivine alteration front in the Lunar Crater alkali basalt is shown in Figure 9 with a reflected light image of the location where the traverse was collected. Three groups of peaks are distinguished: the olivine doublet or a “remnant” olivine feature (described below), four peaks attributable to goethite [FeO(OH)], and a “polymerized” silicate phase. Goethite peaks occur at 245, 302, 390 and 478 cm^{-1}, the strongest of which is the ~390 cm^{-1} peak. The polymerized silicate phase has two multi-component spectral features in the 400-800 cm^{-1} and 800-1100 cm^{-1} regions that cannot be attributed to olivine, goethite, saponite, or any other smectite. The polymerized silicate phase in Lunar Crater has a strong, broad feature in the 400-800 cm^{-1} region where $Si\text{-}O_b\text{-}Si$ peaks occur (O_b = bridging oxygen). It is centered at 630 cm^{-1} but has a shoulder near 690 cm^{-1}. A weaker feature is located in the 800-1100 cm^{-1} region where $Si\text{-}O_{nb}$ peaks occur (O_{nb} = non-bridging oxygen), centered at 935 cm^{-1}, usually with a shoulder near 1020 cm^{-1}. This phase is categorized as a polymerized silicate phase (or mixture of phases) according to the correlation of Wang et al. (1994) who related the relative intensities of the $Si\text{-}O_b\text{-}Si$ and $Si\text{-}O_{nb}$ Raman bands to the ratio of O_{nb} to O_b bonds (see Fig. 10). Silicates with $O_{nb} < 2$ have relatively strong Raman Si-

O_b-Si bands in comparison to their Si-O_{nb} bands and the peak positions of the Si-O_{nb} bands increase as the number of O_{nb} bonds decreases (Wang et al., 1994). The stronger 630 cm^{-1} band suggests a degree of polymerization higher than that of pyroxene whereas the peak position of the Si-O_{nb} band suggests an incipient layered structure. These two constraints imply a structure whose degree of polymerization is between that of a double-chain and sheet silicate. The presence of multiple peak components and large peak shifts suggests that the degree of polymerization is variable and that a mixture of phases may be present. No saponite or smectite are apparent in the Lunar Crater alteration products.

Alteration begins as the olivine doublet degrades (broadens and weakens) into a variably developed remnant ~850 cm^{-1} in proximity to, but outside of, the alteration front (I refer to the phase as a remnant when the two olivine peaks can no longer be resolved). The olivine remnant disappears within 10 µm of the inside of the alteration front (see Figure 9). Goethite and "polymerized" peaks appear in the olivine spectra *ahead* of the alteration front in the yellowish-brown fringes (with a possible contribution from alteration at depth in the thin section) but their peaks are weaker than the olivine doublet. Peaks of the goethite and "polymerized" phases only dominate the spectra acquired inside of the alteration. Just inside the alteration front, the peaks of the polymerized phase are strongest but the spectra acquired here are usually noisy with a low signal-to-noise ratio. Peaks of both the goethite and polymerized phases strengthen and are better resolved deeper into the alteration, but the strengthening of the goethite peaks outpaces that of the polymerized phase so that goethite becomes the dominant phase inside the alteration. A broad, weak band in the OH stretching mode region (3400-3800 cm^{-1}) appears in some spectra but its peak positions are too low for goethite. Some spectra acquired just inside the alteration front have high backgrounds that may indicate the presence of a phyllosilicate clay (halloysite was reported to occur in the iddingsite fringes of olivine from the Baynton basalt of Australia by Eggleton, 1984; Eggleton et al., 1987 and I have found that saponite can fluoresce under a green laser), but this is speculation. A search for smectite was made at higher magnification (100X) but none was detected. Hematite peaks occur in some spectra within the alteration but are rare and may represent goethite that has dehydrated. This description of the alteration reaction holds for all of the Raman traverses acquired on the large phenocryst in the Lunar Crater sample.

Several spectral features combine to indicate the alteration of olivine and provide information about the alteration process. When the ~820 and ~850 cm^{-1} peak positions are plotted against each other on the olivine calibration curve of Kuebler et al. (2006) the data points are found to plot off the calibration curve (see Figure 11, green data points represent spectra whose peak height/width ratios are >10). This scattering of data points could be a potentially useful indicator of alteration during in-situ measurements on Mars if the focal quality of the spectra is otherwise known to be good. The coincidence of goethite peaks with the degradation of the olivine doublet reflects the concurrent oxidation of Fe^{2+} whereas the multi-component features near ~630 and ~935 cm^{-1} indicate the presence of an additional phase (or phases) in the reaction. I repeated several of the Lunar Crater traverses with the thin section rotated 90 degrees from its original orientation to gauge the relative effects of orientation and alteration on the degradation of the doublet; these results are discussed in Appendix I.

Microprobe data. The microprobe data across the alteration fronts in the Lunar Crater phenocryst record a loss of MgO and SiO_2 with progressive alteration and compositions that deviate from the Fo-Fa lines as shown in Figure 12. EMP analyses that correlate with the traverse 2 spectra shown in Figure 9 are provided in Table 2. Olivine analyses (those having oxide totals > 97 wt %) were reduced using 4 oxygen atoms per formula unit and indicate the phenocryst to have compositions between Fo_{51-64}. Iddingsite analyses (those having totals less than 97 wt %) were reduced using 3 oxygen atoms per formula unit. Iron in the olivine is assumed to be in the Fe^{2+} state and in the Fe^{3+} state in the iddingsite. Magnesium numbers, Mg # = Mg/(Mg+Fe+Mn), were calculated for all of the analyses and demonstrate the removal of Mg relative to Fe. The microprobe data record little influx of other cations; the oxides of the other cations present in the analyses of the alteration products sum to less than ~2.2 wt % on average, rarely exceed 4.0 wt %, and are less than 7.2 wt % in all analyses. Microprobe analyses do not support the presence of a smectite component which, volumetrically, is a relatively minor component. All analyses acquired within the alteration contain less SiO_2 than the host olivine. Spot analyses taken in the olivine adjacent to the alteration tend to have low totals (between 99.0 and 99.5 wt %) and plots of the major oxides support the inference that material is being mobilized out of the olivine (Fig. 12).

A balanced reaction representing the alteration reaction using an olivine composition that corresponds to our EMP analyses of the starting olivine composition and other constituents to represent the polymerized phase can be written as follows:

$2\ FeMgSiO_4 + 2\ H_2O \rightarrow 2\ FeO(OH) + 2\ SiO_2 + 2\ MgO + H_2$

Because the alteration products are a fine-scale (nm) intergrowth it was impossible to determine an average composition of the polymerized phase; it is represented in the above reaction by its constituents MgO, SiO_2, and H_2. Note that each of the reactants and products are neutral species so that positive and negative charges do not need to be balanced. In each of the samples used, oxidation of the Fe from $Fe^{2+} \rightarrow Fe^{3+}$ is balanced by reduction of hydrogen from H^+ in H_2O to H^0 in H_2.

Mauna Kea. *Raman analysis.* Several olivine grains of various degrees of alteration were studied in the two Mauna Kea samples, from unaltered to almost completely altered. Traverses through alteration in three olivine grains are described in detail in Appendix II, ranging from slightly altered to highly altered. Both the moderately and highly altered grains have alteration whose brightness is variable in reflected light. A sequence of spectra from across an alteration front in the moderately altered olivine of 16J-30 is shown in Figure 13 and briefly described here. In general, the spectral patterns of the alteration products in the Mauna Kea samples are similar to those of Lunar Crater except that the peak positions of the polymerized silicate phase occur at higher Raman shifts, reflecting the more magnesian olivine compositions, and the goethite peaks are lacking (Fig. 14). The $Si\text{-}O_b\text{-}Si$ bands of the polymerized silicate phase in the Mauna Kea samples (in the 400-800 cm^{-1} region) are centered near 640 cm^{-1} with shoulders near 710 cm^{-1}. The weaker, overlapping $Si\text{-}O_{nb}$ features (in the 800-1100 cm^{-1} region) are centered at ~945 cm^{-1} and ~1035 cm^{-1}. Instead of goethite, many spectra have a two broad features below 500 cm^{-1}, centered near ~335 cm^{-1} and 475 cm^{-1} (Fig. 14). These could be the secondary peaks of an Fe-oxide whose primary peak (~670 cm^{-1}) is obscured by the polymerized silicate. A broad peak whose center varies from 1300 to 1360 cm^{-1} is common and suggests hematite (or maghemite). As noted above, hematite (or maghemite) is present as grain coatings near the altered surfaces of the Mauna Kea samples but the quality of the peaks (weak, broad, noisy) imply that it is poorly crystalline.

Degradation of the olivine doublet in the Mauna Kea samples differs from that in Lunar Crater such that the doublet is observed further into the alteration products, up to 30 µm, and only becomes a “remnant” and disappears in proximity to alteration products that are bright in reflected light (Fig. 13). The doublets may even appear sharp where the alteration appears to be well developed (more opaque) in transmitted light (as at the end of traverse 5). When the doublet does degrade into a remnant near the reflective material, it does so over a short distance, within 5-10 µm. Furthermore, the relative ~820 and ~850 cm^{-1} peak heights remain similar as the doublet degrades; neither peak is preferentially affected by the alteration. I did not observe any situations in the Mauna Kea samples where the initially stronger peak degrades more readily than the initially weaker peak as was observed with the 820 cm^{-1} peak in Lunar Crater (described in Appendix I), which suggests that the mechanisms of alteration differ between the two terrestrial basalts and that the Mauna Kea mechanism of alteration does not preferentially influence either cation site. As in the Lunar Crater sample, the peaks of the alteration phases appear in the olivine ahead of the alteration front (in association with alteration at depth in the thin section), and spectra acquired at, or just inside, the alteration front sometimes have high backgrounds.

Unlike the olivine peaks at the Lunar Crater alteration fronts, the curve-fit peak positions of the Mauna Kea olivine largely fall along the olivine calibration curve between Fo_{60} and Fo_{90}. Data from the entire length of traverse 5 are shown in Figure 15. Some scatter is observed to either side of the curve but the data do not spread away from the curve systematically as alteration progresses. This supports the interpretation that alteration has had less of an effect on the olivine crystal structure in these two samples. The same 820 cm^{-1} peak height/width cut-off ratio (= 10) was used to define “good” data points (green in Figs. 11, 15) in the Mauna Kea samples although some of the data points defined as good were acquired behind the alteration front, particularly in traverse 5. The observed spread of the good data points along the calibration curve in Figure 15 can be explained completely by compositional zoning in the host olivine. Scatter of the black dots away from the calibration curve in the Mauna Kea samples may also be due in part to zoning (see the discussion in Kuebler et al., 2006, regarding the degree of zoning and its influence on the breadth of the olivine doublet peaks and their peak positions).

The ~640 and ~710 cm^{-1} peaks of the polymerized phase emerge over a short distance (< 10 µm) across the alteration front in traverse 5 (which appears sharp in both transmitted and reflected light) and imply that the reaction occurs abruptly over a short distance. This is probably true of the reaction fronts in most of the Mauna Kea olivine but because the olivine is more transparent to the laser than the alteration, the alteration is sometimes detected at depth ahead of the alteration front as observed in reflected light. Thus, the spectral traverses sometimes require many spectra for the olivine peaks to disappear and alteration products to dominate the spectra, giving the impression that the reactions are more drawn out (e.g., the reactions at the end of traverse 1 or across the alteration front in traverse 6 – as described in Appendix II).

Microprobe data. Microprobe analyses that correlate with the traverse 5 spectra shown in Figure 13 are provided in Table 3. Without concrete phase identifications from the Mauna Kea alteration, and because the Raman data suggest that the olivine structure persists further into the alteration, all EMP analyses were reduced as olivine using 4 oxygen atoms per formula unit and the Fe^{2+}/Fe^{3+} ratios varied to bring the total cation sum to 3.0. Even though the totals are low, the stoichiometric calculations produced octahedral cation sums >1.98 for all olivine analyses and >1.80 for most iddingsite analyses.

A loss of MgO and SiO_2 with an increase of FeO is also demonstrated from the alteration products in the Mauna Kea olivine (see Fig. 16). These olivine grains are initially more magnesian ($Fo_{63\text{-}83}$) than those of the Lunar Crater sample so the data trend toward an alteration product containing less FeO than goethite, ~70 wt % FeO at 0 wt % SiO_2, consistent with the presence of either hematite or maghemite. As with the Lunar Crater alteration, the Mauna Kea samples show little influx of other elements, the sum of cations other than FeO and MgO is 2.2 wt %, on average, and never exceeds 4.0 wt %. EMP of the Mauna Kea alteration products indicate less SiO_2 than the host olivine and do not support the presence of a smectite component.

A balanced reaction representing the Mauna Kea reaction using an olivine composition that corresponds to my EMP analyses and again using theoretical end member compositions to represent the polymerized phase other constituents can be written as follows:

$4\ Fe_{0.5}Mg_{1.5}SiO_4 + H_2O \rightarrow Fe_2O_3 + 4\ SiO_2 + 6\ MgO + H_2$

ALHA 77005. *Raman analysis.* The ALHA 77005 samples indicate multiple generations of alteration; early alteration products include the brown color of the olivine (predating the injection of impact melt, Smith and Steele, 1983, 1984) and "patchy" olivine alteration materials that resemble those in the Lunar Crater sample. No goethite was detected; instead two broad peaks near 300 and 390 cm^{-1} and another near 720 cm^{-1} suggest the presence of its polymorph, akaganéite (compare spectrum 05260817 in Figure 17 to the standard spectrum shown in Fig. 2). A small peak near 684 cm^{-1} (see spectra 05260817 & 05260818 in Fig. 17) may also belong to akaganéite or to minute inclusions of magnetite (~660 cm^{-1} peak) as observed elsewhere in the brown olivine. Later veins of jarosite cut across the thin section, altering most primary phases and overprinting the patchy alteration. No quenstedtite (suggested to be present by Steele and Smith, 1983) was detected by Raman spectroscopy.

Despite the low laser power (<5.5 mW), the Raman laser left a trace in the jarosite-rich portions of some traverses, suggesting that oxidation occurred and that an N_2 purge should have been used. It is unclear which phase in the alteration was oxidized. An iron oxyhydroxide, akaganéite (an Fe^{3+} plus phase), was detected instead of hematite (what would oxidize to akaganéite?) and jarosite is nominally a Fe^{3+}-bearing mineral (but Fe^{2+} is present in the olivine and Fe^{2+} was required to properly reduce the probe data of the olivine-hosted jarosite and produce the proper cation sums – if all Fe was assumed to be Fe^{3+} the B cation sums jumped into the hundreds; this problem was not encountered with the chromite-hosted jarosite). Elemental sulfur was detected in the Raman spectra of the chromite alteration products and is not the phase being oxidized. I therefore infer that Fe^{2+} is present in the jarosite and that jarosite is the phase that is being oxidized by the Raman laser.

Spectral changes across the alteration fronts in ALHA 77005 are complex because multiple alteration phases are present and because the jarosite spectrum contains several peaks. As shown in Figure 17, the olivine doublets diminish over a distance of about 15 µm and are replaced by a minor jarosite peak at 870 cm^{-1} inside the patchy alteration. The akaganéite is most easily detected near the iddingsite fringes before the jarosite peaks come to dominate the spectra. Weak jarosite peaks appear several spectra ahead of the alteration front but strengthen and sharpen inside the alteration. Because jarosite has a relatively large Raman cross-section this phase dominates most of the spectra acquired inside the alteration making the polymerized phase difficult to detect, it is apparent in a few spectra of one of the traverses, however. Three standard jarosite spectra are shown for comparison in Figure 18 (a Chinese jarosite from A. Wang, an Iconofile pigment sample, and a jarosite sample from Mauna Kea HWMK515 – both from D. Morris and D. Ming; see Ming et al. 1996 for XRD spectrum).

When the olivine peak positions from Raman traverse 1 are plotted on the calibration curve (see Figure 19) a different scattering pattern is observed than that demonstrated by the Lunar Crater samples at either of the orientations investigated (Figures 11 a and b). The ALHA 77005 data points appear to scatter to the lower right while the Lunar Crater data points scattered above the calibration curve at both orientations. Whether the difference in the direction of scatter is due to the presence of jarosite or to the different Fe-oxyhydroxide crystal structure (and crystallographic orientation relative to the olivine structure) is unknown.

Microprobe data. EMP analyses of locations correlating with the traverse 1 spectra shown in Figure 17 are provided in Table 4. EMP analyses of the olivine (analyses having oxide totals > 97% and 36-38 wt % SiO_2) were reduced using 4 oxygen atoms per formula unit, the iddingsite alteration (analyses having totals < 97 wt % but usually containing some SO_3) with 3 oxygen atoms per formula unit, and the jarosite alteration (analyses having > 12.5 wt % SO_3) with 11 oxygen atoms per formula unit. All Fe^{2+}/Fe^{3+} ratios were varied to satisfy stoichiometry; i.e., to bring the sum of the octahedral cations to 2.0 for olivine, the total cation sum of the iddingsite as close to 2.0 as possible, and the sum of the B cations to 3.0 for jarosite.

The brown host olivine in ALHA 77005 have compositions similar to the Mauna Kea olivine but are less-strongly zoned, Fo_{68-74}. Unlike the Lunar Crater and Mauna Kea samples, plots of the EMP data through the patchy alteration in ALHA 77005 indicate the presence of both silica-rich and silica-poor alteration products (see Fig. 20). The chemical trends indicate that the silica-rich alteration phase has SiO_2 contents of ~70 wt % (greater than that of smectites, which have 36-38 wt % SiO_2), suggesting the presence of amorphous silica. A broad microprobe spot size was used for the ALHA 77005 alteration (multiple phases analyzed simultaneously) so the silica content of the siliceous phase is probably higher than this. The trend of the FeO data from the unaltered olivine into the silica-poor secondary materials extrapolates to an FeO content appropriate for jarosite (~40 wt % FeO at 0 wt % SiO_2; see Fig. 20) and do not indicate the presence of akaganéite. The trend of the MgO data points indicates a low silica phase (~20 wt% SiO_2) which could be the jarosite or a polymerized phase.

The chemical trends of this patchy alteration differ from that of the Lunar Crater and Mauna Kea samples, which demonstrate the removal of Si from the olivine. The ALHA 77005 microprobe data indicate the mobility and removal of both Mg and Fe from the olivine and its alteration products, but suggest that Si mobility was limited in this sample. The Si became incorporated into an amorphous silica alteration phase, which suggests that the altering fluids were saturated in silica (Dymek, pers. communication).

A balanced reaction representing the ALHA 77005 alteration products using an olivine composition based on my EMP analyses, a theoretical end-member composition to represent the jarosite (assuming all Fe as Fe^{3+}), and assuming a single-stage reaction can be written as follows:

$$16\ Fe_{0.5}Mg_{1.5}SiO_4 + 18\ H_2O + K_2O$$

$$\rightarrow 2\ FeO(OH) + 16\ SiO_2 + 24\ MgO + 2\ KFe_3(SO_4)_2(OH)_6 + 11\ H_2$$

This reaction implies that more water is used up by the ALHA 77005 alteration reaction and more H_2 (as 2 H^+) is evolved than in either of the terrestrial samples producing an acidic environment.

Comparison of jarosite in olivine and chromite (*Raman spectra and EMP data).* Like the jarosite associated with the altered olivine, the chromite-hosted alteration products in ALHA 77005 are highly variable in composition. Representative analyses of several ALHA 77005 chromite and their associated alteration products are shown in Table 5a for comparison with the analyses of the olivine-hosted alteration shown in Table 4. Table 5b shows EMP analyses of the feldspathic glass ($Or_{1.5\text{-}2.7}An_{41\text{-}47}Ab_{50\text{-}58}$) that surrounds and appears to have reacted with the altered chromite mentioned above (see Fig. 8). The analyses in Table 5a demonstrate the range of compositions observed in the chromite alteration products. Chromite analyses were reduced by assuming 4 oxygen atoms per formula unit and varying the Fe^{2+}/Fe^{3+} ratios until the total number of cations equaled 3.0. As with the olivine-hosted alteration the chromite-hosted jarosite was reduced using 11 oxygen atoms per formula unit and the Fe^{2+}/Fe^{3+} ratios varied until the number of B cations equaled 3.0. I used the same formula for calculating the cation sums of the jarosite residing in the chromite as for that in the olivine.

The chromite-hosted alteration products are relatively enriched in Cr_2O_3 (ranging from 3.5 – 17 wt %), P_2O_5 (1.2 – 5.2 wt %), Al_2O_3 (up to 3.6 wt %), and FeO_{tot} (19 – 36 wt % FeO) versus that of the olivine (Cr_2O_3 < 3 wt %, P_2O_5 < 1.5 wt %, Al_2O_3 < 1.5 wt %, FeO_{tot} < 9 – 28 wt %). CaO and Na_2O contents are generally low (< 1 wt %) in both. Silica contents range up to 31 wt % in the chromite-hosted jarosite and up to 72 wt % in the olivine alteration products (again, implying silica saturated fluids). SiO_2, Cr_2O_3 and P_2O_5 all presumably substitute for SO_4 (the tetrahedral cation sums include these oxides) but it is possible that another secondary silicate with a small Raman cross-section (and therefore difficult to detect, e.g., a phyllosilicate) is intergrown with the jarosite. The sulfate content of the alteration in both phases is highly variable, ranging from 11 – 20 wt % SO_3 in the chromite alteration and from 1.5 – 20 wt % SO_3 in the olivine alteration, and is lower than the theoretical SO_3 content of jarosite (32 wt %). Note, however, that I used a 5 µm spot for most EMP analyses, that the samples are probably hydrated (totals are low), and that there is no external constraint on the Fe^{2+}/Fe^{3+} ratio of the jarosite; therefore the accuracy of Fe^{2+}/Fe^{3+} ratios that were calculated to satisfy cation site occupancy may not be unique.

The lack of a primary K-bearing mineral within the meteorite, coupled with the presence of K in the alteration, suggests that the infiltrating aqueous solution was potassic possibly due to leaching and transport from an overlying source. Meanwhile, the disparate compositions of the olivine and chromite-hosted sulfates suggest that Cr and P mobility was localized. The K_2O content of either lithology, and that of the bulk meteorite, is ~0.03 wt% and maskelynite compositions are reported to range from An_{24-56} (see Table VIII-1a in Meyer Compendium, 2003 for bulk compositions; Treiman et al., 1994 for maskelynite compositions). It is doubtful that enough K_2O could be leached from the maskelynite or the labradorite glass reported in Table 5b to produce the jarosite in these two thin sections. Some of the SiO_2 in the olivine-hosted iddingsite may have been mobilized from the host olivine but the high SiO_2 content of the chromite alteration products suggests that the altering fluids were saturated with dissolved silica.

Raman spectra of the olivine and chromite-hosted jarosite are quite similar despite the chemical variability indicated by Tables 4 and 5 (see Figure 20). Some Raman spectra of the chromite-hosted jarosite have an additional peak near 471 cm^{-1}, which probably belongs to elemental sulfur (the other major Raman peak of elemental sulfur, at 219 cm^{-1}, is buried under a major jarosite peak at this same location). A soil associated with the impact melt glass in fractures of thin section ALHA 77005,202 was found to contain goethite and elemental sulfur and could be the source of the Fe and S for the jarosite.

Summary of inferences regarding the mode of iddingsite alteration.

Alteration environment. Altered olivine occur throughout the Lunar Crater flow so I infer the iddingsite to have formed by reaction with deuteric waters shortly before or just after emplacement (flows are Pliocene to Holocene in age) at elevated temperatures. The temperature of formation of the Lunar Crater iddingsite is unknown, although instances of renewed olivine growth around iddingsitized cores suggest formation during consolidation of the magma (Edwards, 1938, Sheppard, 1962, see Fig. 3). Other forms of goethite (limonite, yellow ocher, gossan deposits) have relatively low T and P paragenesis (Yapp and Pedley, 1985). Likewise, the identification of akaganéite, previously reported to occur in the weathering products of Antarctic meteorites and purported to be a weathering product formed in lunar samples during their transport the Earth (Bland et al., 1997; Korotev, personal communication), in the iddingsite of the ALHA 77005 lherzolite (a deep-seated lithology) is confounding. The Washington University akaganéite reference spectrum came from a lunar sample that was irradiated in the nuclear reactor operated by the University of Missouri; but it is unclear whether this phase formed in a reaction the with water sealed in the silica tube with the sample at ambient temperatures or at the elevated temperature of the water bath during irradiation (Korotev and Zeigler, personal communication). So, the temperature of formation of the Lunar Crater and ALHA 77005 alteration products are not well constrained, presently. Calcite is present in Lunar Crater amygdules, but its deposition is not spatially correlated with the iddingsite, suggesting that the calcite was precipitated during a later event by post-magmatic meteoric waters (Rakovan, 2005).

In contrast, altered olivine grains are only present in the oxidative alteration rinds of the two Hawaiian samples and are clear examples of surface alteration. Secondary minerals, such as fine-grained calcite and amorphous silica and clay, occur in the vesicles of 16G1-30 (see Fig. 5). The younger sample is more altered than the older, for unknown reasons. The summit of Mauna Kea at present is cold and dry with temperatures between -4 °C (average winter low) and 10 °C (average summer high) and 15 cm of precipitation (mostly snow; CFHT website). The two flows sampled were separated temporally by the Makanaka glacial episode 13 thousand years ago (Wolfe et al., 1997) so some of the 16G1-30 alteration may have occurred at temperatures colder than currently present on Mauna Kea (the colder temperatures may have also reduced the rate of chemical weathering).

The brown and patchy alteration in ALHA 77005 resembles that of the Lunar Crater and Mauna Kea samples, but this sample is a lherzolite, not a basalt, so I infer the iddingsite to have formed at depth. The shergottites are generally inferred to be hypabyssal – that is, that they formed below the surface but above the magma chamber, so perhaps not at any great depth. Although I infer the ALHA 77005 iddingsite to have formed prior to the jarosite alteration on the basis of cross-cutting relationships, this cannot be demonstrated conclusively with just two thin sections. Only a search of multiple iddingsite-bearing thin sections for instances without a jarosite overprint could substantiate whether they were deposited at different intervals of time. Arslan and Arslan (2003) report the stability field of coexisting K-jarosite and goethite without hematite to be between pH = 1 and 3 and Eh = 0.9 and 1.15 at 25 °C and between pH = 0.5 and 4 and Eh = 0.9 and 1.15 at 95 °C; and note that both the goethite and jarosite fields shift to more acidic and oxidizing conditions as temperatures increase.

While the Lunar Crater sample fits the narrow definition of deuteric alteration (i.e., alteration by magmatic waters that separated from the magma as the result of depressurization en route to the surface; Edwards, 1938; Gay and LeMaitre, 1961; Sheppard, 1962), the iddingsite in ALHA 77005 fits the definition given by McSween (personal communication) – reaction of the olivine with the acidic volatiles (H_2O, HCl, H_2SO_4) that became concentrated around the crystal during the final stages of crystallization. This interpretation fits with the observation that the patchy alteration products occur in olivine that are poikilitically-enclosed by orthopyroxene. If, however, the brown alteration is considered to be an impact-related product (per the inference of Reynard et al., 2006, that the black olivine in chassignite NWA 2737 are due to minute particles of an Fe-Ni alloy, < 20 nm in diameter, implanted by an impact, I infer the brown color in the ALHA 77005 olivine to be due to small particles of magnetite, the oxidized equivalent of the iron particles, as indicated by a small peak near 670 cm^{-1}), then perhaps the alteration setting was not at any great depth. We interpret the jarosite alteration to have formed later, but whether this alteration also occurred at depth is unclear. Jarosite suggests alteration in an acidic environment, and the jarosite veins clearly crosscut all primary phases and line some fractures indicating that it may have formed in a near surface environment.

<u>Length scale of the reactions.</u> The distance over which the alteration reactions appear to occur is on the order of 8-10 µm in the Lunar Crater and ALHA 77005 iddingsite but ranges up to a few tens of µm in the Hawaiian basalt 16J-30. Because the olivine is relatively transparent compared to the alteration phases the distance over which the reactions appear to occur may be influenced by the detection of the alteration phases at depth within the olivine (see Appendix II).

<u>Chemical mobility, water/rock ratios.</u> Both the Lunar Crater and Mauna Kea (16J-30) samples show a net loss of Mg and Si with little addition of anything else. The ALHA 77005

alteration products indicate the mobility of Mg and Fe but retention of Si, which suggests that the ALHA altering fluids were saturated in silica whereas the Lunar Crater and Mauna Kea fluids were not. The alteration products of all three samples include iron oxides and oxyhydroxides with a poorly crystallized polymerized silicate (amorphous silica in the martian meteorite). The ALHA 77005 alteration products also contain jarosite which indicates a net influx of S and K. The coincidence of the iron oxides and hydroxides with the degradation of the olivine doublet reflects the concurrent oxidation of the Fe^{2+} with alteration. Chemical compositions vary systematically and the wt % FeO trends in Figures 12, 16, and 20 indicate the formation of goethite in the case of Lunar Crater, suggest the presence of either hematite or maghemite in Mauna Kea, and the presence of jarosite in ALHA 77005.

The ternary diagrams shown in Figure 21 suggest that the alteration in Mauna Kea involved only the addition of oxygen coincident with Fe oxidation ($Fe_2O_3 = 2\ FeO + ½\ O_2$) but the alteration in the Lunar Crater sample reflects the addition of OH as well as the oxidation of Fe. The chemical reactions provided in the discussion suggest that more water was required to drive alteration in the Lunar Crater sample than in the Mauna Kea sample. This is consistent with the petrographic observation that all of the olivine in the Lunar Crater flows exhibit some degree of alteration (although a comparison of bulk rock compositions would better demonstrate this). The chemical reaction provided for ALHA 77005 suggests that even more water is needed to produce the jarosite, but the patchy alteration products and jarosite only occur in a few thin sections.

Conclusions

All three iddingsite samples yielded different Raman spectra of their alteration products, they each contain a polymerized silicate phase(s) but only ALHA 77005 has enough silica in its patchy alteration to suggest amorphous silica. Different Fe-oxides and oxyhydroxides are present in each sample.

The Lunar Crater iddingsite has definitive goethite Raman peaks and a poorly crystallized ‘polymerized’ silicate. The Mauna Kea iddingsite also contains a polymerized silicate but has higher peak positions than that of the Lunar Crater sample and contains no goethite – only broad, weak features occur in its place. Probe data of the Mauna Kea iddingsite suggest that the Fe oxide present is hematite or maghemite; the lack of clear hematite Raman peaks implies that the Fe oxide is maghemite.

The ALHA 77005 iddingsite contains akaganéite (β-FeO(OH); a polymorph of goethite, α-FeO(OH)). ALHA 77005 also has a polymerized silicate phase but this is difficult to resolve in most traverses because of the later jarosite overprint. Where present, the polymerized phase is most apparent near the alteration front where the jarosite peaks are weaker. Jarosite is present in both the altered olivine and altered chromite of ALHA 77005 but the spectra do not reflect the variation in chemistry observed in the microprobe data.

Future work.

Determine the temperature of formation of the Lunar Crater and ALHA 77005 alteration products. Because hematite and goethite are the most common Fe^{3+} oxides on the surface of the Earth, Yapp (1987) and Yapp and Pedley (1985) looked into the use of the O and H isotope signatures of these minerals as indicators of paleotemperature. Their data suggest that the D/H ratios of goethite synthesized in the lab are independent of T between 25 and 145 °C but that the $^{18}O/^{16}O$ fractionation factor does vary between samples synthesized at 24, 44, and 62 °C. The petrographic evidence for elevated T during iddingsite formation conflicts with the low T and P paragenesis of other forms of goethite (limonite, ocher, gossan deposits). The isotopic signatures of the goethite in the Lunar Crater iddingsite might give us some indication of its temperature of formation; depending on how far the fractionation factors can be extrapolated. Analysis of the amygdular carbonate might be able to confirm whether these were deposited at the same time or later than the iddingsite. Further experimentation regarding the formation of akaganéite in lunar samples at room temperature or at the temperatures experienced in the nuclear reactor would also be informative.

Regarding the geologic setting and temperature of Lunar Crater olivine alteration. Smith (2000) suggested that Lunar Crater olivine are samples of the lower crust or upper mantle, that they derive from a plume that ascended relatively quickly (>50 cm/sec), and infer equilibrium temperatures in excess of 1270 ˚C. Ultramafic nodules in the Lunar Crater flows are also reported to contain CO_2 – rich fluid inclusions entrapped at moderate to high pressures (“volatile saturation via primary and/or retrograde boiling of basaltic magmas in the lower crust and upper mantle,” Bergman, 1984). Per my petrographic examination of the Lunar Crater olivine, I have invoked iddingsite formation per deuteric alteration en route to the surface.

However, the LCVF coincides with a region of anomalously low heat flow (the “Eureka Low”), which Sass et al. (1971) attribute to the influence of circulating ground water. Publications by John et al. (1989, 1991) report the incidence of coarse jarosite crystals in the matrices of breccias at the Paradise Peak Mine, Nye Co., NV, that presumably formed in response to alteration by oxidizing and acidic fluids at relatively low temperatures (150 – 200 ˚C) and depths less than 200 m. Jarosite formation temperatures of ~150˚C are supported by ^{18}O fractionation between the sulfate and hydroxyl sites in jarosite (Stoffregen and Rye, 1992 in Stoffregen, 1993). Isotopic studies (oxygen and hydrogen) of the hydroxyl in the goethite should be useful in determining both the source of the altering fluids (magmatic or meteoric) and the temperature of formation.

The Paradise Peak Mine and LCVF flows both occur in Nye Co., NV but the county is large and their geologic affinity unknown. The inference of alteration by ‘oxidizing and acidic fluids’ indicates that there could be a link between the emplacement of the LCVF flows and the formation of the jarosite deposit.

<u>Resolving Antarctic from martian alteration products.</u> Two potential projects that would be informative regarding the discrimination of Antarctic and martian alteration products are:

(1) A comparison of the alteration products in the Ferrar dolerite of Antarctica and with those of the MIL 03346 meteorite (Fleming et al. (1995) provide a brief, 1 paragraph, description of the alteration products in this clinopyroxenite that sound suspiciously similar to those present in MIL 03346, but this could be deceptive).

(2) A Raman survey of the alteration phases in NWA 817. Jarosite is present in both ALHA 77005 (shergottite) and MIL 03346 (nakhlite) and both of these meteorites are Antarctic. The jarosite in ALHA 77005 was initially suggested to be pre-terrestrial (Smith & Steele, 1983) but

later inferred to be an Antarctic weathering product (Gooding, 1981). No jarosite was found in Lafayette, and has not been reported in any of the non-Antarctic nakhlites but the mesostasis of NWA 817 (as pictured in Treiman, 2005) looks altered like that in MIL 00346. The discovery of jarosite in a non-Antarctic martian meteorite would support a martian origin.

<u>Analysis of alteration phases in the nakhlite (martian) meteorites.</u> Some of this data is already in hand, but is faulty. Notably, there are Fe^{2+}/Fe^{3+} issues with the probe data: (1) an inability to accurately calculate the cation sums and Fe^{2+}/Fe^{3+} ratios of the hydrous, vein-filling materials in Lafayette because the oxide sums are low; (2) conflicting inferences regarding the Fe^{2+}/Fe^{3+} ratios of the coarse and fine-grained alteration phases relative to Raman spectral identifications in Lafayette; and (3) MIL 03346 jarosite composition differs significantly from that of ALHA 77005 suggesting the presence of an unanalyzed component (possibly hydronium), which requires confirmation. In addition, (4) the traces of a former carbon coat impair our Raman spectral analysis of Lafayette and (5) issues remain regarding the crystallinity of our stilpnomelane standard (our standard is from Friedericke bei Weilburg, Nassau, Germany – a sample that once belonged to the Michigan School of Mines and is from a locality mentioned by Dana (1868); EMP analyses of the martian stilpnomelane and terrestrial standard are both consistent with analyses reported in the extended volumes of Deer et al., 1966, and XRD of the standard is consistent with a stilpnomelane reported by Guggenheim and Eggleton, 1987 but the Raman peaks of both are more consistent with it being a glass). I foresee several research projects (and papers) stemming from the resolution of these issues.

I recommend recollecting the nakhlite EMP data with oxygen included in the microprobe routine to see if the Fe^{2+} and Fe^{3+} proportions can be determined directly instead of by stoichiometric analysis. This analysis could help (1) resolve the conflict between the Raman and probe data regarding the Fe^{3+} contents of the coarse and fine-grained vein-filling materials in Lafayette, (2) may better constrain the extent/presence of the laihunite in MIL 03346 (at present, the totals are too high to adequately calculate the Fe^{2+}/Fe^{3+} ratios), and (3) help confirm the presence or absence of hydronium in the MIL 03346 jarosite. Including oxygen in my probe analysis of these materials could present a real undertaking because of a lack of established protocols for oxygen analysis. Establishing such protocols might best be done by obtaining a standard sample of laihunite and using the MIL 03346 as a test sample.

I am also interested in adding Northwest Africa (NWA) 817 to my study of the secondary materials in the nakhlites. NWA 817 is believed to have formed at depths intermediate to those of MIL 03346 and Lafayette. The vein-filling materials of this meteorite, as pictured in Treiman (2005), are visibly different from those in both MIL 03346 and Lafayette. The NWA 817 veins have saw-tooth outlines like those in Lafayette (whereas the veins in MIL 03346 are straight-edged) but the mineral filling the NWA 817 veins appears to be a single homogeneous phase while that in Lafayette is a micaceous intergrowth. I anticipate the NWA 817 vein-filing material are either a more crystalline mineral version of the stilpnomelane found in MIL 03346 or a metastable phase related to the micaceous materials in Lafayette. The three meteorites together would form something of a vertical profile through the parent cumulate body on Mars. The analysis of the alteration products in these three meteorites could then be used to make some inferences regarding the thermal profile of the body. The Lafayette materials have compositions similar to nontronite, and I have found a paper that refers to a sample of “primary nontronite,” that could be used as a potential terrestrial analog for the NWA 817 vein-filling materials, but the availability of the sample is questionable (reference is old, sample locality in Venezuela). This project will require a significant discussion of the terrestrial analogs (establishing their identity, inferred geologic setting) before any inferences can be made regarding the martian cumulate body.

References.

Armstrong J.T. (1988) Quantitative analysis of silicate and oxide materials: Comparison of Monte Carlo, ZAF, and φ(ρZ) procedures. *Microbeam Anal.*, **23**, 239-45.

Arslan, C. and Arslan, F. (2003) Thermochemical Review of Jarosite and Goethite stability regions at 25 and 95 °C. *Turkish J. of Eng. Env. Sci.*, **27**, 45-52.

Baker I. and Haggerty S.E. (1967) The alteration of olivine in basaltic and associated lavas; Part II: Intermediate and Low temperature alteration. *Contr. Mineral. Pet.*, **16**, 258-273.

Bandfield, J.L., Hamilton, V.E., and Christensen, P.R. (2000) A Global View of Martian Surface Compositions from MGS-TES. *Science*, **287**, 1626-1630.

Bergman S.C. (1984) Petrogenetic aspects of the alkali basaltic lavas and the included megacrysts and nodules from the Lunar Crater Volcanic Field, Nevada, USA. Princeton University, PhD Dissertation, p. 431.

Bibring J.P., Langevin Y., Gendrin A., Gondet B., Poulet F., Berthe M., Soufflot A., Arvidson R., Mangold N., Mustard J., Drossart P. and the OMEGA Team (2005) Mars surface diversity as revealed by the OMEGA/Mars Express Observations. *Science*, **307**, 1576-1581.

Bibring J.P., Langevin Y., Poulet F., Gondet B., Mangold N., Mustard J., Arvidson R., Chevrier V., Sotin C., and the OMEGA team (2007) Mars Climatic and Geological History, derived from the OMEGA/MEX Data. *7th International Conference on Mars*, abstr. #3234.

Biswas S., Ngo H.T., and Lipschutz M.E. (1980) Trace element contents of selected Antarctic meteorites. I. Weathering effects and ALH A77005, A77257, A77278, and A77299. *Z. Naturforsch. Teil. A*, 2, **35a**, 191-196.

Bland P.A., Kelley S.P., Berry F.J., Cadogan J.M., and Pillinger C.T. (1997) Artificial weathering of the ordinary chondrite Allegan: Implications for the presence of Cl^- as a structural component in akaganéite. *Am. Mineral.*, **82**, 1187-1197.

Brey, G.P. and Kohler, T. (1990) Geothermobarometry in four-phase lherzolites: II. New thermobarometers and practical assessment of existing thermobarometers. *J. of Petrology*, **31**, 1353-1378.

Bridges J.C., Catling D.C., Saxton J.M., Swindle T.D., Lyon I.C., and Grady M.M. (2001) Alteration assemblages in Martian meteorites: Implications for near-surface processes. *Space Science Rev.*, **96**, 365-392.

Brown G. and Stephen I. (1959) A structural study of iddingsite from New South Wales, Australia. *Am. Mineral.*, **44**, 251-260.

Burns R.G. (1993) Rates and Mechanisms of chemical weathering of ferromagnesian minerals on Mars. *Geochim. Cosmochim. Acta*, **57**, 4555-4574.

Canada France Hawaii Telescope online instruction manual, version 1.0 (2003) (available at: <http://www.cfht.hawaii.edu/Instruments/ObservatoryManual/index.html>), accessed 9/29/09.

Chopelas A. (1991) Single crystal Raman spectra of forsterite, fayalite, and monticellite, *Am. Mineral.*, **76**, 1101-1109.

Christensen P.R., Ruff S.W., Fergason R.L., Knudson A.T., Anwar S., Arvidson R.E., Bandfield J.L., Blaney D.L., Budney C., Calvin W.M., Glotch T.D., Golombek M.P., Gorelick N., Graff T.G., Hamilton V.E., Hayes A., Johnson J.R., McSween H.Y. Jr., Mehall G.L., Mehall L.K., Moersch J.E., Morris R.V., Rogers A.D., Smith M.D., Squyers S.W., Wolff M.J., and Wyatt M.B. (2004a) Initial Results from the Mini-TES Experiment in Gusev Crater from the Spirit Rover. *Science*, **305**, 837- 842.

Christensen P.R., Wyatt M.B., Glotch T.D., Rogers A.D., Anwar S., Arvidson R.E., Bandfield J.L., Blaney D.L., Budney C., Calvin W.M., Fallacaro A., Fergason R.L., Gorelick N., Graff T.G., Hamilton V.E., Hayes A., Johnson J.R., Knudson A.T., McSween H.Y. Jr., Mehall G.L., Mehall L.K., Moersch J.E., Morris R.V., Smith M.D., Squyers S.W., Ruff S.W., and Wolff M.J. (2004b) Mineralogy at Meridiani Planum from the Mini-TES Experiment on the Opportunity Rover. *Science*, **306**, 1733-1739.

Deer W.A., Howie R.A., and Zussman J. (1966) *The Rock Forming Minerals*. London: Longmans, 528 p.

De Faria D.L.A., Venancio Silva S., and de Oliveira M.T. (1997) Raman microspectroscopy of some iron oxides and oxyhydroxides. *J. Raman Spectr.*, **28**, 873-878.

Delvigne J., Bisdom E.B.A., Sleeman J., and Stoops G. (1979) Olivines, their pseudomorphs and secondary products. *Pedologie*, **29**, 3, 247-309.

Delvigne J.E. (1998) Atlas of Micromorphology of Mineral Alteration and Weathering. *Can. Mineral. Sp. Pub.* 3, Ontario, Canada, 494 p.

Dutrizac J.E. and Jambor J.L. (2000) Jarosites and their application in Hydrometallurgy. In *Sulfate minerals; Crystallography, Geochemistry, and Environmental Significance*. RIM, **40**, 405-452.

Eaton G.P. (1980) Geophysical and Geological characteristics of the Crust of the Basin and Range Province. In Studies in Geophysics, Continental Tectonics. National Research Council, National Academy of Sciences, Washington D.C., pp. 96-113.

Edwards A.B. (1938) The formation of iddingsite. *Am. Mineral.*, **23**, 277-281.

Eggleton R.A. (1984) Formation of Iddingsite rims on olivine: a transmission electron microscope study. *Clays and Clay Mineral.*, **32**, 1, 1-11.

Eggleton R.A., Foudoulis C., and Varkevisser D. (1987) Weathering of Basalt: Changes in Rock Chemistry and Mineralogy. *Clays and Clay Mins.*, **35**, 3, 161-169.

Fleming T.H., Foland K.A. and Elliot D.H. (1995) Isotopic and chemical constraints on the crustal evolution and source signature of Ferrar magmas, north Victoria Land, Antarctica. *Contrib. Mineral. Pet.*, **121**, 217-236.

Fries M., Rost D., Vicenzi E., and Steele A. (2006) Raman Imaging analysis of Jarosite in MIL 03346. *Martian Sulfates as recorders of Atmospheric-Fluid-Rock Interactions*, abstr. #7060.

Gay P. and LeMaitre R.W. (1961) Some observations on "Iddingsite." *Am. Mineral.*, **46**, 92-111.

Gooding J.L. (1981) Mineralogical aspects of terrestrial weathering effects in chondrites from Allan Hills, Antarctica. *Proc. Lunar Planet. Sci. 12th*, 1105-1122.

Gooding J.L. (1984) Search for "Martian weathering" effects in achondrites EETA 79001 and ALHA 77005: Complications from Antarctic Weathering. *15th LPSC*, 310-311.

Gooding J.L. (1992) Soil mineralogy and Chemistry on Mars: Possible clues from Salts and Clays in SNC meteorites. *Icarus*, **99**, 28-41.

Guggenheim S. and Eggleton R.A. (1987) Modulated 2:1 layer silicates: Review, systematics, and predictions. *Am. Mineral.*, **72**, 724-738.

Hurowitz J.A. and McLennan S.M. (2007) A 3.5 Ga record of water-limited, acidic weathering conditions on Mars. *Earth and Planet. Sci.*, **260**, 432-443.

Israel E.J. (1996) Examination of a desert varnished basalt using electron microprobe analyses and laser Raman spectroscopy. Washington University, M.A. Thesis, p.79.

Israel E.J., Arvidson R.E., Wang A., Pasteris J.D., and Jolliff B.L. (1997) Laser Raman spectroscopy of varnished basalt and implications for in-situ measurements of Martian rocks. *J. Geophys. Res.*, **102**, E12, 28705-28716.

John D.A., Thomason R.E., and McKee E.H. (1989) Geology and K-Ar Geochronology of the Paradise Peak Mine and the Relationship of Pre-Basin and Range Extension to Early Miocene Precious Metal Mineralization in West-Central Nevada. *Econ. Geol.*, **84**, 631-649.

John D.A., Nash J.T., Clark C.W., and Wulftange W.H. (1991) Geology, Hydrothermal Alteration, and Mineralization at the Paradise Peak Gold-Silver-Mercury Deposit, Nye County, Nevada. In *Geology and Ore Deposits of the Great Basin*, Raines, G.L., Lisle, R.E., Schafer, R.W., and Wilkinson, W.H. (Eds.), Symposium Proceedings, Geol. Soc. Nevada (Reno) 2:1020-1050.

Khisina N.R., Khramov D.A., Kolosov M.V., Kleschev A.A., and Taylor L.A. (1995) Formation of ferriolivine and magnesioferrite in Mg-Fe olivine: Reactions and Kinetics of Oxidation. *Phys. Chem. Mineral.*, **22**, 241-250.

Klingelhöfer G., Morris R.V., Bernhardt B., Schröder C., Rodionov D.S., de Souza P.A. Jr., Yen A., Gellert R., Evlanov E.N., Zubkov B., Foh J., Bonnes U., Kankelkeit E., Gütlich P., Ming D.W., Renz F., Wdowiak T., Squyers S.W., and Arvidson R.E. (2004) Jarosite and Hematite at Meridiani Planum from Opportunity's Mossbauer spectrometer. *Science*, **306**, 1740-1745.

Korotev, R.L. (2005) Lunar geochemistry as told by lunar meteorites. *Chemie der Erde*, **65**, 297-346.

Kristall B. (2000) Chemical alteration on the south flank of Mauna Kea, Hawaii. Washington University, Senior Honors thesis, 37 p.

Kuebler K.E., Jolliff B.L., Wang A., and Haskin L.A. (2006) Extracting olivine (Fo-Fa) compositions from Raman spectral peak positions. *Geochim. Cosmochim. Acta*, **70**, 6201-6222.

Kuebler K., Jolliff B.L., and Treiman A. (2007) A survey of alteration products and other secondary minerals in Martian meteorites recovered from Antarctica. *38th LPSC*, abstr. # 2228.

Marvin U.B. (1980) Catalog of Antarctic meteorites 1977-1978, edited by B. Mason. *Smithsonian Contrib. Earth Sci.*, **23**, 50 p.

McSween H.Y. Jr, Arvidson R.E., Bell J.F. III, Blaney D., Cabrol N.A., Christensen P.R, Clark B.C., Crisp J.A., Crumpler L.S., Des Marais D.J., Farmer J.D., Gellert R., Ghosh A., Gorevan S., Graff T., Grant J., Haskin L.A., Herkenhoff K.E., Johnson J.R., Jolliff B.L., Klingelhöfer G., Knudson A.T., McLennan S., Milam K.A., Moersch J.E., Morris R.V., Rieder R., Ruff S.W., deSouza P.A. Jr., Squyers S.W., Wänke H., Wang A., Wyatt M.B., Yen A., Zipfel J. (2004) Basaltic rocks analyzed by the Spirit Rover in Gusev Crater. *Science*, **305**, 842-845.

Meyer C. (2003) Mars Meteorite Compendium. JSC Report 27672. Johnson Space Center, Houston, TX. (Also available at: <http://www-curator.jsc.nasa.gov/antmet/mmc/index.cfm>).

Ming D.W., Golden D.C., Gooding J.L., Morris R.V., Thompson D.R., and Bell J.F. III (1996) Mineralogical and thermal properties of jarositic tephra on Mauna Kea, Hawaii: Implications for the sulfur mineralogy on Mars. *27th LPSC*, 883-884.

Mittlefehldt D.W., Wentworth S.J., Wang M.S., Lindstrom M.M., and Lipschutz M.E. (1997) Geochemistry of and alteration phases in Martian lherzolite Y-793605. *Ant. Met. Res.*, **10**, 109-124.

Morris R.V., Klingelhöfer G., Bernhardt B., Schröder C., Rodionov D.S., de Souza P.A. Jr., Yen A., Gellert R., Evlanov E.N., Foh J., Kankelkeit E., Gütlich P., Ming D.W., Renz F., Wdowiak T., Squyers S.W., and Arvidson R.E. (2004) Mineralogy at Gusev Crater from the Mössbauer spectrometer on the Spirit Rover. *Science*, **305**, 833-836.

Ostertag R., Amthauer G., Rager H., and McSween H.Y. Jr. (1984) Fe^{3+} in shocked olivine crystals of the ALHA 77005 meteorite. *Earth Planet. Sci. Lett.*, **67**, 162-166.

Papike J.J. (1987) Chemistry of the Rock-Forming Silicates: Ortho, Ring, and Single-Chain Structures. *Rev. Geophys.*, **25**, 7, 1483-1526.

Papike J.J, Karner J.M., Spilde M.N., and Shearer C.K. (2006a) Terrestrial analogs of Martian sulfates: Major and minor element systematics of alunite-jarosite from Goldfield, Nevada. *Am. Mineral.*, **91**, 1197-1200.

Papike J.J., Karner J.M., and Shearer C.K. (2006b) Comparative planetary mineralogy: Implications of Martian and terrestrial jarosite. A crystal chemical perspective. *Geochim. Cosmochim. Acta*, **70**, 1309-1321.

Pâques-Ledent M.T. and Tarte P. (1973) Vibrational studies of olivine-type compounds –I. The i.r. and Raman spectra of the isotopic species of Mg_2SiO_4. *Spectrochim. Acta,* **29A**, 1007-1016.

Pouchou J. and Pichior F. (1991) Quantitative analysis of homogeneous or stratified microvolumes applying the model "PAP." In *Electron Probe Quantitation* (Ed. K.F.J. Heinrich and D.E. Newbury), Plenum, pp.31-75.

Poulet F., Bibring J.P., Mustard J.F., Gendrin A., Mangold N., Langevin Y., Arvidson R.E., Gondet B., Gomez C., and the OMEGA Team (2005) Phyllosilicates on Mars and implications for early Martian climate. *Nature*, **438**, 623-627.

Piriou B. and McMillan P. (1983) The high-frequency vibrational spectra of vitreous and crystalline orthosilicates. *Am. Mineral.,* **68**, 426-443.

Rakovan, J. (2005) Amygdule. *Rocks and Minerals*, **80**, 202-203.

Reynard B., Van de Moortèle B., Beck P., and Gillet P. (2006) Shock induced transformations in olivine of the Chassignite NWA 2737. *37th LPSC*, abstr. #1837.

Ripmeester J.A., Ratcliffe C.I., Dutrizac J.E., and Jambor J.L. (1986) Hydronium ion in the Alunite – Jarosite Group. *Can. Mineral.*, **24**, 435 – 447.

Sass J.H. Lachenbruch A.H., Munroe R.J., Greene G.W., and Moses T.H. Jr. (1971) Heat flow in the Western United States, *J. Geophys. Res.*, **76**, 26, 6376 – 6413.

Scott K.M. (1987) Solid solution in, and classification of, gossan-derived members of the alunite-jarosite family, northwest Queensland, Australia. *Am. Mineral.*, **72**, 178-187.

Scott D.H. and Trask N.J. (1971) Geology of the Lunar Crater Volcanic Field, Nye County, Nevada. U.S. Geological Survey Prof. Paper, 599-I, 22 p.

Sheppard R.A. (1962) Iddingsitization and recurrent crystallization of olivine in basalts from the Simcoe Mountains, Washington. *Am. J. Science*, **260**, 67-74.

Smith J.V. and Steele I.M. (1983) Pre-terrestrial alteration of achondrite 77005: Effect of Martian volatiles? *14th LPSC*, 712-713.

Smith J.V. and Steele I.M. (1984) Achondrite ALHA77005: Alteration of Chromite and Olivine. *Meteoritics*, **19**, 3, 121-133.

Smith K.L., Milnes A.R., and Eggleton R.A. (1987) Weathering of Basalt: Formation of Iddingsite. *Clays and Clay Mineral.*, **35**, 6, 418-428.

Smith D. (2000) Insights into the evolution of the uppermost continental mantle from xenolith localities on and near the Colorado Plateau and regional comparisons. *J. Geophys. Res.*, **105**, B7, 16769-16781.

Spera, F.J. (1980) Aspects of Magma Transport. In *Proc. Conf. Phys. and Chem. of Magmatic Processes*, R.B. Hargraves (ed.), Princeton University Press, Princeton, NJ, 265-324.

Stöffregen R.E. and Rye, R.O. (1992) Jarosite-water ^{18}O and D fractionations. *Amer. Chem. Soc. Div. Geochem*., **204**, 86, abstr.

Stöffregen, R.E. (1993) Stability relations of jarosite and natrojarosite at 150-250 ˚C. *Geochim. Cosmochim. Acta*, **57**, 2417-2429.

Stöffregen R.E., Alpers C.N., Jambor J.L. (2000) Alunite-Jarosite Crystallography, Thermodynamics, and Geochronology. In *Sulfate minerals; Crystallography, Geochemistry, and Environmental Significance*. RIM, **40**, 453-479.

Stopar J.D., Taylor G.J., and Norman M.D. (2007) Aqueous alteration in Nakhlite MIL 03346: LA-ICPMS and Raman Spectroscopy. *7th International Conference on Mars*, abstract #3105.

Sun M.S. (1957) The nature of iddingsite in some basaltic rocks of New Mexico. *Am. Min.*, **42**, 525-533.

Tosca N.J., McLennan S.M., Lindsley D.H., and Schoonen M.A.A. (2004) Acid-sulfate weathering of synthetic Martian basalt: The acid fog model revisited. *J. Geophys. Res.*, **109**, E05003, doi:10.1029/2003JE002218.

Treiman A.H., Barrett R.L., and Gooding J.L. (1993) Preterrestrial aqueous alteration of the Lafayette (SNC) meteorite. *Meteoritics*, **28**, 86-97.

Treiman A.H., McKay G.A., Bogard D.D., Mittlefehldt D.W., Wang M.S., Keller L., Lipschutz L.E., Lindstrom M.M., Garrison D. (1994) Comparison of the LEW 88516 and ALHA 77005 martian meteorites: Similar but distinct. *Meteoritics*, **29**, 581-592.

Treiman A.H., Lanzirotti A., and Xirouchakis D. (2004) Synchrotron X-ray diffraction analysis of meteorites in thin section: Preliminary results. *35th LPSC*, abstr. #1172.

Treiman A.H. (2005) The Nakhlite meteorites: Augite-rich igneous rocks from Mars. *Chemie der Erde*, 65, 203-270.

Treiman A.H. (2006) Sulfate-bearing minerals in the Martian meteorites. *Workshop on Martian Sulfates as Recorders of Atmospheric-Fluid-Rock Interaction*, #7017.

Treiman A.H., Dyar M.D., McCanta M., Noble S.K., and Pieters C.M. (2007) Martian dunite NWA 2737: Petrographic constraints on geological history, shock events, and olivine color. *J. Geophys. Res.*, **112**, E04002, doi:10.1029/2006JE002777.

Wang A., Han J., Guo L., Yu J., and Zeng P. (1994) Database of standard Raman spectra of minerals and related inorganic crystals. *App. Spectr.*, **48**, 8, 959-968.

Wang A., Jolliff B.L., and Haskin L.A. (1999) Raman spectroscopic characterization of a highly weathered basalt: Igneous mineralogy, alteration products, and a microorganism. *J. Geophys. Res.*, **104**, E11, 27067–27077.

Wang A., Kuebler K.E., Jolliff B.L., and Haskin L.A. (2004) Raman spectroscopy of Fe-Ti-Cr oxides, case study: Martian meteorite EETA 79001. *Am. Mineral.*, **89**, 665-680.

Warren P.H. (1994) Lunar and Martian meteorite delivery services. *Icarus*, **111**, 338-363.

Wells S.G., Dohrenwend J.C., McFadden L.D., Turrin B.D., and Mahrer K.D. (1985) Late Cenozoic landscape evolution on lava flow surfaces of the Cima volcanic field, Mojave Desert, California. *GSA Bulletin*, **96**, 1518-1529.

Wentworth S.J. and Gooding J.L. (1993) Weathering features and secondary minerals in Antarctic Shergottites ALHA 77005 and LEW 88516. *24th LPSC*, 1507-1508.

Wentworth S.J., Gibson E.K., Velbel M.A., and McKay D.S. (2005) Antarctic Dry Valleys and indigenous weathering in Mars meteorites: Implications for water and life on Mars. *Icarus*, **174**, 383-395.

Wilshire H.G. (1958) Alteration of olivine and orthopyroxene in basic lavas and shallow intrusions. *Am. Mineral.*, **43**, 120-147.

Wolfe E.W., Wise W.S., and Dalrymple G.B. (1997) The Geology and Petrology of Mauna Kea Volcano, Hawaii – A Study of Postshield Volcanism. U.S. Geological Survey Prof. Paper 1557, Reston, VA U.S. Geological Survey, Serial Report Map, Reston, VA, U. S. Geological Survey, United States, pp. 129.

Wyatt, M.B. and McSween, H.Y., Jr. (2002) Spectral evidence for weathered basalt as an alternative to andesite in the northern lowlands of Mars. *Nature*, **417**, 263-266.

Yapp, C.J. and Pedley, M.D. (1985) Stable hydrogen isotopes in iron oxides-II. D/H variations among natural goethites. *Geochim. Cosmochim. Acta*,, **49**, 487 – 495.

Yapp, C.J. (1987) Oxygen and hydrogen isotope variations among goethites (α-FeOOH) and the determination of paleotemperatures. *Geochim. Cosmochim. Acta*,, **51**, 355 – 364.

Appendix I. Detailed analysis of the Lunar Crater traverses.

The ~820 cm^{-1} peak is weaker than the ~850 cm^{-1} peak in the olivine doublets of the spectra acquired ahead of the alteration front in the large phenocryst that traverses 1-3 were made on. When the peak positions of the olivine doublets from these three traverses are plotted on the olivine calibration curve of Kuebler et al. (2006), the points rise above the olivine calibration curve (see Fig. 11) as the signal-to-noise ratio of the spectra decreases. The green data points (representing doublets from spectra whose ~820 cm^{-1} peak has a height/width ratio >10) were taken inside the olivine ahead of, but in proximity to, the alteration front while the red dots represent spectra acquired in an unaltered portion of the phenocryst. Because the olivine doublets disappear quickly inside the alteration, the black data points (weaker doublets) represent spectra acquired just inside the alteration front. The apparent effect of alteration on the olivine doublet at this crystal orientation (the same for all three traverses) is a relative increase in the peak positions of both peaks with the peak positions of the ~820 cm^{-1} peak shifting more than the ~850 cm^{-1} peak. Figure 22 shows the curve-fit peak positions plotted against the peak height/width ratios, from which it is apparent that a loss in signal is correlated to an increase in peak position. Again, green dots represent data from olivine doublets whose 820 cm^{-1} height/width ratios are >10 and black data points represent data points from olivine spectra whose 820 cm^{-1} height/width ratios are <10. While it is likely that some of the apparent increase in peak position is due to an increase in error associated with the curve-fitting of weaker doublets, the peak positions of *both* peaks in these three traverses increase whereas correlated errors in peak position would be expected if the shifts were due solely to errors in curve-fitting (i.e., an increase in one set of peak positions producing a increase in the other). The degree and direction of the shift of peak positions is not consistent for all of the traverses, however, and the peak positions of the doublet in several traverses show nothing but scatter about the median calibration curve as the degree of alteration increases and peak resolution diminishes.

I repeated several of the traverses on Lunar Crater with the thin section rotated roughly 90 degrees relative to the laser beam (see Table 2). In all but two cases, this had the effect of making the opposite peak of the doublet the stronger of the two peaks and typically the pattern of scattering on the calibration plot differed from the original set of traverses. The pattern of scattering does not appear to be a function of which peak in the doublet is initially weaker at that orientation but no systematic study of crystal orientations was pursued. Comparing the calibration curve plots of the data points from traverses 1-3 on the Lunar Crater phenocryst (Figure 11a) with their 90-degree counterparts (Figure 11b), the ~820 cm^{-1} peak positions increase in both data sets but the ~850 cm^{-1} peak positions, as shown in Figure 11b, scatter to both higher and lower Raman shifts. I observed a clear upshift of both peaks only when the ~820 cm^{-1} peak is initially the weaker peak. In addition, I observed that the ~820 cm^{-1} peak degrades faster than the ~850 cm^{-1} peak in all traverses where the ~820 cm^{-1} peak is initially the stronger of the two (see Figure 23). This is not true of the 850 cm^{-1} peak. Based on these observations, I believe that at least some of the observed scatter in the 820 cm^{-1} peak positions is due to changes in the bonding environment, that crystal orientation is important to the degree and direction of the observed scatter, and that alteration has a stronger effect on the ~820 cm^{-1} peak than on the ~850 cm^{-1} peak. These observations are consistent with the interpretation of Chopelas (1991) that the ~820 cm^{-1} peak has a higher contribution from the v_3 (asymmetric mode) than the ~850 cm^{-1} peak because the v_3 mode is more easily affected by variations in the Si- O_{nb} force constant and should be affected more by the breakdown of SiO_4 units during polymerization. A more thorough study of the effects of alteration at different crystal orientations with a polarized laser is needed to fully resolve the effects of crystal orientation and alteration on the peak positions of the doublet if we wish to better constrain which crystal sites are most affected by alteration.

Appendix II. Detailed analysis of the Mauna Kea traverses.

Traverse 1 crossed a small olivine (~0.06 mm in diameter) in 16G-30 with relatively thin alteration rims, 5-10 µm thick, as seen in reflected light. Although the alteration rim looks symmetric in reflected light, more alteration is present at depth in the thin section on the side of the olivine at the end of the traverse (as seen in transmitted light, see Fig. 24). The minor degree of alteration is apparent in the spectra at the beginning of the traverse (Fig. 25a). The olivine peaks weaken but do not broaden much and the doublet can be resolved throughout the alteration. The ~640 and ~710 cm^{-1} peaks of the polymerized phase appear several µm ahead of the alteration front but are quite weak; they strengthen and resolve inside the alteration front but never dominate the spectra. The polymerized features near 945 and 1035 cm^{-1} can only be discerned at the alteration front or inside the alteration.

The alteration reaction appears to be more protracted in the spectra from the other end of the traverse (Fig. 25b) because of the alteration products at depth in the thin section. Again, the ~640 and ~710 cm^{-1} peaks are the first alteration peaks to appear and these appear well ahead of the alteration front (~30 µm, as seen in reflected light) and the changes in the spectra are more gradual. The ~640 and ~710 cm^{-1} peaks are initially shorter than the minor olivine peak at 600 cm^{-1} (1/6 the height of the doublet) but strengthen over the next several µm. Broad peaks near

1035 cm^{-1} and 1350 cm^{-1} appear over the same distance. The spectral pattern is similar for the next 20 µm. The peaks of the polymerized phase strengthen on approach to the alteration front with the strength of the ~640 cm^{-1} peak outpacing that of the ~710 cm^{-1} peak. About 5 µm ahead of the alteration front the peaks of the polymerized phase are roughly half the height of the olivine doublet. The olivine doublet quickly diminishes into a remnant feature and disappears at the alteration front (occurs at spectrum 08080369). As observed for Lunar Crater, the spectra acquired at or just inside the alteration front are noisier than those acquired just ahead of or behind it. The last few spectra, near the edge of the olivine grain are weak and the peaks of the polymerized phase better resolved with three distinct peaks in both of the multi-component features of the polymerized silicate. The multi-component feature in the 400-800 cm^{-1} (Si- O_b -Si) region has peaks at 640, 680, and 715 cm^{-1} the strongest of which is the 640 cm^{-1} peak. Two of these spectra also have a peak near 480 cm^{-1} that could belong to a clay (Hectorite, SHCa-1, has peaks near 465 and 688 cm^{-1}). The multi-component feature in the 800-1100 cm^{-1} (Si- O_{nb}) region is resolved into peaks occurring at 950, 1005, and 1065 cm^{-1} that are equivalent in height. The improved peak resolution in the alteration products implies that the alteration materials are better developed at this edge of the olivine. Furthermore, the number of peaks (three in the well resolved spectra, but possibly a fourth ~580 cm^{-1}) in the 400-800 cm^{-1} region implies that the polymerized phase is a mixture of phases. The peaks in the 800-1100 cm^{-1} region seem strong for phyllosilicates but the peak height may be exaggerated as a result of the baseline subtraction. The 715 cm^{-1} peak position of the last few spectra could belong to a dioctahedral phyllosilicate (Wang et al., 2002). Some spectra have a single broad, weak band in the O-H stretching mode region near 3450 cm^{-1}, consistent with either a clay or amorphous silica, while other spectra contain two broad, weak bands near 3380 and 3755 cm^{-1} of unknown affinity.

Traverse 5 crossed a larger, resorpted olivine in 16J-30 whose rim of alteration is discontinuous but ranges up to tens of µm in thickness. The alteration is well developed at one side of the grain (the upper edge as shown in Fig. 6) where it is opaque in transmitted light. I focus the discussion on the spectra acquired across this alteration front, which is sharp in both transmitted and reflected light, although the traverse crossed the entire grain (Fig. 13). The ~640 and ~710 cm^{-1} peaks of the polymerized phase appear 2 µm ahead of the alteration front (occurs at 09080459) and are initially weak (1/7 the height of the doublet, equivalent in height to the minor olivine peak at 540 cm^{-1}). Spectra at the alteration front are less noisy in this traverse than in the other grains I examined. The ~640 and ~710 cm^{-1} peaks strengthen inside the alteration and are about 1/4 - 1/3 of the height of the olivine doublet within 8 µm of the inside of the alteration front but the olivine doublet persists and dominates the spectra well into the alteration, ~ 30 µm (until spectrum 0475, 2 µm steps). The olivine doublet only degrades in proximity to reflective alteration products, ~ 32 µm behind the alteration front, and reappears beyond the reflective materials in the last two spectra of the traverse. The ~945 and ~1035 cm^{-1} peaks that occur in the 800-1100 cm^{-1} (Si- O_{nb}) region are weak throughout the alteration but are strongest near the rim of the olivine. OH and the 1300 cm^{-1} peaks (hematite or maghemite) are both uncommon in this traverse.

Traverse 6 crossed a large, heavily altered olivine in 16J-30 (Fig. 26). This olivine grain has no transparent areas when viewed in transmitted light but olivine is present at the upper surface of the thin section in the middle of the grain (100-120 µm from the edge of the grain as seen in reflected light) and olivine dominates spectra collected there. There are no spectra without alteration peaks but the polymerized silicate peaks are quite weak in the spectra from the center of the olivine (Fig. 27), where the ~640 and ~710 cm^{-1} peaks have intensities equivalent to minor olivine peaks (heights are ~1/10 that of the doublet). The intensities of the ~640 and ~710 cm^{-1} peaks increase as they approach the alteration front; they are about 1/2 the height of the olivine doublet 6 µm ahead of the alteration front and become the dominant phase behind it. In this traverse the ~710 cm^{-1} peak is taller than the ~640 cm^{-1} peak. The ~390 and ~1300 cm^{-1} peaks appear 2 µm ahead of the alteration front and occur in all but a few spectra of the alteration. The intensity of the olivine doublet begins to diminish ~8 µm ahead of the alteration front and degrades into a very weak remnant near 830 cm^{-1} within the 6 µm behind the alteration front (spectrum 09100351). The olivine remnant, however, persists throughout the alteration, appearing in all but two spectra. Polymerized silicate peaks in the 800-1100 cm^{-1} (Si- O_{nb}) region are very weak, their peak positions are variable and not well resolved in many spectra. As in traverse 5, no OH peaks were observed.

Table 1a. Samples used in study, Raman data collection parameters, instruments used for Raman data collection

Sample description, thin sections used	thin section, olivine label	Raman traverse*	Raman objective	date Raman data collected	Raman laser power (in mW)	under N_2 purge	Raman acc. time	# of spectra in Raman traverse	step size in µm
1) Lunar Crater	ol phenocryst	1	20x	1/22/2003	2.0	no	5s x 10	94	2
terrestrial alkali basalt	ol phenocryst	2	20x	1/22/2003	2.0	no	5s x 10	94	2
QBV1 & QBV2**	ol phenocryst	3	20x	1/27/2003	2.1	no	5s x 10	72	2
	ol phenocryst	4	100x	6/25 & 26/2008	0.8	yes	10s x 5	201	1
	1st groundmass ol	5	20x	6/26/2003	2.1	yes	10s x 5	73	1
	2nd groundmass ol	6	20x	6/30/2008	2.2	yes	10s x 5	76	1
	3rd groundmass ol	7	20x	6/30/2003	2.2	yes	10s x 5	66	1
	ol phenocryst	8	20x	7/10/2003	2.1	yes	10s x 5	200	1
	ol phenocryst	9	20x	3/7/2004	4.7	yes	10s x 5	70	1
	ol phenocryst	10	20x	3/13/2004	4.8	yes	10s x 5	113	2
	ol phenocryst	11	20x	4/15/2004	4.9	yes	10s x 5	77	1
	ol phenocryst	12	20x	4/16/2004	5.0	yes	10s x 5	87	1
	ol phenocryst	13	20x	4/19/2004	5.0	yes	10s x 5	62	1
	ol phenocryst	14	20x	4/24/2004	5.5	yes	10s x 5	74	1
	ol phenocryst	15	20x	4/25/2004	5.2	yes	10s x 5	78	1
	ol phenocryst	16	20x	4/29/2004	5.2	yes	10s x 5	78	1
	ol phenocryst	17	20x	6/13 & 14/2004	11.6	yes	10s x 5	287	1
2) Mauna Kea	16G1-30	1	20x	8/8/2003	2.0	yes	10s x 5	74	1
post-shield flows	16G1-30	2	20x	8/9/2003	2.0	part of traverse	10s x 5	81	1
hawaiite & mugearite	16G1-30	3	20X	8/11/2003	2.0	no	10s x 5	136	1
16J-30, 16G1-30	16G1-30	4	20x	8/12/2003	2.0	no	10s x 5	49	1
	16J-30	5	20x	9/8 & 9/2003	2.0	yes	10s x 5	182	2
	16J-30	6	20x	9/10/2003	2.0	no?	10s x 5	59	2
	16J-30	7	20x	9/10/2003	2.0	no?	10s x 5	15	10
3) ALHA 77005	,51 on olivine 10	1	20x	5/26/2008	4.8	no	10s x 10	140	1
lherzolitic shergottite	,51 on olivine 15	2	20x	6/4 & 5/2008	5.3	no	8s x 10	243	1.5
,51 & ,34	,51 on olivine 14	3	20x	6/6 & 7/2008	5.5	no	8s x 10	226	1
	,51 on olivine 11	4	20x	6/8 & 9/2008	5.5	no	8s x 10	244	1
	,51 on olivine 15	5	20x	6/10/2008	5.5	no	8s x 10	88	1

* repeated some Raman traverses with different parameters or at different orientations relative to laser polarization

** Lunar Crater thin sections made from the same parent samples used by Israel (1996)

Table 1b. Samples used in study, microprobe data collection parameters, instruments used for microprobe data collection

Sample description, thin sections used	Raman manual traverse	corresponding EMP traverse*	EMP instrument**	date EMP data collected	EMP acc. voltage	EMP beam current	EMP spot size (in µm)
1) Lunar Crater	1	unk 32	JEOL 733	8/26/2003	15 keV	30 nA	1
terrestrial alkali basalt	2	unk 7	JEOL 733	8/25/2003	15 keV	30 nA	1
QBV1 & QBV2	3	none	JEOL 733	none	-----------	-----------	-----------
	4	-----------	JEOL 733	8/25/2003	-----------	-----------	-----------
	5	unk 15	JEOL 733	8/25/2003	15 keV	30 nA	1
	6	unk 30	JEOL 733	8/26/2003	15 keV	30 nA	1
	7	unk 31	JEOL 733	8/26/2003	15 keV	30 nA	1
	8	unk 33	JEOL 733	8/26/2003	15 keV	30 nA	1
	9	-----------	JEOL 733	8/25/2003	-----------	-----------	-----------
	10	-----------	JEOL 733	8/26/2003	-----------	-----------	-----------
	11	none	JEOL 733	none	-----------	-----------	-----------
	12	none	JEOL 733	none	-----------	-----------	-----------
	13	none	JEOL 733	none	-----------	-----------	-----------
	14	-----------	JEOL 733	8/25/2003	-----------	-----------	-----------
	15	-----------	JEOL 733	8/26/2003	-----------	-----------	-----------
	16	-----------	JEOL 733	8/26/2003	-----------	-----------	-----------
	17	-----------	JEOL 733	8/26/2003	-----------	-----------	-----------
2) Mauna Kea	1	unk 8	JEOL 733	12/17/2003	15 keV	30 nA	1
post-shield flows	2	unk 9	JEOL 733	12/17/2003	15 keV	30 nA	1
hawaiite & mugearite	3	none	JEOL 733	none	-----------	-----------	-----------
16J-30, 16G1-30	4	none	JEOL 733	none	-----------	-----------	-----------
	5	unk 12	JEOL 733	12/11/2003	15 keV	30 nA	1
	6	unk 13	JEOL 733	12/11/2003	15 keV	30 nA	1
	7	unk 9	JEOL 733	12/12/2003	15 keV	30 nA	1
3) ALHA 77005	1	a	Cameca SX100	6/13/2006	15 keV	10 nA	5
lherzolitic shergottite	2	g	Cameca SX100	none	-----------	-----------	-----------
,51 & ,34	3	f	Cameca SX100	6/27/2006	15 keV	10 nA	5
	4	c	Cameca SX100	6/13/2008	15 keV	10 nA	5
	5	h	Cameca SX100	6/27/2006	15 keV	10 nA	5

* regarding the repeated Raman traverses, the corresponding probe data are listed with the original traverse (see text and Appendix I)

**JEOL 733 located at Washington University, St. Louis, MO; Cameca SX100 at JSC in Houston, TX.

Table 2. EMP analyses acquired along manual traverse 2 of the Lunar Crater phenocryst going from olivine into alteration.

line #	55	56	61	62	63	64	65
distance*:	50 µm	45 µm	20 µm	15 µm	10 µm	5 µm	0 µm
notes:	alteration	alteration	alteration	alteration	alteration	alt. front	olivine
corr spectra:**	~01223119	~01223122	~01223138	=01223139	~01223140	=01223144	~01223145
FeO	41.298	42.960	45.286	47.313	38.018	34.882	34.122
MgO	16.475	14.927	14.088	12.284	19.376	27.201	29.005
Cr_2O_3	0.000	0.008	0.000	0.000	0.000	0.000	0.000
TiO_2	0.070	0.055	0.025	0.051	0.053	0.042	0.032
MnO	0.631	0.702	0.712	0.818	0.644	0.662	0.568
V_2O_3	0.044	0.087	0.123	0.123	0.085	0.040	0.061
Al_2O_3	0.627	0.906	0.491	0.686	0.187	0.000	0.000
CaO	0.993	1.107	1.146	1.315	0.797	0.361	0.304
ZnO	0.000	0.070	0.067	0.006	0.172	0.000	0.092
SiO_2	29.931	28.589	27.772	26.868	32.364	35.697	36.179
Totals	**90.069**	**89.411**	**89.710**	**89.465**	**91.695**	**98.884**	**100.364**
Fe^{2+}/Fe^{3+}***	0.0001	0.0001	0.0001	0.0001	0.0001	10000.0	1000.0
FeO	0.004	0.004	0.005	0.005	0.004	34.879	34.088
Fe_2O_3	45.891	47.737	50.322	52.575	42.245	0.004	0.038
corr total	**94.666**	**94.192**	**94.751**	**94.730**	**95.926**	**98.884**	**100.368**
Si	0.646	0.626	0.611	0.597	0.677	1.004	0.997
Al	0.016	0.023	0.013	0.018	0.005	0.000	0.000
Ti	0.001	0.001	0.000	0.001	0.001	0.001	0.001
V	0.001	0.002	0.002	0.002	0.001	0.001	0.001
Cr	0.000	0.000	0.000	0.000	0.000	0.000	0.000
Fe^{3+}	0.745	0.787	0.834	0.880	0.665	0.000	0.001
Fe^{+2}	0.000	0.000	0.000	0.000	0.000	0.821	0.786
Mn	0.012	0.013	0.013	0.015	0.011	0.016	0.013
Mg	0.530	0.487	0.462	0.407	0.605	1.141	1.192
Zn	0.000	0.001	0.001	0.000	0.003	0.000	0.002
Ca	0.023	0.026	0.027	0.031	0.018	0.011	0.009
sum oct.	1.327	1.341	1.353	1.355	1.309	1.990	2.004
sum tet.	0.646	0.626	0.611	0.597	0.677	1.004	0.997
Total cations	**1.973**	**1.967**	**1.964**	**1.952**	**1.986**	**2.994**	**3.001**
Mg# of ol	**0.979**	**0.974**	**0.972**	**0.963**	**0.981**	**0.577**	**0.599**

* 'distance along traverse' is reported according to the spacing of points set during acquisition of probe data = 5 µm.

** corresponding spectra shown in Figure 9.

*** all Fe in olivine assumed to be in 2+ state, all Fe in alteration 3+ state;

Note: Olivine data reduced using 4 oxygens per formula unit, alteration data reduced using 3 oxygens per formula unit in goethite.

Mn included in calculation of Mg# = $Mg/(Mg+Fe^{2+}+Mn)$

Table 3. EMP analyses acquired along manual traverse 5 of a Mauna Kea phenocryst going from oli

line #	131	132	133	136	138
distance*:	0 µm	10 µm	20 µm	50 µm	70 µm
notes:	olivine	alteration	alteration	alteration	alteration
corr spectra:**	09080455	09080459	09080463	09080475	09080483
FeO	19.112	26.580	26.746	25.826	33.834
MgO	40.460	32.763	31.941	34.049	24.961
Cr_2O_3	0.000	0.000	0.033	0.004	0.000
TiO_2	0.035	0.033	0.051	0.094	0.052
MnO	0.292	0.450	0.466	0.502	0.731
V_2O_3	0.000	0.000	0.001	0.000	0.000
Al_2O_3	0.000	1.051	0.956	0.217	0.356
CaO	0.150	0.228	0.211	0.219	0.310
ZnO	0.067	0.000	0.000	0.024	0.028
SiO_2	38.173	33.316	34.350	35.891	33.213
Total	98.290	94.421	94.755	96.825	93.485
Fe^{2+}/Fe^{3+}***	53.90	6.47	24.33	29.73	10000.0
FeO	18.76	23.02	25.69	24.99	33.83
Fe_2O_3	0.39	3.95	1.17	0.93	0.00
corr total	**98.3**	**94.8**	**94.9**	**96.9**	**93.5**
Si	0.996	0.940	0.971	0.985	0.994
Al	0.000	0.035	0.032	0.007	0.013
Ti	0.001	0.001	0.001	0.002	0.001
V	0.000	0.000	0.000	0.000	0.000
Cr	0.000	0.000	0.001	0.000	0.000
Fe^{3+}	0.008	0.084	0.025	0.019	0.000
Fe^{+2}	0.409	0.543	0.607	0.574	0.847
Mn	0.006	0.011	0.011	0.012	0.019
Mg	1.574	1.379	1.346	1.394	1.114
Zn	0.001	0.000	0.000	0.000	0.001
Ca	0.004	0.007	0.006	0.006	0.010
sum oct.	2.003	2.059	2.029	2.014	2.004
sum tet.	0.996	0.940	0.971	0.985	0.994
Total cations	**3.000**	**3.000**	**3.000**	**3.000**	**2.998**
Mg# of ol	**0.791**	**0.713**	**0.685**	**0.704**	**0.563**

* 'distance along traverse' is reported according to the spacing of points set during acquisition of prol

** corresponding spectra shown in Figure 13.

*** Fe^{2+}/Fe^{3+} ratio varied to satisfy stoichiometry (sum oct = 2.0), all Fe in unaltered olivine should b

Note: Mn included in calculation of Mg#

Table 4. EMP analyses acquired along manual traverse 1 on ALHA 77005,51 going from olivine into alteration.

line #	pt 54	pt 56	pt 57	pt 59	pt 60	pt 61	pt 63	pt 66	pt 70	pt 77
distance*:	61.48 µm	63.8 µm	64.96 µm	67.28 µm	68.44 µm	69.6 µm	71.92 µm	75.4 µm	80.04 µm	88.16 µm
phase id.:	iddingsite	iddingsite	olivine	olivine	olivine	olivine	iddingsite	iddingsite	jarosite	Si-rich alt
corr spectra:**	05260812	05250814	05250815	05260817	05260818	05260820	05260822	05260824	-----------	05260838
FeO	17.735	17.867	23.096	23.653	23.120	22.597	19.333	17.794	20.986	8.628
MgO	18.497	19.913	31.700	34.834	35.008	35.415	24.158	1.222	1.495	1.485
Cr_2O_3	0.097	0.076	0.087	0.059	0.024	0.020	0.016	0.250	0.819	0.529
TiO_2	0.163	0.025	0.025	0.124	0.000	0.000	0.013	0.075	0.000	0.090
MnO	0.343	0.357	0.423	0.552	0.469	0.465	0.130	0.086	0.177	0.000
V_2O_3	0.000	0.105	0.190	0.000	0.000	0.000	0.000	0.228	0.000	0.000
Al_2O_3	0.460	0.868	0.150	0.073	0.172	0.070	0.155	0.303	0.689	0.371
CaO	0.109	0.109	0.176	0.191	0.193	0.131	0.072	0.051	0.128	0.048
Na_2O	0.000	0.014	0.007	0.002	0.014	0.052	0.026	0.085	0.382	0.067
K_2O	0.000	0.006	0.009	0.000	0.011	0.057	0.393	1.638	3.157	0.642
ZnO	0.000	0.000	0.000	0.173	0.033	0.033	0.185	0.000	0.000	0.100
SiO_2	53.509	49.962	41.311	37.721	37.209	38.446	44.715	58.263	42.285	71.817
NiO	0.069	0.015	0.099	0.034	0.099	0.000	0.107	0.057	0.000	0.000
P_2O_5	0.031	0.000	0.024	0.067	0.018	0.008	0.030	0.119	0.544	0.290
SO_3***	0.605	0.306	0.147	0.024	0.000	0.094	1.512	6.952	15.565	4.667
F	0.102	0.168	0.000	0.000	0.000	0.031	0.000	0.428	0.000	0.311
Cl	0.149	0.071	0.028	0.000	0.000	0.025	0.139	0.196	0.124	0.073
Total	**91.869**	**89.863**	**97.472**	**97.507**	**96.369**	**97.443**	**90.985**	**87.748**	**86.351**	**89.117**
-O = F	0.043	0.071	0.000	0.000	0.000	0.013	0.000	0.180	0.000	0.131
-O = Cl	0.034	0.016	0.006	0.000	0.000	0.006	0.031	0.044	0.028	0.016
New Total	**91.793**	**89.776**	**97.466**	**97.507**	**96.369**	**97.424**	**90.954**	**87.524**	**86.323**	**88.969**
Fe^{2+}/Fe^{3+}****	525	1000	390	2050	3000	1270	1000000	125	70.9805	46
FeO	17.70	17.85	23.04	23.64	23.11	22.58	19.33	17.65	20.694	8.44
Fe_2O_3	0.04	0.02	0.07	0.01	0.01	0.02	0.00	0.16	0.324	0.20
corr total	**91.797**	**89.778**	**97.472**	**97.508**	**96.370**	**97.426**	**90.954**	**87.540**	**86.356**	**88.990**
Si	1.049	1.012	1.095	1.016	1.012	1.027	0.917	1.139	3.192	1.287
Al	0.011	0.021	0.005	0.002	0.006	0.002	0.004	0.007	0.061	0.008
Ti	0.002	0.000	0.000	0.003	0.000	0.000	0.000	0.001	0.000	0.001
V	0.000	0.002	0.004	0.000	0.000	0.000	0.000	0.004	0.000	0.000
Cr	0.002	0.001	0.002	0.001	0.001	0.000	0.000	0.004	0.049	0.007
Fe^{+3}	0.088	0.048	0.209	0.041	0.028	0.063	0.000	0.369	2.939	0.439
Fe^{+2}	0.290	0.302	0.511	0.532	0.526	0.504	0.332	0.289	1.306	0.127
Mn	0.006	0.006	0.009	0.013	0.011	0.011	0.002	0.001	0.011	0.000
Mg	0.540	0.601	1.252	1.398	1.420	1.410	0.738	0.036	0.168	0.040
Zn	0.000	0.000	0.000	0.003	0.001	0.001	0.003	0.000	0.000	0.001
Ca	0.002	0.002	0.005	0.005	0.006	0.004	0.002	0.001	0.010	0.001
Na	0.000	0.001	0.000	0.000	0.001	0.003	0.001	0.003	0.056	0.002
K	0.000	0.000	0.000	0.000	0.000	0.002	0.010	0.041	0.304	0.015
Ni	0.001	0.000	0.002	0.001	0.002	0.000	0.002	0.001	0.000	0.000
P	0.001	0.000	0.001	0.002	0.000	0.000	0.001	0.002	0.035	0.004
S	0.009	0.005	0.003	0.000	0.000	0.002	0.023	0.102	0.882	0.063
F	0.006	0.011	0.000	0.000	0.000	0.003	0.000	0.026	0.000	0.018
Cl	0.005	0.002	0.001	0.000	0.000	0.001	0.005	0.006	0.016	0.002
for olivine:										
sum oct			2.000	2.000	2.000	2.000				
sum tet			1.098	1.018	1.013	1.029				
Total cations			3.099	3.018	3.012	3.029				
for sulfate:										
A cations									1.856	
B cations									3.000	
X cations									4.157	
Total cations									9.013	
for iddingsite:										
Total cations	2.000	2.002					2.035	2.000		1.996
Mg#	0.646	0.661	0.707	0.720	0.726	0.733	0.689	0.109	0.113	0.239

* 'distance along traverse' is reported according to the spacing of points set during acquisition of probe data = 1.16 µm; alteration front located at spectrum 05260822 (pt. 63).

** corresponding spectra shown in Figure 17.

***analyzed as SO_2 and converted to SO_3 by multiplying by (80.0642/64.0648 = 1.24973776551242)

****Fe^{2+}/Fe^{3+} ratios varied to satisfy stoichiometry; to bring sum oct to 2.0 for olivine and sum B as close to 3.0 as possible for sulfate

Notes: 1) Mn included in calculation of Mg# = Mg/(Mg+Fe^{2+}+Mn), 2) olivine analyses reduced using 4 oxygens per formula unit, jarosite using 11 oxygens, and iddingsite 3 oxygens.

3) oxide sums for olivine (analyses having 36-38 wt% SiO_2): oct = (Al, Ti, V, Cr, Fe^{2+}, Fe^{3+}, Mn, Mg, Zn, Ca, Na, K, Ni), tet = (Si, P, S);

oxide sums for sulfate (analyses having > 10 wt% SO_3): A = (Fe^{2+}, Mn, Mg, Ca, Na, K, Ni), B = (Al, Ti, Fe^{3+}); X = (Si, P, S, Cr);

oxide sums for iddingsite alteration (SiO_2 > 39 wt% and oxide totals < 95 %) include all cations

Table 5a. EMP analyses of chromites in ALHA 77005,51 with their alteration products.

chromite #:	chr 7					chr 8					chr 9				
point:	pt 1	pt 2	pt 3	pt 4	pt 5	pt 1	pt 2	pt 3	pt 4	pt 5	pt 1	pt 2	pt 3	pt 4	pt 5
line #	27 / 1 .	28 / 1 .	29 / 1 .	30 / 1 .	31 / 1 .	32 / 1 .	33 / 1 .	34 / 1 .	35 / 1 .	36 / 1 .	37 / 1 .	38 / 1 .	39 / 1 .	40 / 1 .	41 / 1 .
phase id:	chr	chr	alt	chr	alt	alt	chr	chr	chr	alt	chr	chr	alt	alt	alt
for location see:	pic 29	pic 29	pic 29	pic 29	pic 29	see t.s. map	see t.s. map	see t.s. map	see t.s. map	see t.s. map	pic 30	pic 30	pic 30	pic 30	pic 30
FeO	30.595	28.597	27.946	27.931	26.841	31.838	24.831	24.789	25.377	30.352	29.378	29.958	21.684	20.582	39.269
MgO	6.364	6.077	0.293	6.165	0.861	0.189	6.245	5.997	6.216	0.218	6.050	6.489	5.228	0.147	0.241
Cr_2O_3	43.613	47.898	17.548	48.673	16.615	9.457	56.165	57.300	56.545	9.129	41.522	37.630	6.871	6.671	3.893
TiO_2	5.890	3.678	1.513	4.169	4.889	0.949	1.084	0.591	1.233	0.687	3.945	4.338	0.535	0.337	0.102
MnO	0.466	0.358	0.236	0.454	0.246	0.287	0.488	0.230	0.397	0.394	0.351	0.433	0.159	0.000	0.159
V_2O_3	1.482	1.525	0.863	1.318	1.263	0.804	1.171	1.137	1.045	0.762	1.248	1.335	0.000	0.000	0.000
Al_2O_3	9.003	8.304	1.121	8.538	1.541	0.791	7.237	6.359	6.771	1.189	15.248	17.347	5.158	1.269	0.396
CaO	0.106	0.046	0.065	0.062	0.173	0.162	0.029	0.030	0.015	0.090	0.083	0.021	0.550	0.050	0.075
Na_2O	0.016	0.022	0.331	0.000	0.161	0.143	0.016	0.016	0.003	0.135	0.000	0.000	0.875	0.895	0.535
K_2O	0.011	0.000	4.386	0.021	2.484	3.409	0.011	0.022	0.054	3.366	0.024	0.000	1.961	2.069	4.362
ZnO	0.070	0.000	0.000	0.151	0.030	0.000	0.000	0.000	0.228	0.070	0.170	0.301	0.000	0.124	0.000
SiO_2	0.086	0.058	0.616	0.112	3.353	5.468	0.039	0.115	0.108	6.467	0.072	0.006	22.157	30.619	2.968
NiO	0.071	0.000	0.061	0.050	0.018	0.112	0.011	0.028	0.032	0.104	0.014	0.047	0.000	0.018	0.004
P_2O_5	0.000	0.000	0.356	0.000	1.748	1.782	0.026	0.018	0.000	2.730	0.000	0.000	1.177	1.187	0.933
SO_3*	0.075	0.115	14.898	0.137	13.076	16.895	0.000	0.027	0.000	17.559	0.041	0.104	14.761	16.474	18.599
Cl	0.046	0.000	0.132	0.000	0.194	0.042	0.016	0.008	0.000	0.081	0.008	0.000	0.053	0.041	0.094
Total	**97.895**	**96.678**	**70.366**	**97.782**	**73.494**	**72.327**	**97.369**	**96.667**	**98.024**	**73.333**	**98.155**	**98.009**	**81.168**	**80.483**	**71.630**
-O = Cl	0.010	0.000	0.030	0.000	0.044	0.009	0.004	0.002	0.000	0.018	0.002	0.000	0.012	0.009	0.021
New Total	**97.884**	**96.678**	**70.336**	**97.782**	**73.450**	**72.318**	**97.365**	**96.666**	**98.024**	**73.315**	**98.154**	**98.009**	**81.156**	**80.474**	**71.609**
Fe^{2+}/Fe^{3+}**	11.300	11.300	0.00001	23.900	0.00001	0.00001	16.0	15.4	12.3	0.00001	17.3	12.4	0.00001	0.000001	0.1537
FeO	28.107	26.272	0.000	26.810	0.000	0.000	23.370	23.278	23.469	0.000	27.773	27.723	0.000	0.000	5.232
Fe_2O_3	2.764	2.584	31.056	1.247	29.829	35.381	1.623	1.680	2.120	33.730	1.784	2.485	24.097	22.873	37.826
corr total	**98.161**	**96.936**	**73.447**	**97.907**	**76.438**	**75.862**	**97.528**	**96.834**	**98.236**	**76.693**	**98.332**	**98.258**	**83.570**	**82.765**	**75.398**
Si	0.003	0.002	0.067	0.004	0.340	0.543	0.001	0.004	0.004	0.621	0.0024	0.0002	1.7919	2.4066	0.3070
Al	0.368	0.345	0.144	0.350	0.184	0.093	0.300	0.267	0.279	0.135	0.6057	0.6816	0.4917	0.1175	0.0483
Ti	0.153	0.097	0.124	0.109	0.372	0.071	0.029	0.016	0.032	0.050	0.1000	0.1088	0.0325	0.0199	0.0079
V	0.041	0.043	0.076	0.037	0.103	0.064	0.033	0.032	0.029	0.059	0.0337	0.0357	0.0000	0.0000	0.0000
Cr	1.195	1.334	1.514	1.340	1.331	0.742	1.561	1.613	1.566	0.693	1.1065	0.9919	0.4393	0.4146	0.3183
Fe^{+3}	0.072	0.068	2.551	0.033	2.274	2.642	0.043	0.045	0.056	2.438	0.0452	0.0623	1.4665	1.3528	2.9438
Fe^{+2}	0.814	0.774	0.000	0.781	0.000	0.000	0.687	0.693	0.687	0.000	0.7828	0.7729	0.0000	0.0000	0.4525
Mn	0.014	0.011	0.022	0.013	0.021	0.024	0.015	0.007	0.012	0.032	0.0100	0.0122	0.0109	0.0000	0.0139
Mg	0.329	0.319	0.048	0.320	0.130	0.028	0.327	0.318	0.324	0.031	0.3040	0.3225	0.6303	0.0173	0.0371
Zn	0.002	0.000	0.000	0.004	0.002	0.000	0.000	0.000	0.006	0.005	0.0042	0.0074	0.0000	0.0072	0.0000
Ca	0.004	0.002	0.008	0.002	0.019	0.017	0.001	0.001	0.001	0.009	0.0030	0.0007	0.0477	0.0042	0.0083
Na	0.001	0.002	0.070	0.000	0.032	0.028	0.001	0.001	0.000	0.025	0.0000	0.0000	0.1372	0.1364	0.1073
K	0.000	0.000	0.611	0.001	0.321	0.432	0.000	0.001	0.002	0.413	0.0010	0.0000	0.2023	0.2075	0.5755
Ni	0.002	0.000	0.005	0.001	0.001	0.009	0.000	0.001	0.001	0.008	0.0004	0.0013	0.0000	0.0011	0.0003
P	0.000	0.000	0.033	0.000	0.150	0.150	0.001	0.001	0.000	0.222	0.0000	0.0000	0.0806	0.0790	0.0817
S	0.002	0.003	1.220	0.004	0.994	1.258	0.000	0.001	0.000	1.266	0.0010	0.0026	0.8959	0.9717	1.4435
Cl	0.003	0.000	0.024	0.000	0.033	0.007	0.001	0.000	0.000	0.013	0.0005	0.0000	0.0073	0.0055	0.0165
for sulfate:* **															
sum A			0.763		0.524	0.537				0.518			1.028	0.366	1.195
sum B			2.895		2.935	2.869				2.686			1.991	1.497	3.000
sum X			2.835		2.814	2.692				2.803			3.208	3.872	2.150
Total cations			6.492		6.273	6.098				6.007			6.227	5.736	6.345
for chromite:															
sum 1, 2+	1.166	1.107		1.123			1.032	1.022	1.034		1.105	1.117			
sum 3, 4+	1.832	1.890		1.873			1.967	1.977	1.966		1.894	1.880			
Total cations	3.000	3.000		3.000			3.000	3.000	3.000		3.000	3.000			
opaque end members (in %)															
$(Al+Ti+Cr+Fe^{3+}+Mg$	1.04	1.04		1.04			1.07	1.07	1.08		0.98	0.97			
% mgt	3.45	3.28		1.57			2.01	2.10	2.60		2.31	3.22			
% chr	57.3	63.9		64.2			73.0	75.3	72.8		56.5	51.3			
% ulvo	14.7	9.33		10.5			2.68	1.48	3.02		10.2	11.2			
% spinel	24.6	23.5		23.7			22.3	21.1	21.6		31.0	34.3			

*analyzed as SO_2 and converted to SO_3 by multiplying by (80.0642/64.0648 = 1.24973776551242)

**Fe^{2+}/Fe^{3+} of chromite was varied to bring cation total to 3.0000, but set = 0.0001 for alteration because jarosite should only have Fe^{3+}

***Chromite data reduced assuming 4 oxygens per formula unit and the sulfate data using 11 oxygens per formula unit (assuming jarosite).

sulfate sums: A = Fe^{2+} + Mn + Mg + Ca + Na + K + Ni, B = Al + Ti + V + Zn + Fe^{3+}, X = Si + Cr + S + P

chromite sums: 1,2+ = Fe^{2+} + Mn + Mg + Zn + Ca + Na + K + Ni; 3,4+ = Si + Al + Ti + V + Cr + Fe^{3+}

Table 5a. cont'd																	
chromite #:	chr 12					chr 30					chr 33						
point:	pt 1	pt 2	pt 3	pt 4	pt 5	pt 1	pt 2	pt 3	pt 4	pt 5	pt 1	pt 2	pt 3	pt 4	pt 5	pt 6	pt 7
line #	1 / 1 .	2 / 1 .	3 / 1 .	4 / 1 .	5 / 1 .	5 / 1 .	6 / 1 .	7 / 1 .	8 / 1 .	9 / 1 .	12 / 1 .	13 / 1 .	14 / 1 .	15 / 1 .	16 / 1 .	17 / 1 .	18 / 1 .
phase id:	alt	alt	alt	chr	chr	chr	chr	alt	alt	alt	alt	alt	alt	alt	alt	chr	chr
for location see:	pic 37	pic 37	pic 37	pic 37	pic 37	pic 31	pic 31	pic 31	pic 31	pic 31	pic 33	pic 33	pic 33	pic 33	pic 33	pic 33	pic 33
FeO	33.104	33.969	34.408	26.093	26.331	28.760	29.044	30.703	30.553	30.402	35.888	35.682	29.275	31.995	27.551	26.307	27.092
MgO	0.168	0.173	0.191	5.502	5.541	5.074	5.323	0.230	0.218	0.244	0.234	0.591	0.673	0.444	0.218	5.447	5.676
Cr_2O_3	7.563	8.585	7.991	54.476	54.520	45.913	44.790	6.214	4.165	3.017	3.579	4.503	7.207	9.084	3.975	53.885	50.925
TiO_2	0.889	0.870	0.871	1.105	0.916	2.204	2.056	0.637	0.645	0.402	0.479	0.422	0.810	0.217	0.442	1.480	1.297
MnO	0.278	0.143	0.137	0.467	0.419	0.419	0.307	0.203	0.147	0.052	0.090	0.029	0.039	0.066	0.117	0.596	0.331
V_2O_3	0.514	0.559	0.670	1.300	1.454	1.401	1.132	0.465	0.000	0.215	0.143	0.207	0.120	0.178	0.184	1.207	0.788
Al_2O_3	0.665	0.623	0.610	7.091	7.050	12.715	12.763	1.165	0.524	0.518	0.546	0.563	1.365	1.545	4.199	7.841	8.874
CaO	0.274	0.203	0.314	0.067	0.045	0.145	0.101	0.236	0.130	0.213	0.205	0.085	0.223	2.180	0.252	0.091	0.128
Na_2O	0.179	0.132	0.083	0.000	0.006	0.000	0.000	1.108	1.065	0.727	0.442	0.458	1.305	0.739	0.997	0.000	0.016
K_2O	3.571	2.242	2.689	0.017	0.036	0.028	0.020	4.953	4.779	5.655	2.532	2.377	3.087	2.735	3.536	0.034	0.010
ZnO	0.000	0.069	0.000	0.206	0.000	0.029	0.020	0.112	0.000	0.051	0.030	0.100	0.115	0.000	0.000	0.111	0.080
SiO_2	3.698	2.516	1.845	0.105	0.146	0.171	0.123	16.688	15.583	16.539	1.698	1.045	17.592	1.803	10.374	0.052	0.106
NiO	0.029	0.000	0.000	0.000	0.060	0.095	0.109	0.058	0.000	0.112	0.000	0.000	0.015	0.000	0.103	0.004	0.057
P_2O_5	1.902	2.225	2.189	0.000	0.006	0.000	0.000	1.551	1.706	1.812	2.588	2.097	2.888	1.383	1.224	0.000	0.021
SO_3*	17.096	17.326	18.185	0.227	0.140	0.256	0.382	17.384	17.503	17.510	20.108	19.657	13.491	18.646	15.417	0.186	0.265
Cl	0.075	0.092	0.058	0.026	0.000	0.005	0.008	0.000	0.027	0.091	0.096	0.141	0.026	0.348	0.162	0.000	0.027
Total	**70.004**	**69.727**	**70.242**	**96.681**	**96.669**	**97.215**	**96.179**	**81.706**	**77.044**	**77.560**	**68.658**	**67.957**	**78.232**	**71.364**	**68.751**	**97.242**	**95.693**
-O = Cl	0.017	0.021	0.013	0.006	0.000	0.001	0.002	0.000	0.006	0.021	0.022	0.032	0.006	0.079	0.037	0.000	0.006
New Total	**69.987**	**69.706**	**70.229**	**96.676**	**96.669**	**97.214**	**96.177**	**81.706**	**77.038**	**77.539**	**68.636**	**67.925**	**78.226**	**71.285**	**68.715**	**97.242**	**95.687**
Fe^{2+}/Fe^{3+}**	0.017	0.048	0.055	19.400	12.900	23.600	15.100	0.00001	0.00001	0.00001	0.068	0.091	0.000001	0.00001	0.00001	21.200	11.500
FeO	0.537	1.547	1.807	24.814	24.437	27.591	27.240	0.000	0.000	0.000	2.298	2.967	0.000	0.000	0.000	25.122	24.925
Fe_2O_3	36.191	36.031	36.230	1.421	2.105	1.299	2.005	34.120	33.953	33.786	37.328	36.357	32.534	35.556	30.618	1.317	2.409
corr total	**73.612**	**73.315**	**73.858**	**96.818**	**96.880**	**97.344**	**96.378**	**85.123**	**80.439**	**80.923**	**72.375**	**71.566**	**81.485**	**74.846**	**71.781**	**97.374**	**95.928**
Si	0.381	0.260	0.190	0.004	0.005	0.006	0.004	1.408	1.382	1.455	0.174	0.110	1.544	0.182	1.038	0.002	0.004
Al	0.081	0.076	0.074	0.298	0.296	0.519	0.524	0.116	0.055	0.054	0.066	0.070	0.141	0.184	0.495	0.326	0.372
Ti	0.069	0.068	0.067	0.030	0.025	0.057	0.054	0.040	0.043	0.027	0.037	0.033	0.053	0.016	0.033	0.039	0.035
V	0.042	0.046	0.055	0.037	0.041	0.039	0.032	0.031	0.000	0.015	0.012	0.017	0.008	0.014	0.015	0.034	0.022
Cr	0.616	0.702	0.650	1.534	1.534	1.256	1.235	0.414	0.292	0.210	0.290	0.374	0.500	0.726	0.315	1.504	1.432
Fe^{+3}	2.808	2.805	2.803	0.038	0.056	0.034	0.053	2.166	2.265	2.236	2.883	2.872	2.148	2.705	2.306	0.035	0.064
Fe^{+2}	0.046	0.134	0.155	0.739	0.727	0.799	0.794	0.000	0.000	0.000	0.197	0.260	0.000	0.000	0.000	0.742	0.741
Mn	0.024	0.013	0.012	0.014	0.013	0.012	0.009	0.015	0.011	0.004	0.008	0.003	0.003	0.006	0.010	0.018	0.010
Mg	0.026	0.027	0.029	0.292	0.294	0.262	0.277	0.029	0.029	0.032	0.036	0.092	0.088	0.067	0.032	0.287	0.301
Zn	0.000	0.005	0.000	0.005	0.000	0.001	0.001	0.007	0.000	0.003	0.002	0.008	0.007	0.000	0.000	0.003	0.002
Ca	0.030	0.023	0.035	0.003	0.002	0.005	0.004	0.021	0.012	0.020	0.023	0.010	0.021	0.236	0.027	0.003	0.005
Na	0.036	0.026	0.017	0.000	0.000	0.000	0.000	0.181	0.183	0.124	0.088	0.093	0.222	0.145	0.193	0.000	0.001
K	0.470	0.296	0.353	0.001	0.002	0.001	0.001	0.533	0.541	0.635	0.332	0.318	0.346	0.353	0.451	0.002	0.000
Ni	0.002	0.000	0.000	0.000	0.002	0.003	0.003	0.004	0.000	0.008	0.000	0.000	0.001	0.000	0.008	0.000	0.002
P	0.166	0.195	0.191	0.000	0.000	0.000	0.000	0.111	0.128	0.135	0.225	0.186	0.215	0.118	0.104	0.000	0.001
S	1.323	1.345	1.403	0.006	0.004	0.007	0.010	1.101	1.165	1.156	1.549	1.549	0.888	1.415	1.158	0.005	0.007
Cl	0.013	0.016	0.010	0.002	0.000	0.000	0.000	0.000	0.004	0.014	0.017	0.025	0.004	0.060	0.027	0.000	0.002
for sulfate:*																	
sum A	0.634	0.518	0.600					0.783	0.776	0.822	0.683	0.777	0.681	0.806	0.723		
sum B	3.000	3.000	3.000					2.361	2.363	2.335	3.000	3.000	2.359	2.920	2.849		
sum X	2.487	2.502	2.433					3.034	2.966	2.955	2.238	2.218	3.146	2.442	2.615		
Total cations	6.121	6.020	6.034					6.178	6.106	6.113	5.921	5.995	6.186	6.168	6.187		
for chromite:																	
sum 1, 2+				1.054	1.039	1.083	1.088									1.054	1.063
sum 3, 4+				1.940	1.957	1.911	1.902									1.941	1.930
Total cations				3.000	3.000	3.000	3.000									3.000	3.000
opaque end members (in %)																	
$(Al+Ti+Cr+Fe^{3+}+Mg)$				1.04	1.04	0.96	0.97									1.03	1.03
% mgt				1.84	2.71	1.76	2.72									1.69	3.14
% chr				74.03	73.71	65.2	63.8									72.7	69.8
% ulvo				2.86	2.36	5.96	5.57									3.80	3.38
% spinel				21.3	21.2	27.1	27.9									21.8	23.7

Table 5a. cont'd								
chromite #:	chr 42							
point:	pt 1	pt 2	pt 3	pt 4	pt 5	pt 6	pt 7	pt 8
line #	42 / 1 .	43 / 1 .	44 / 1 .	45 / 1 .	46 / 1 .	47 / 1 .	48 / 1 .	49 / 1 .
phase id:	alt	alt	alt	alt	alt	alt	chr	chr
for location see:	pic 47	pic 47	pic 47	pic 47	pic 47	pic 47	pic 47	pic 47
FeO	25.365	24.939	18.675	24.860	22.755	24.108	28.075	33.909
MgO	0.236	0.323	1.120	0.237	1.431	0.360	4.228	4.641
Cr_2O_3	8.709	13.038	8.142	12.752	17.221	9.094	55.484	41.749
TiO_2	6.960	7.879	4.459	8.291	5.858	17.396	1.752	7.011
MnO	0.391	0.555	0.265	0.243	0.267	0.256	0.646	0.469
V_2O_3	0.839	1.154	0.584	1.035	0.933	2.470	0.761	0.786
Al_2O_3	0.766	1.700	8.593	1.656	3.065	0.914	5.651	6.878
CaO	0.195	0.400	4.291	2.049	1.216	0.204	0.058	0.062
Na_2O	0.212	0.151	1.365	0.126	0.272	0.171	0.013	0.003
K_2O	3.141	2.162	2.823	2.967	2.576	1.924	0.022	0.000
ZnO	0.000	0.099	0.106	0.180	0.031	0.120	0.000	0.000
SiO_2	1.909	3.247	21.514	4.038	6.258	2.651	0.078	0.057
NiO	0.000	0.110	0.019	0.000	0.059	0.029	0.004	0.021
P_2O_5	2.565	0.554	1.241	0.826	2.563	5.244	0.000	0.000
SO_3*	15.990	15.382	11.069	15.429	10.964	11.956	0.014	0.046
Cl	0.176	0.047	0.032	0.104	0.193	0.133	0.000	0.003
Total	**67.454**	**71.741**	**84.298**	**74.793**	**75.662**	**77.030**	**96.787**	**95.636**
-O = Cl	0.040	0.011	0.007	0.023	0.044	0.030	0.000	0.001
New Total	**67.415**	**71.730**	**84.291**	**74.769**	**75.618**	**77.000**	**96.787**	**95.636**
Fe^{2+}/Fe^{3+}**	0.00001	0.012	0.000001	0.00001	0.000001	0.324	15.600	9.500
FeO	0.000	0.291	0.000	0.000	0.000	5.902	26.384	30.680
Fe_2O_3	28.188	27.392	20.753	27.627	25.288	20.232	1.880	3.589
corr total	**70.238**	**74.474**	**86.369**	**77.536**	**78.151**	**79.027**	**96.975**	**95.995**
Si	0.203	0.330	1.740	0.395	0.610	0.253	0.003	0.002
Al	0.096	0.204	0.819	0.191	0.352	0.103	0.241	0.293
Ti	0.556	0.602	0.271	0.609	0.429	1.248	0.048	0.191
V	0.071	0.094	0.038	0.081	0.073	0.189	0.022	0.023
Cr	0.731	1.047	0.521	0.985	1.326	0.686	1.586	1.195
Fe^{+3}	2.252	2.093	1.263	2.031	1.854	1.452	0.051	0.098
Fe^{+2}	0.000	0.025	0.000	0.000	0.000	0.471	0.798	0.929
Mn	0.035	0.048	0.018	0.020	0.022	0.021	0.020	0.014
Mg	0.037	0.049	0.135	0.034	0.208	0.051	0.228	0.250
Zn	0.000	0.007	0.006	0.013	0.002	0.008	0.000	0.000
Ca	0.022	0.044	0.372	0.214	0.127	0.021	0.002	0.002
Na	0.044	0.030	0.214	0.024	0.051	0.032	0.001	0.000
K	0.425	0.280	0.291	0.370	0.320	0.234	0.001	0.000
Ni	0.000	0.009	0.001	0.000	0.005	0.002	0.000	0.001
P	0.231	0.048	0.085	0.068	0.211	0.423	0.000	0.000
S	1.274	1.172	0.672	1.131	0.802	0.856	0.000	0.001
Cl	0.032	0.008	0.004	0.017	0.032	0.021	0.000	0.000
for sulfate:*								
sum A	0.564	0.484	1.032	0.663	0.733	0.832		
sum B	2.975	3.000	2.397	2.925	2.710	3.000		
sum X	2.438	2.597	3.017	2.579	2.949	2.218		
Total cations	5.976	6.080	6.446	6.167	6.392	6.049		
for chromite:								
sum 1, 2+							1.049	1.197
sum 3, 4+							1.950	1.802
Total cations							3.000	3.000
opaque end members (in %)								
$(Al+Ti+Cr+Fe^{3+}+Mg)$							1.04	1.04
% mgt							2.46	4.72
% chr							76.2	57.7
% ulvo							4.58	18.43
% spinel							16.7	19.2

Table 5b. EMP analyses of glass surrounding chr 42.

	50 / 1 .	51 / 1 .	52 / 1 .	53 / 1 .	54 / 1 .
	glass around	glass around	glass around	glass around	glass around
	chr 42, pt 1	chr 42, pt 2	chr 42, pt 3	chr 42, pt 4	chr 42, pt 5
	feld glass	feld glass	feld glass	glass	glass
	pic 47	pic 47	pic 47	pic 47	pic 47
FeO	3.438	0.605	0.598	6.177	8.499
MgO	1.179	0.160	0.190	5.948	4.338
Cr2O3	0.244	0.088	0.000	0.477	0.196
TiO2	0.972	0.134	0.078	3.413	3.801
MnO	0.095	0.000	0.043	0.069	0.220
V2O3	0.018	0.057	0.000	0.262	0.054
Al2O3	25.175	27.546	28.342	14.857	15.734
CaO	10.118	9.274	9.681	12.029	11.316
Na2O	3.982	4.731	4.982	2.558	2.855
K2O	0.228	0.413	0.408	0.244	0.210
ZnO	0.000	0.123	0.120	0.000	0.054
SiO2	50.360	52.331	51.453	47.094	46.211
NiO	0.034	0.000	0.004	0.058	0.000
P2O5	0.309	0.130	0.148	1.786	2.207
SO3	0.517	0.000	0.000	0.476	0.371
Cl	0.006	0.000	0.000	0.015	0.021
Total	**96.675**	**95.591**	**96.047**	**95.463**	**96.086**
-O = Cl	0.001	0.000	0.000	0.003	0.005
New Total	**96.674**	**95.591**	**96.047**	**95.459**	**96.081**
Fe2/Fe3*	5.55	100000	0.0001	0.109	0.575
FeO	2.913	0.605	0.000	0.607	3.103
Fe2O3	0.583	0.000	0.664	6.190	5.997
corrected sum	**96.732**	**95.591**	**96.114**	**96.079**	**96.682**
Si IV	2.3891	2.4680	2.4204	2.3066	2.2698
Al VI	1.4076	1.5311	1.5713	0.8576	0.9108
Ti	0.0347	0.0048	0.0028	0.1257	0.1404
V	0.0007	0.0022	0.0000	0.0103	0.0021
Cr	0.0092	0.0033	0.0000	0.0185	0.0076
Fe +3	0.0208	0.0000	0.0235	0.2281	0.2216
Fe +2	0.1156	0.0239	0.0000	0.0249	0.1274
Mn +2	0.0038	0.0000	0.0017	0.0029	0.0092
Mg	0.0834	0.0112	0.0133	0.4343	0.3176
Zn	0.0000	0.0043	0.0042	0.0000	0.0020
Ca	0.5143	0.4686	0.4879	0.6312	0.5955
Na	0.3663	0.4326	0.4544	0.2429	0.2719
K	0.0138	0.0248	0.0245	0.0152	0.0132
Ni	0.0013	0.0000	0.0002	0.0023	0.0000
P	0.0124	0.0052	0.0059	0.0741	0.0918
S	0.0184	0.0000	0.0000	0.0175	0.0137
Cl	0.0005	0.0000	0.0000	0.0012	0.0017
sum tet**	3.8275	4.0043	3.9976	3.2558	3.2860
sum oct	1.1638	0.9756	1.0124	1.7363	1.7085
total cations	**4.9912**	**4.9799**	**5.0100**	**4.9921**	**4.9945**
Or:	1.543	2.683	2.533	1.714	1.494
Ab:	40.952	46.714	46.998	27.313	30.877
An:	57.505	50.602	50.469	70.973	67.629

*Fe2/Fe3 adjusted to bring cation total as close to 5.0 as possible

**Reduced the glass surrounding chr 42 as if it were feldspathic, but only the first three points have composition of labradorite; the glass in the last two points has reacted with the chromite, the jarosite around the chromite, and the adjacent pyroxene

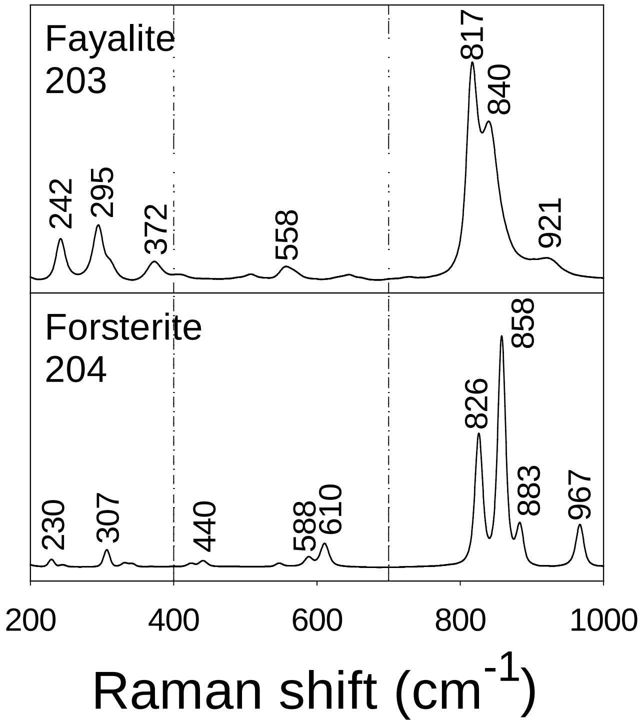

Figure 1. Raman spectra of the olivine end-members forsterite and fayalite (same as Fig. 2 of Kuebler et al., 2006).

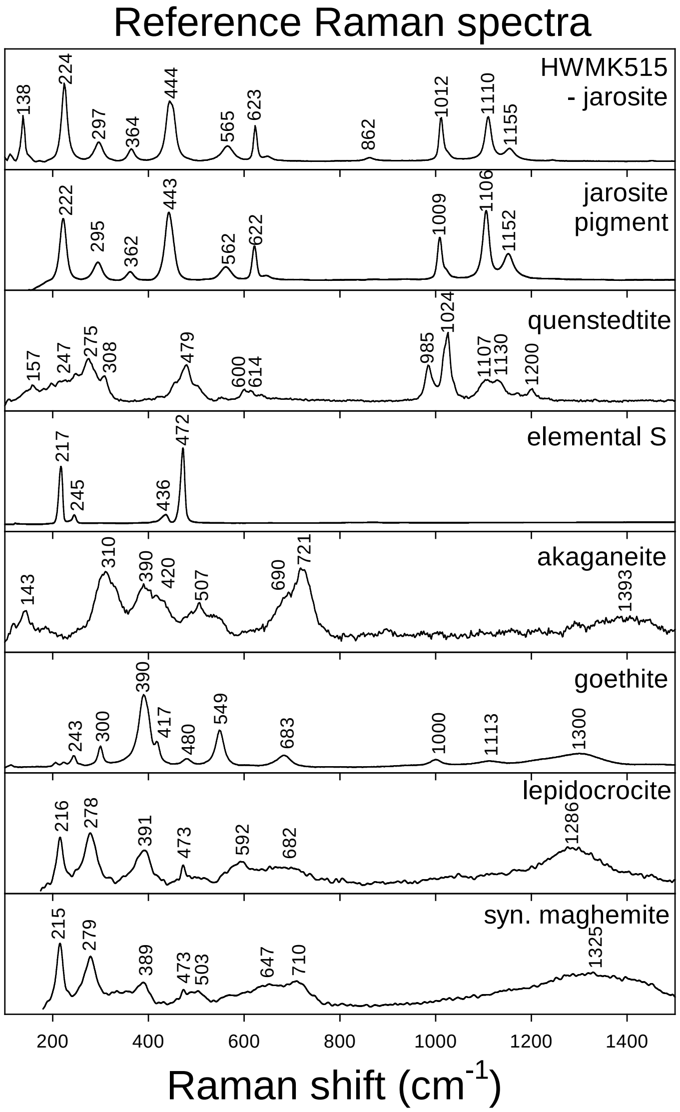

Figure 2. Standard Raman spectra of the secondary phases identified in the present study plus quenstedtite, previously reported to occur in ALHA 77005 but not found by us. The sources of the mineral standards shown here are (from top to bottom): 1 & 2) both jarosites from D. Morris and D. Ming; 3 & 4) quenstedtite and elemental S from Alian Wang; 5) akaganeite, JSC, lunar rusty rock 66055,155; 6) goethite from ASU (WAR-3674); and 7 & 8) lepidocrocite, LPS2, and syn. maghemite, MHS3, also from D. Morris. Lepidocrocite shown for reference to its polymorphs akaganeite and goethite.

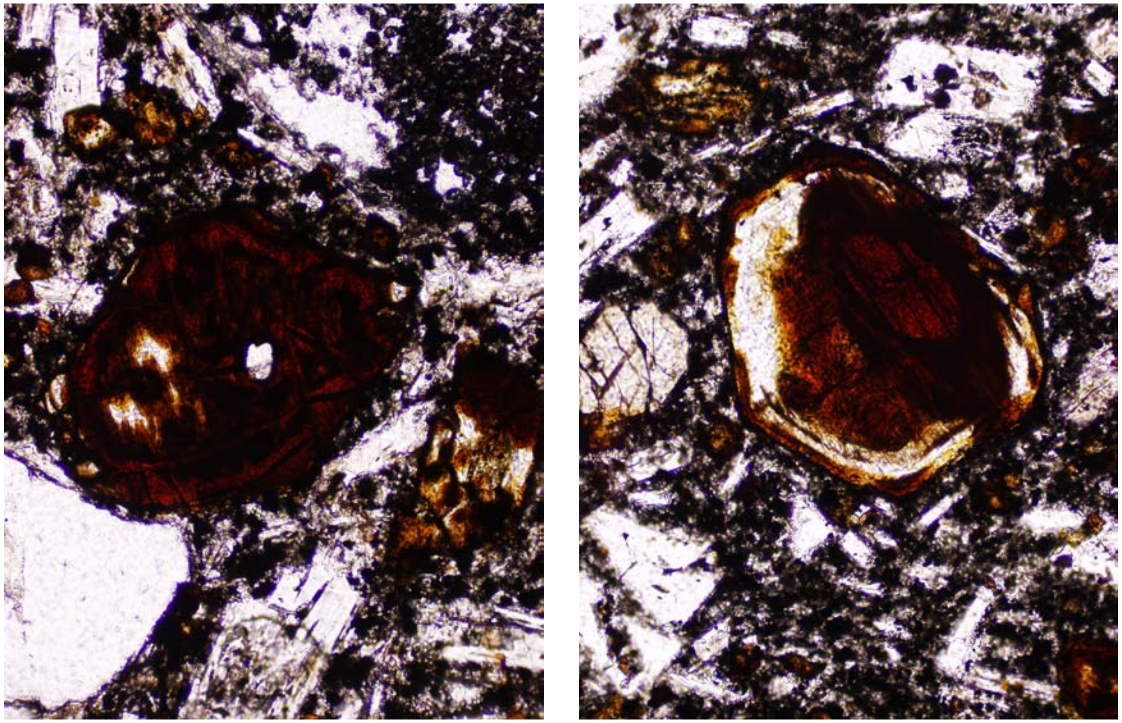

Figure 3. Altered olivine from Lunar Crater, NV; altered olivine from this locality fit the narrow definition of iddingsite. Compare these images to the iddingsite images in plates 102 and 104 of the Delvigne (1998) Atlas of Micromorphology of Weathering Products. Both images were taken with a 10x magnification.

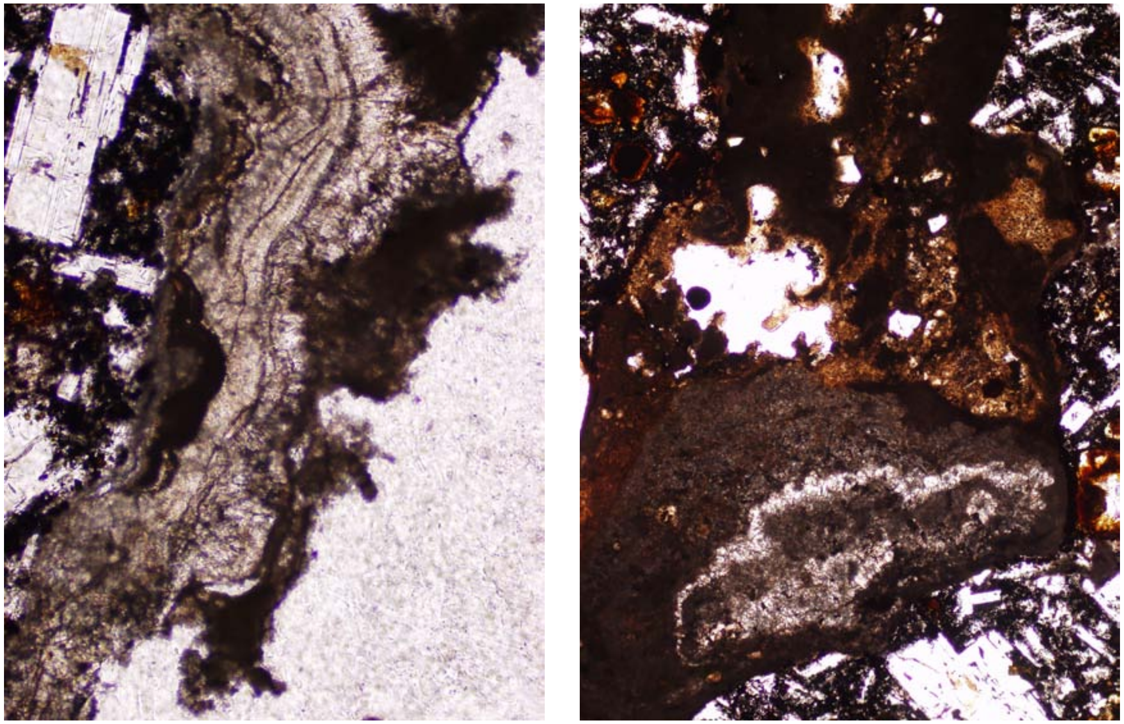

Figure 4. Examples of vesicle-filling secondary materials in Lunar Crater sample. Layered material in image at left (10x) is calcite (identified by Raman spectroscopy). Coarse materials in the image at right (5x) are also calcite. Clays are presumed to be present also, but the carbonates are too fluorescent for positive identification.

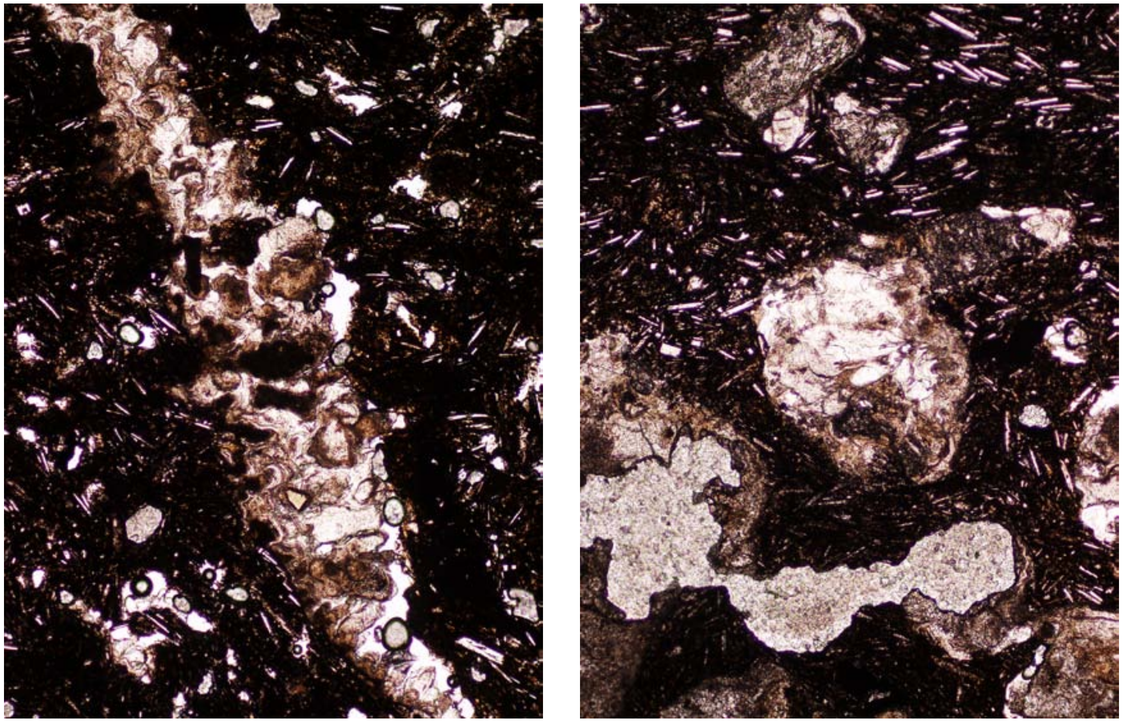

Figure 5. Examples of vesicle-filling materials in the Mauna Kea 16G1-30 sample (clay, silica, and calcite). Both photos were taken at 5x magnification. Clay compositions reported by Kristall (2000) suggest montmorillonite.

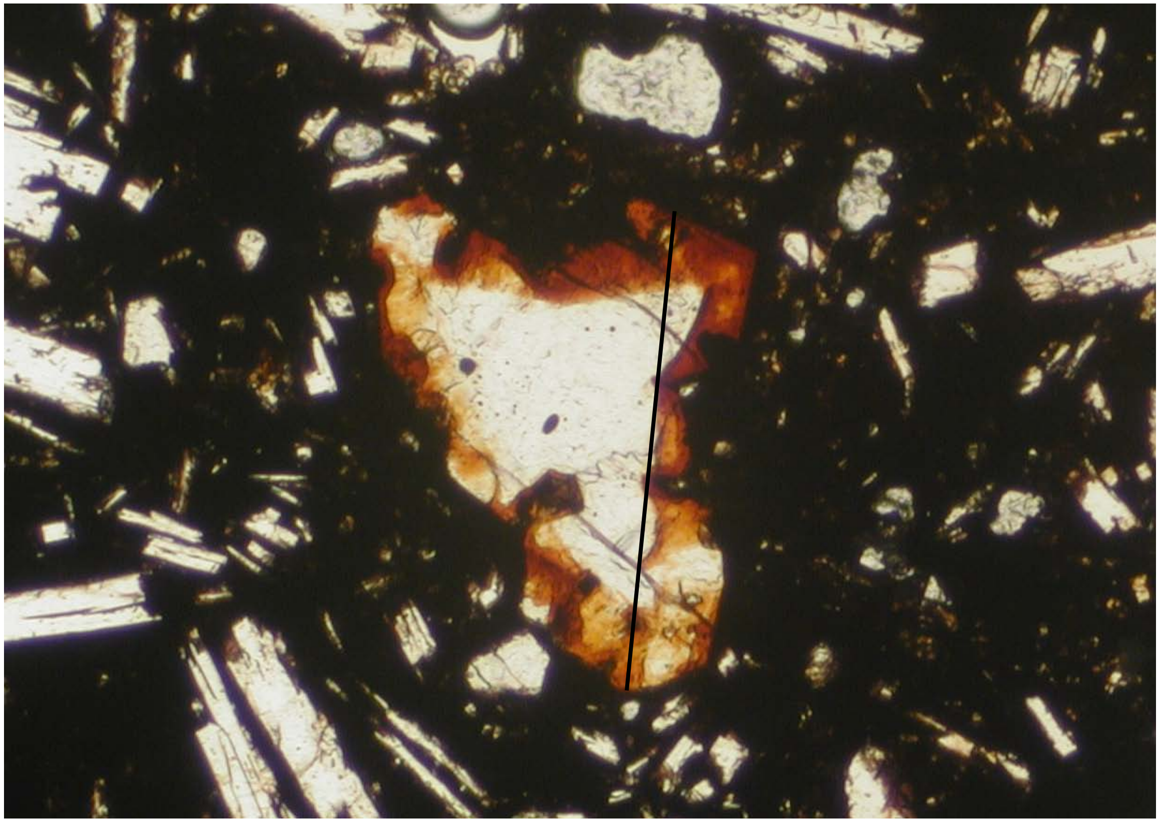

Figure 6. Typical altered olivine in the oxidized rim of Mauna Kea sample 16J-30. Compare this to the iddingsite images in plates 201 and 202 of the Delvigne (1998) Atlas of Micromorphology of Weathering Products. Traverse 5 was made on this grain; the traverse was 364 µm long, it began at the bottom edge and proceeded to the top.

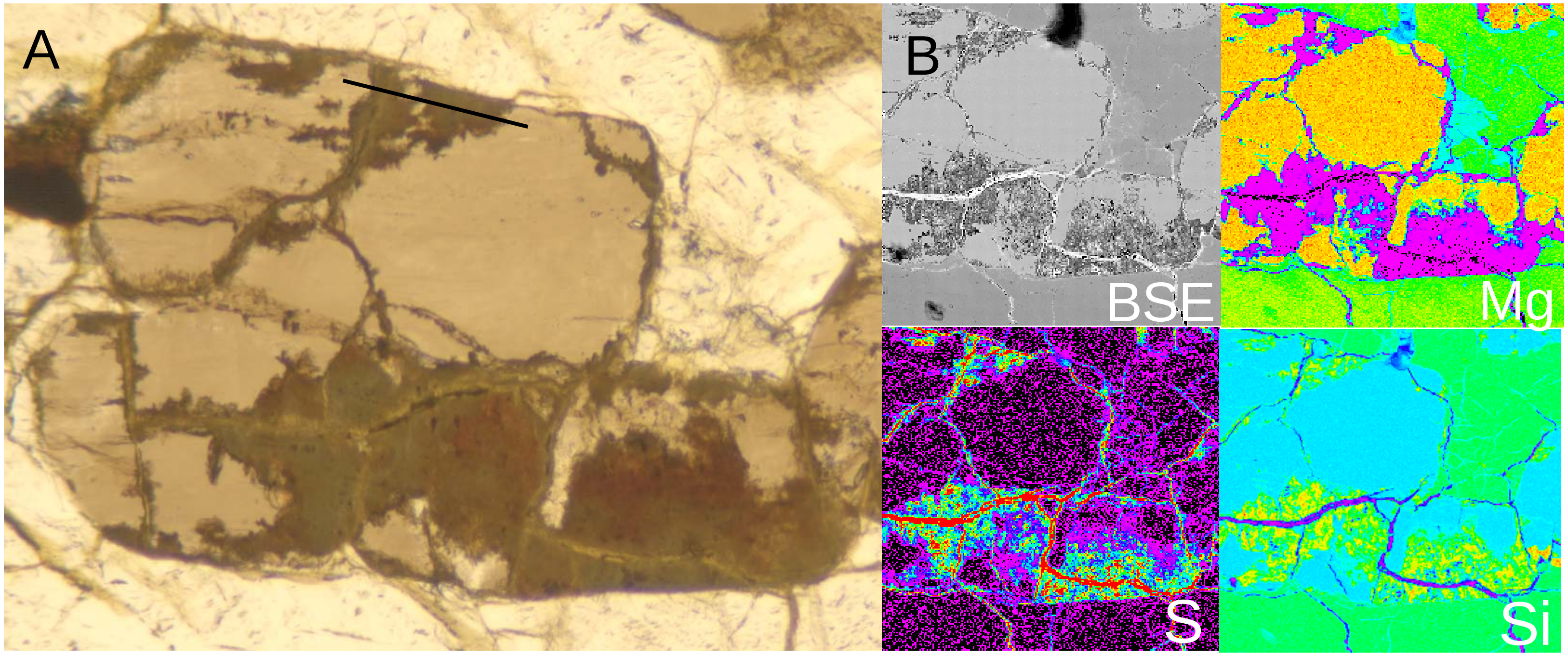

Figure 7. A) Plane-polarized light photos of the patchy olivine alteration in ALHA 77005,51 overprinted by later jarosite alteration (yellow). Compare these images with plates 246 and 247 in the Delvigne (1998) Atlas of Micromorphology of Weathering Products. B) BSE, S, Mg, and Si X-ray maps, at right, indicate the presence of jarosite, demonstrate the removal of Mg, and the retention of Si. The location of traverse 1 is indicated on the olivine at the top of picture (A), 140 µm long.

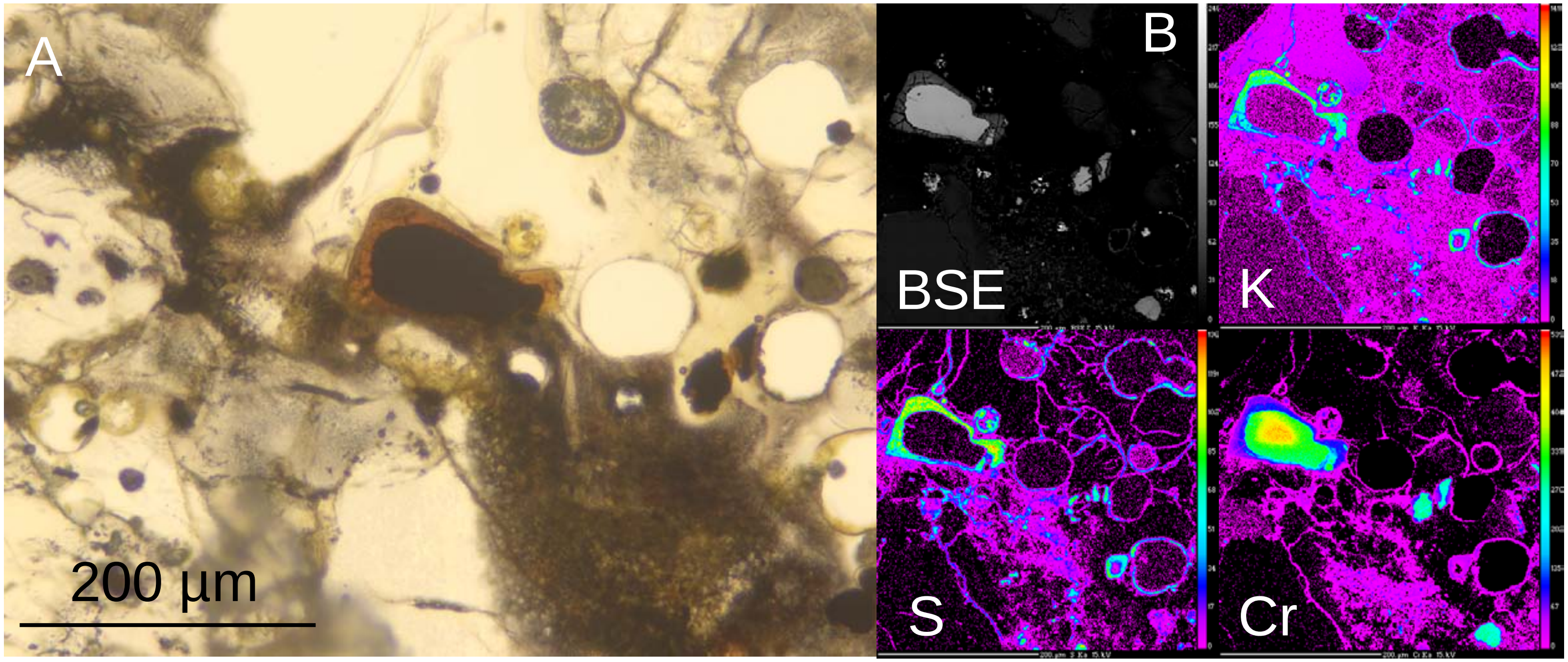

Figure 8. A) Plane-polarized light photo of a jarosite-altered chromite in ALHA 77005,51 reacting with a feldspathic glass near an impact melt vein; image suggests that the jarosite formed before the injection of the feldspathic glass (because the glass is unaltered) and that the jarosite is martian. B) BSE and S, K, and Cr X-ray maps indicating the reaction between the chromite, jarosite, and glass.

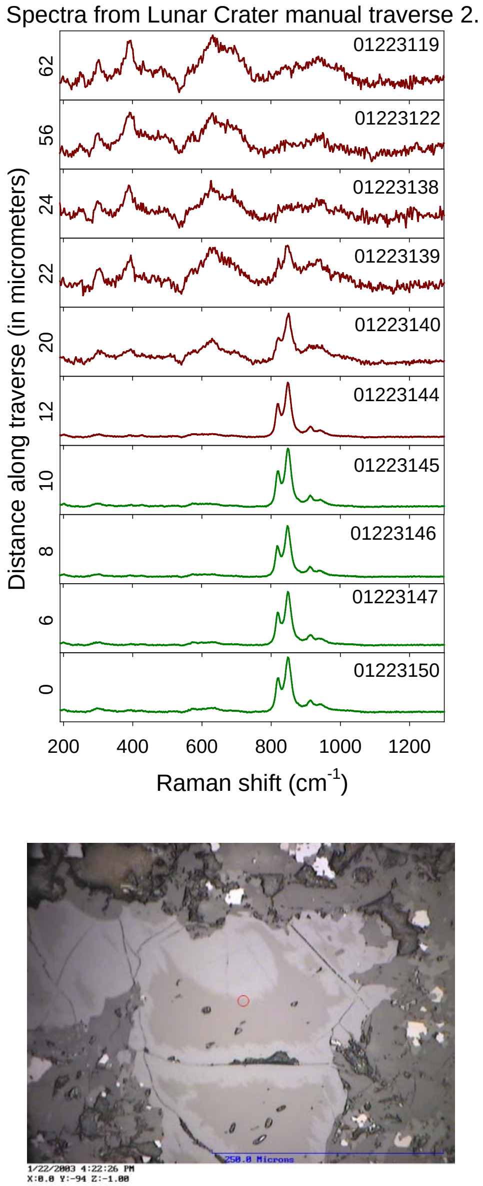

Figure 9. Reflected light image of the location of traverse 2 on the Lunar Crater phenocryst with a stack of spectra showing spectral changes across the alteration front. The direction of the traverse was normal to the alteration front at the location of the spot shown. Distances are reported according to the spacing of the Raman spectra (2 µm steps). The secondary phases present in the alteration products include goethite and a ‘polymerized’ phase (see text).

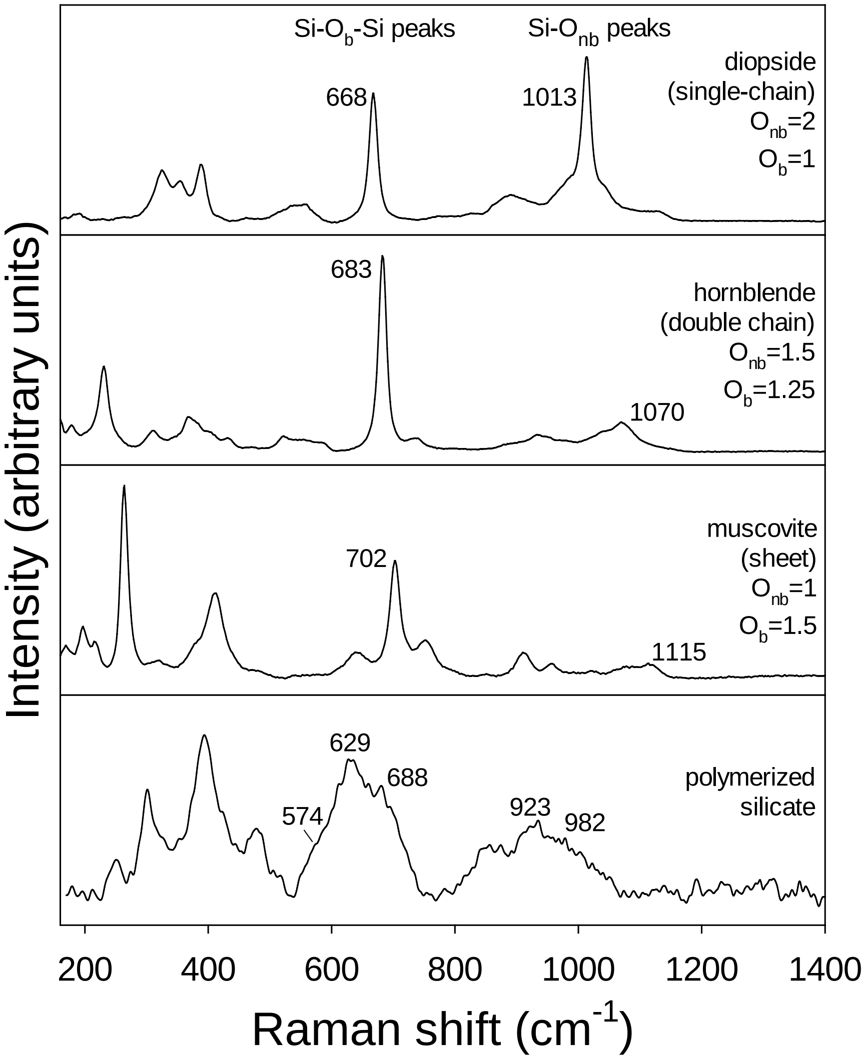

Figure 10. There is a direct correlation between the relative intensities of the Si-O_b-Si and Si-O_{nb} Raman peaks and the ratio of O_{nb}/O_b bonds. Raman Si-O_b-Si peak intensities are much stronger than those of the Si-O_{nb} peaks in silicates with $O_{nb}<2$. The peak positions of the Si-O_{nb} bands also increase as the number of O_{nb} bonds decreases. The relative peak intensities of the polymerized silicate phase in the Lunar Crater and Mauna Kea samples imply a structure whose degree of polymerization lies between that of a double-chain and sheet silicate. The ~935 cm^{-1} feature is weaker than the ~630 cm^{-1} feature, but stronger than those of phyllosilicates. The breadth of the peaks imply that the structure is poorly crystalline.

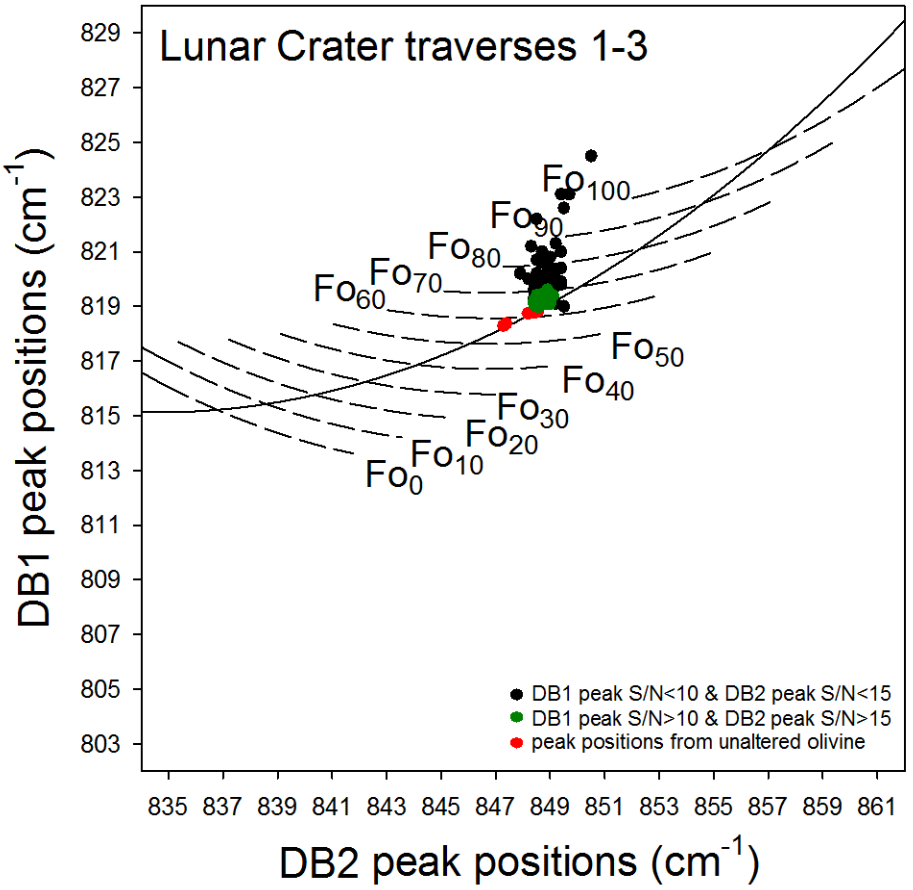

Figure 11a. Lunar Crater data points from traverses 1-3. Green data points represent the curve-fit peak positions of olivine doublets whose 820 cm^{-1} peaks have signal-to-noise (S/N) ratios > 10 and whose 850 cm^{-1} peaks have S/N ratios > 15. Black data points include doublets with peaks whose S/N ratios are < 10 and <15, respectively, but also include doublets whose 820 cm^{-1} peak has a S/N ratio > 10 but whose 850 cm^{-1} peak has a S/N ratio <15. Red data points represent doublets from spectra acquired well away from the alteration. The manner in which the data points deviate from the olivine calibration curve is due to changes in peak position due to diminshed doublet strength and to changes in the SiO_4 bonding environment with alteration.

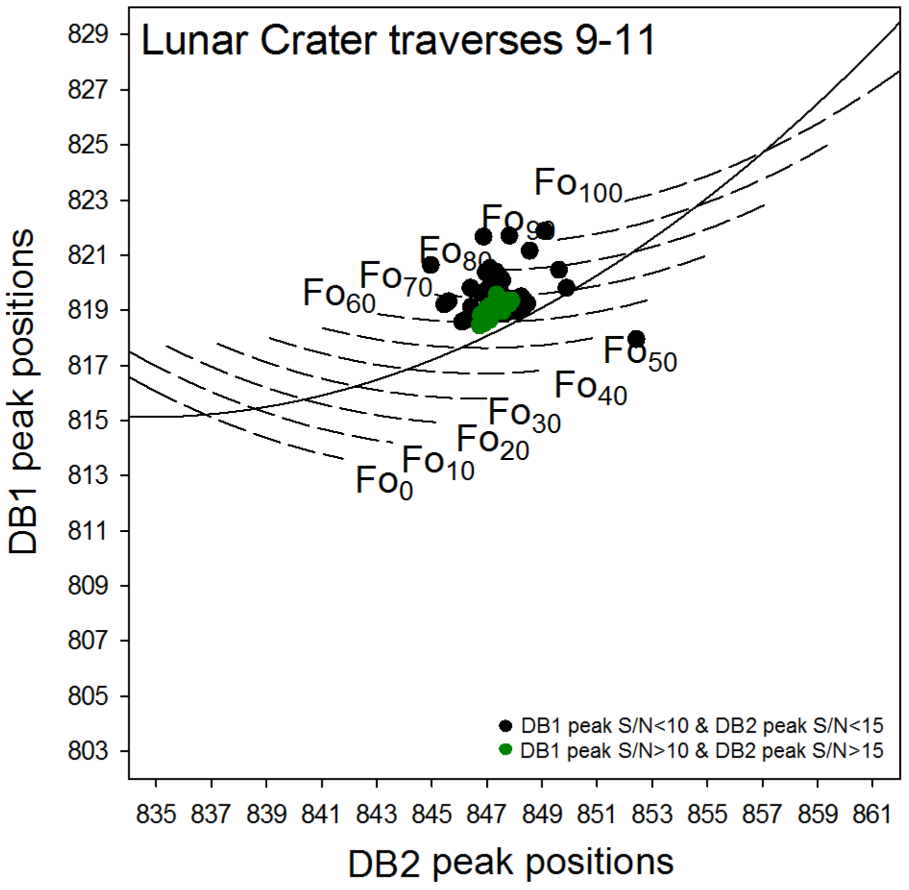

Figure 11b. Data points from Lunar Crater traverses 9 –11 (equivalent to traverses 1-3 but with the thin section rotated 90 degrees relative to the laser beam). Data demonstrate that crystal orientation influences the pattern of scattering even though alteration seems to have a preferential effect on the 820 cm^{-1} peak positions (see Fig. 21). Signal-to-noise (S/N) ratios are indicated by color as in Figure 11a; green points are from doublets with strong S/N ratios and black points from doublets with low S/N ratios.

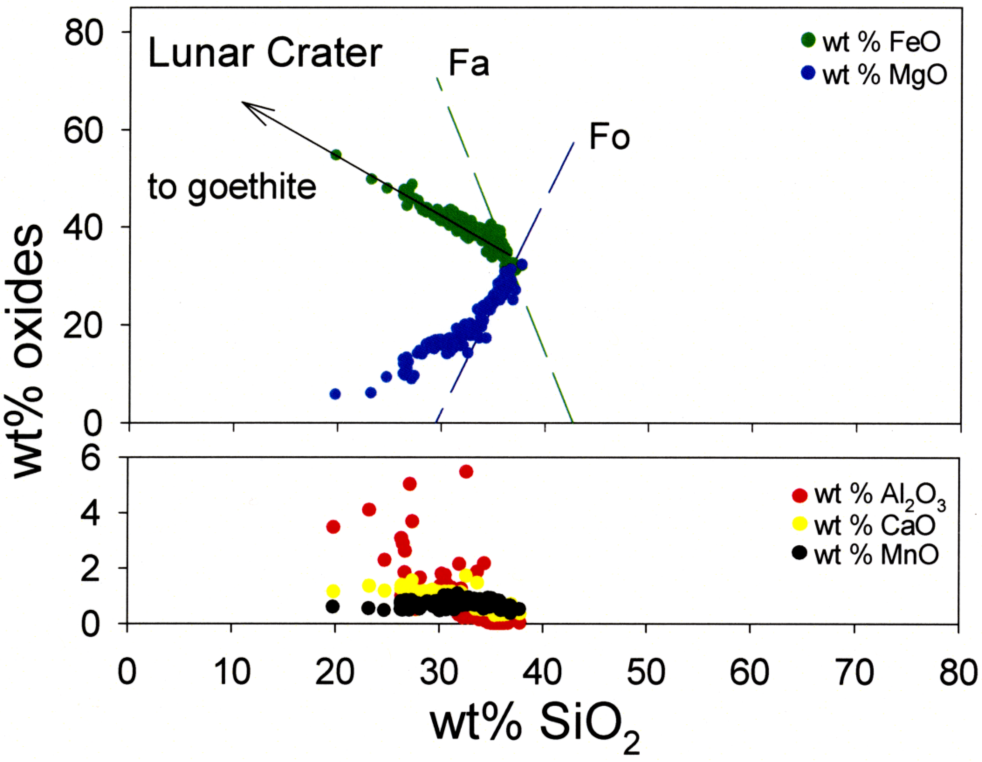

Figure 12. (A) Plot of the EMP wt % FeO and MgO vs. SiO_2 data from the Lunar Crater phenocryst (Raman traverses 1, 2, and 5-8). Unaltered olivine compositions fall along the dashed lines, data points taken in altered areas fall away from these trends (fayalite has high FeO and low MgO, forsterite has high MgO and low FeO). The FeO data points extrapolate to a value of ~81 wt % FeO at 0 wt % SiO_2 – consistent with the stoichiometric composition of goethite, while the MgO data points extrapolate to 0 wt% MgO at ~15 wt% SiO_2, which is inferred to be the approximate MgO content of the polymerized phase. (B) Plot of the minor oxide contents of the Lunar Crater analyses indicating a low influx of cations into the olivine structure during alteration (<6 wt % Al_2O_3, <2 wt % CaO or MnO). Al_2O_3 may be due to removal of carbon coat with alumina grit.

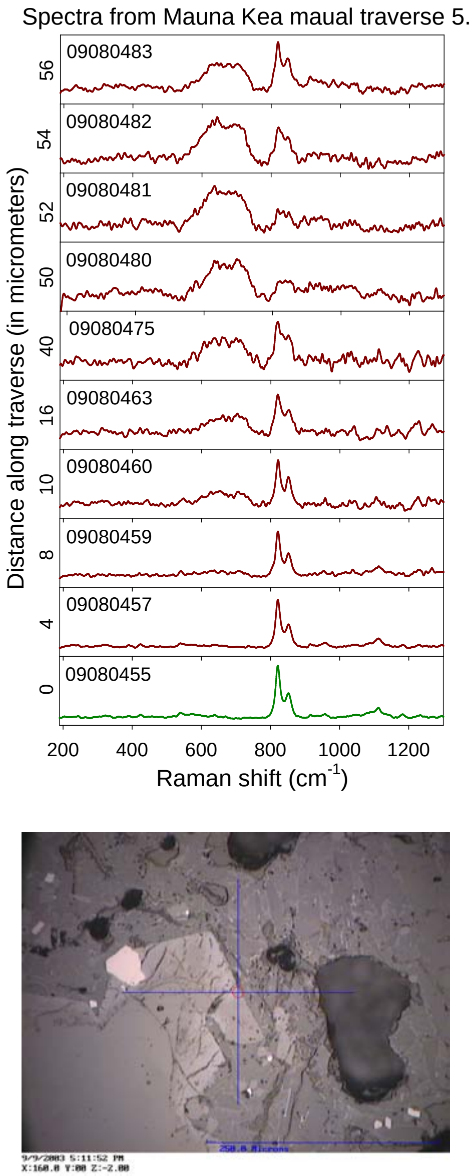

Figure 13. Reflected light image of the location of traverse 5 on Mauna Kea sample 16J-30 with a stack of spectra showing spectral changes across the front. The traverse was oriented along the x-axis of the cross-hairs as shown. Distances are reported according to the spacing of the Raman spectra (2 µm steps). Secondary phases include a polymerized silicate and traces of an iron oxide, inferred to be maghemite from the microprobe data.

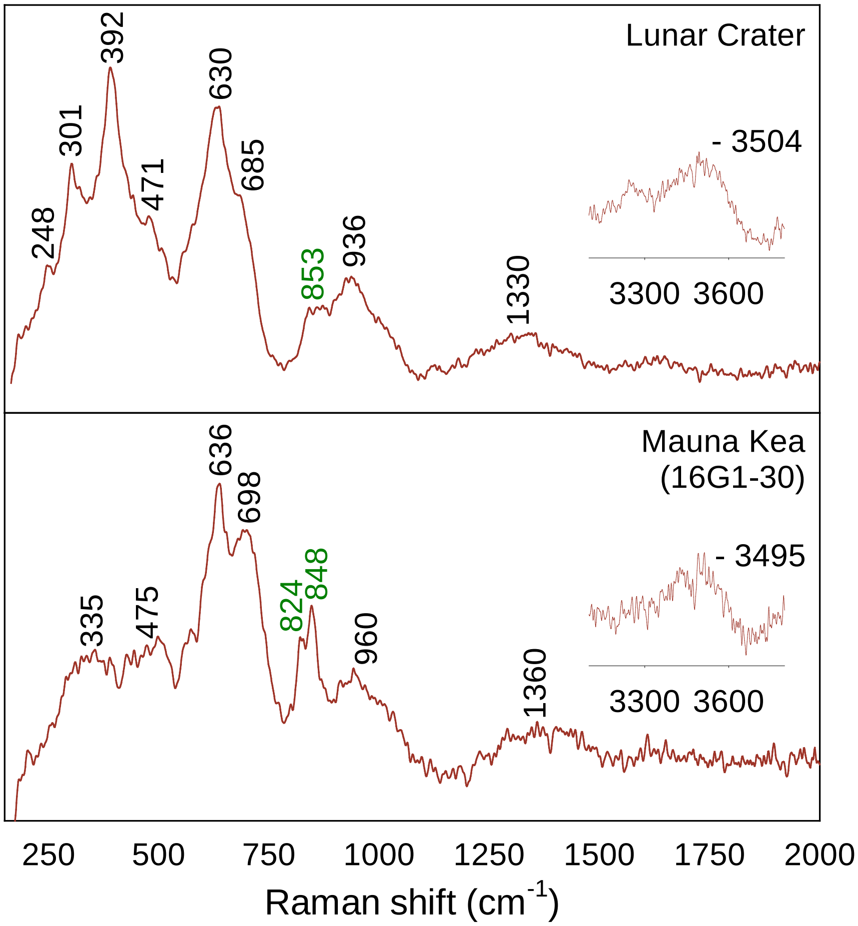

Figure 14. Comparison of "iddingsite" Raman spectra from the Lunar Crater and Mauna Kea samples. The Lunar Crater iddingsite contains distinctive goethite peaks but the Mauna Kea spectra only have weak, broad features in this region, which may belong to maghemite. The "polymerized" phase of the Mauna Kea sample has higher peak positions reflecting the more magnesian olivine compositions. Peaks labeled in green belong to olivine or an olivine 'remnant' (see text).

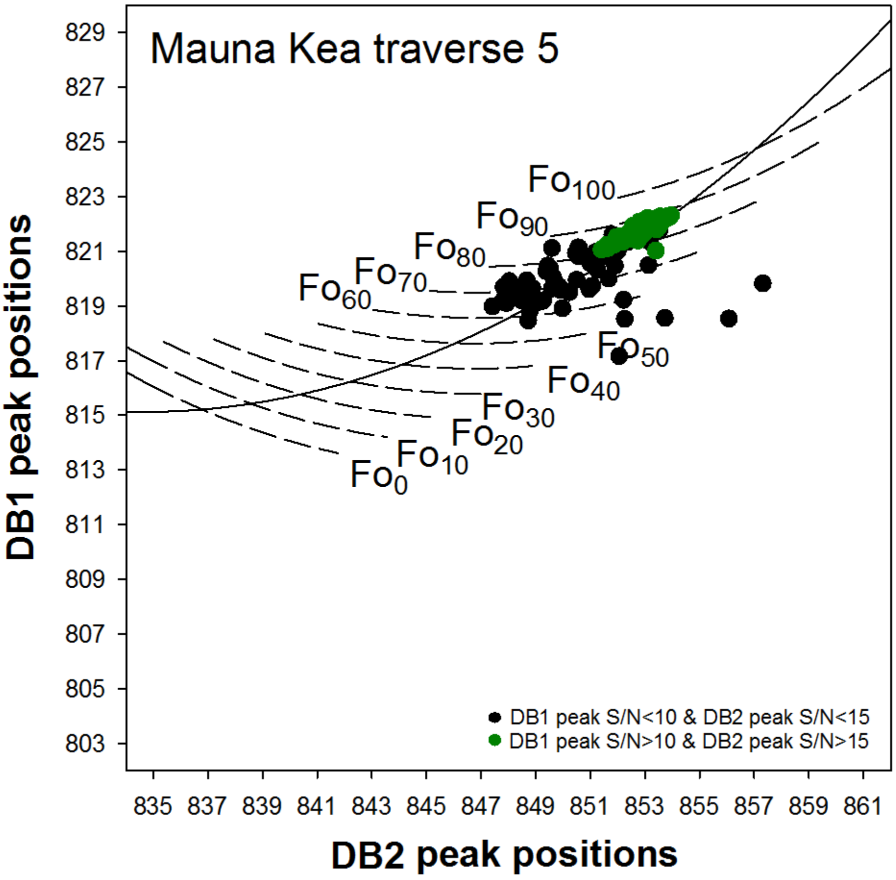

Figure 15. Mauna Kea data points from traverse 5 which crossed the olivine phenocryst shown in Fig. 6. Green data points represent the curve-fit peak positions of olivine doublets with 'good' signal-to-noise (S/N) ratios (as defined in Fig. 11). Most of the data points fall along the median curve of the calibration plot (as good Fo-Fa doublets should) and indicate zoning in the host olivine. Only a few data points scatter more than a few cm^{-1} away from the calibration curve (doublets with low S/N tend to deviate from the median curve) so we interpret the olivine structure in this sample to be less affected by alteration.

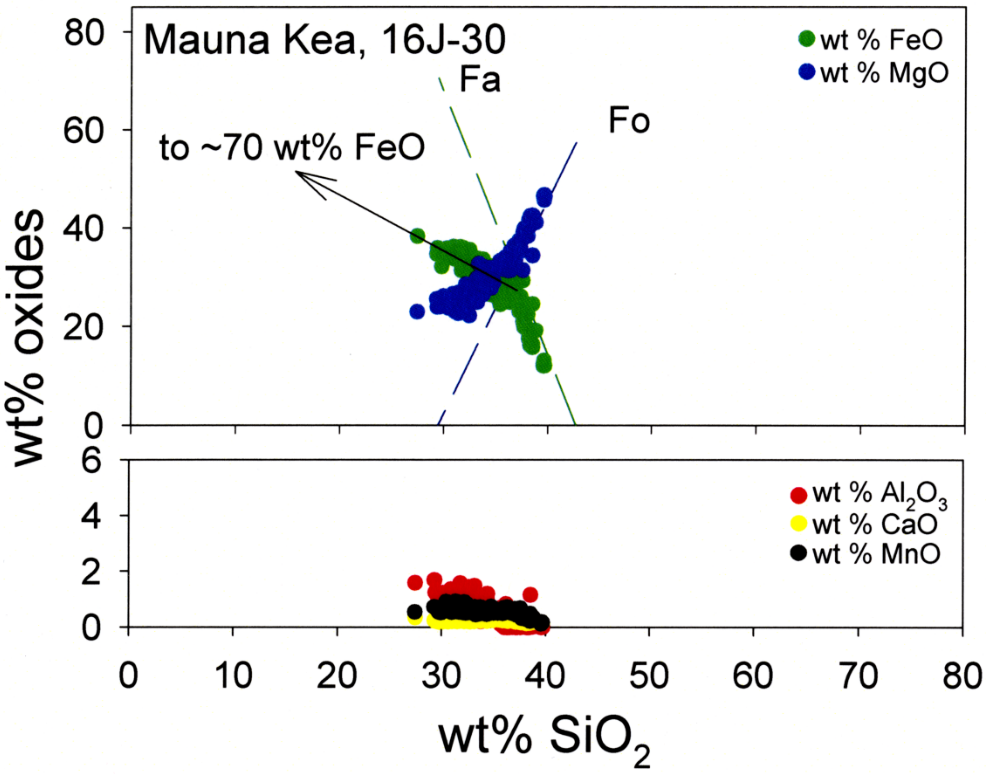

Figure 16. (A) Plot of wt % FeO and MgO vs. SiO_2 data from the EMP traverses parallel to Raman traverses 5-7 on both altered and unaltered olivine in Mauna Kea sample 16-J30. Unaltered olivine compositions fall along the dashed lines and indicate more magnesian olivine compositions than in the Lunar Crater phenocryst. The FeO data points extrapolate to a value near ~70 wt % FeO at 0 wt % SiO_2 – suggesting the presence of hematite or maghemite while the MgO data points appear to extrapolate to the origin. (B) Plot of the minor oxide contents of the Mauna Kea analyses, indicating an even lower influx of cations into the olivine structure of this sample than in Lunar Crater (all oxides <2 wt %).

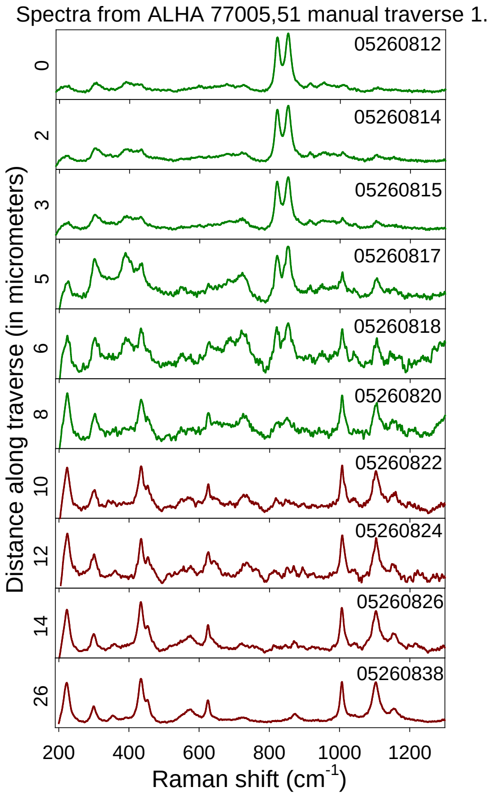

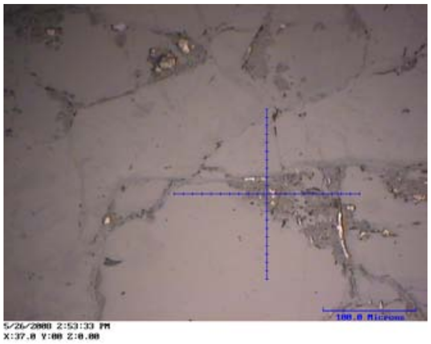

Figure 17. Reflected light image of the location of traverse 1 on ALHA 77005,51 with a stack of spectra showing spectral changes across the front into the patchy alteration (akaganéite plus polymerized silicate) and jarosite. The traverse was oriented along the x-axis of the cross-hairs as shown. Distances are reported according to the spacing of the Raman spectra (1 µm steps). The reflective materials shown in the photo above are the remaining traces of a carbon coat.

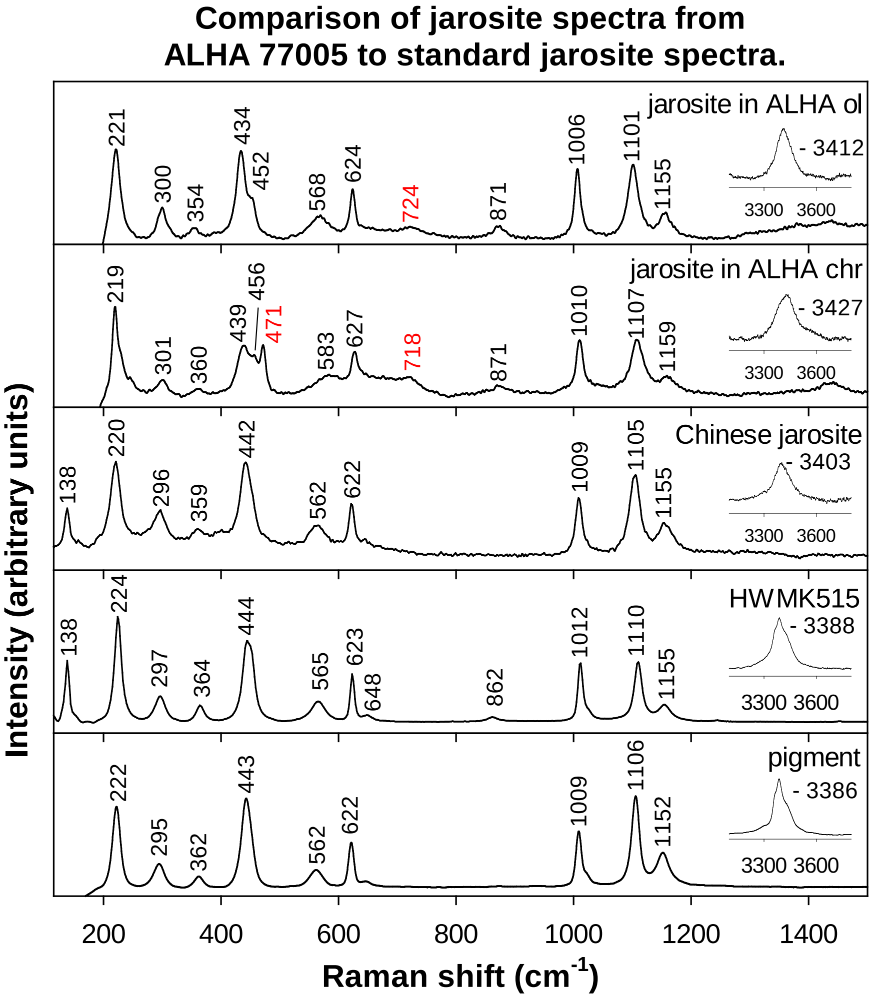

Figure 18. Comparison of the Raman spectra of the jarosite found in ALHA 77005 olivine and chromite to three standard jarosite spectra. Most peak positions are similar and vary <10 cm^{-1} between samples. Only the OH peak positions vary significantly, ~40 cm^{-1}, between the samples. The additional 471 cm^{-1} peak (labeled in red) in the ALHA 77005 chromite alteration spectrum probably belongs to elemental sulfur whose other major peak (at 219 cm^{-1}) is hidden beneath the jarosite peak at this position. The peaks near 720 cm^{-1} in the martian jarosite are probably due to akaganéite (see Fig. 17). The Chinese jarosite sample belongs to A. Wang, HWMK515 and the jarosite pigment are from D. Morris and D. Ming.

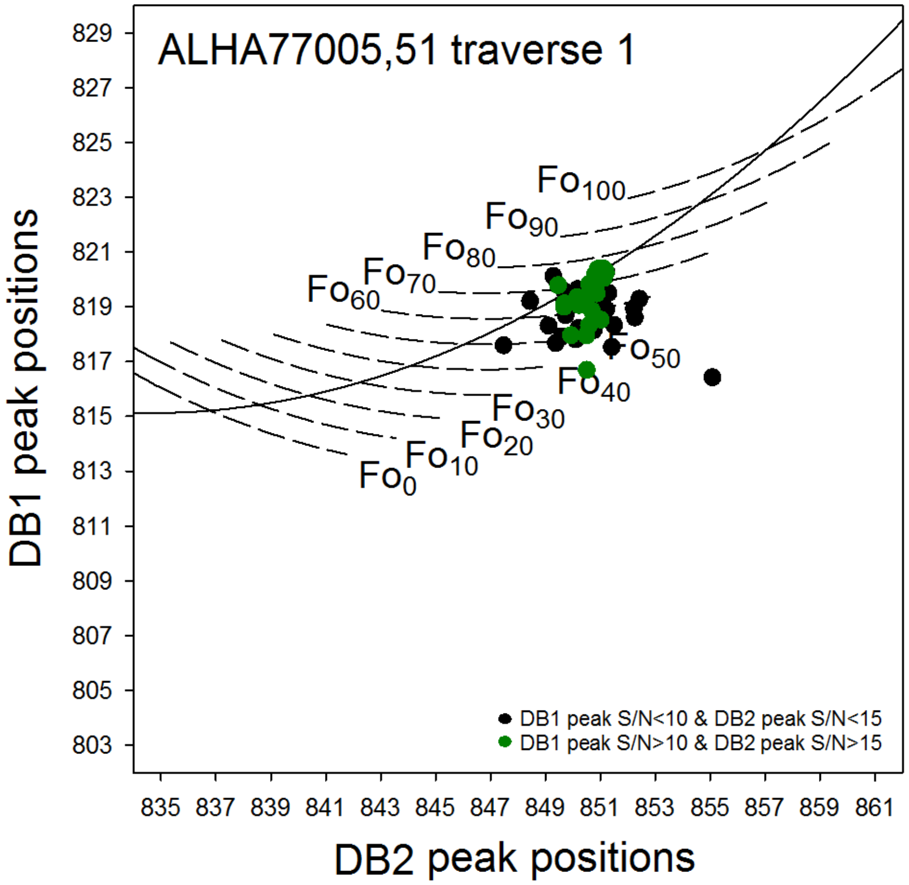

Figure 19. ALHA 77005 data points from traverse 1 on thin section ,51. Green data points represent the curve-fit peak positions of olivine doublets with ‘good’ signal-to-noise (S/N) ratios (as defined in Fig. 11). Data points fall away from the calibration curve in a manner different from those observed in the Lunar Crater phenocryst.

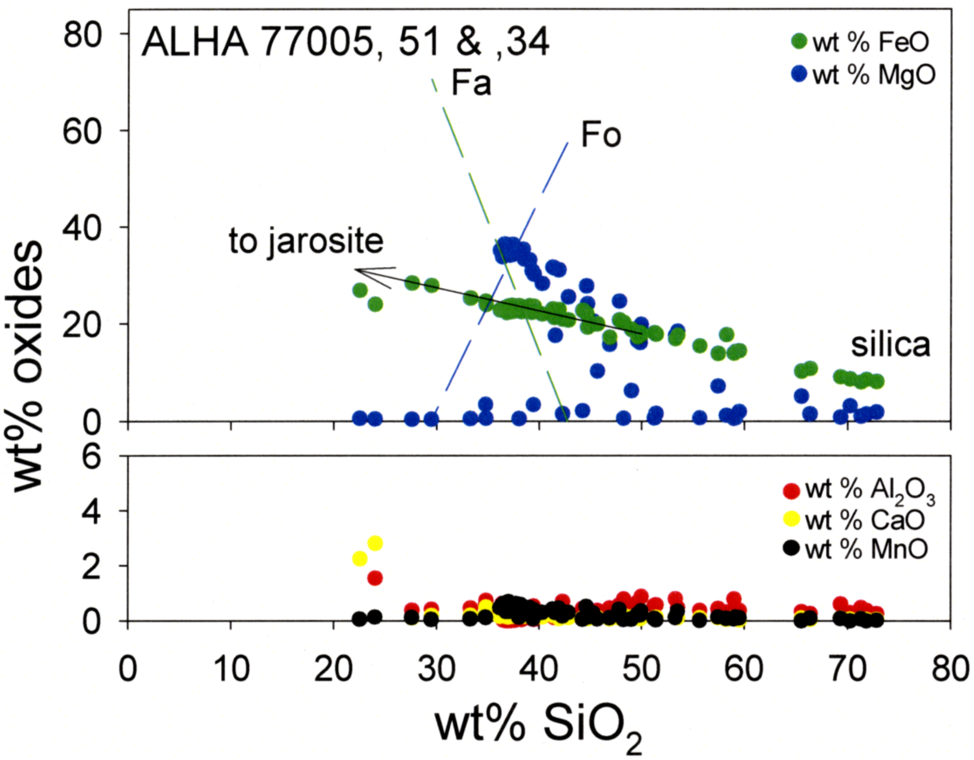

Figure 20. (A) Plot of wt % FeO and MgO vs. SiO_2 data from the EMP traverse parallel to Raman traverse 1 on an ALHA 77005 olivine. Multiple alteration phases are present; those with SiO_2 contents approaching 75 wt % indicate the presence of an amorphous silica phase. The FeO data points extrapolate to a value near ~40 wt % FeO at 0 wt % SiO_2, consistent with the presence of jarosite. Lastly, a low MgO, low SiO_2 phase is indicated and is probably equivalent to the polymerized silicate phase detected in Raman traverse 1. Because of the later jarosite, the microprobe data do not indicate the presence of akaganeite. (B) Plot of the minor oxide contents of ALHA 77005,51 analyses, indicating that the influx of cations into the martian olivine was also minor (all oxides <3 wt %).

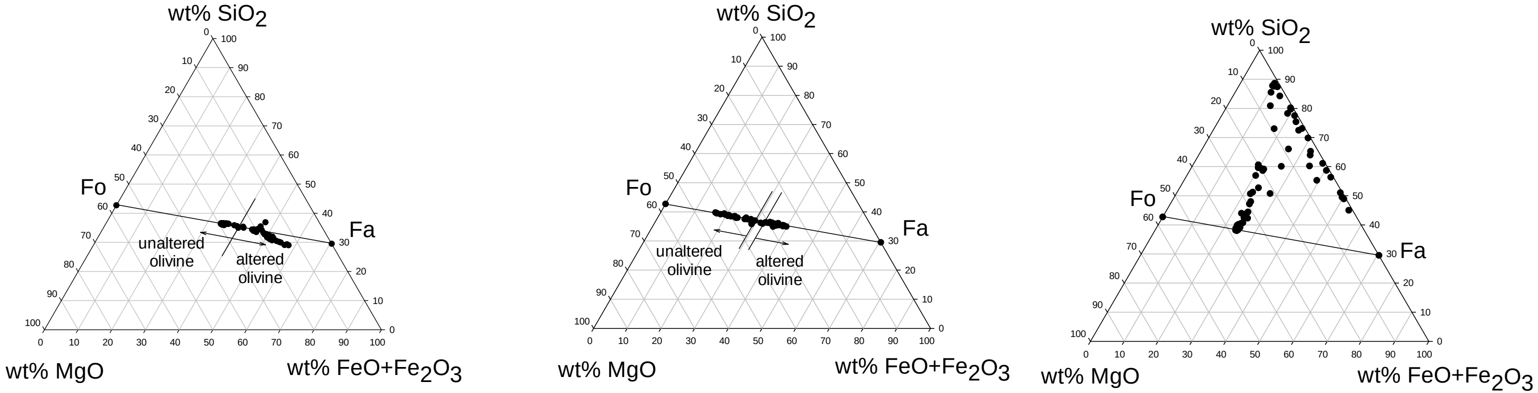

Lunar Crater EMP data
traverses 1-2, pt. check

Mauna Kea EMP data
traverse 5

ALHA 77005,51 EMP data
traverse 1

Figure 21. Normalized microprobe data from altered and unaltered olivine in all three samples. The altered olivine data points in the Lunar Crater sample start to deviate from the Fo-Fa tie line in response to the addition of OH to form goethite whereas the altered Mauna Kea data points simply follow the tie line – indicating that only Fe-oxidation has occurred. The ALHA 77005 data points scatter away from the Fo-Fa tie line indicating a loss of MgO and addition of SiO_2. There is a clean break in the Mg# between the altered and unaltered data in the Lunar Crater sample indicated by the heavy dividing line and arrows. There is some overlap in the Mg# of the altered and unaltered Mauna Kea data, however.

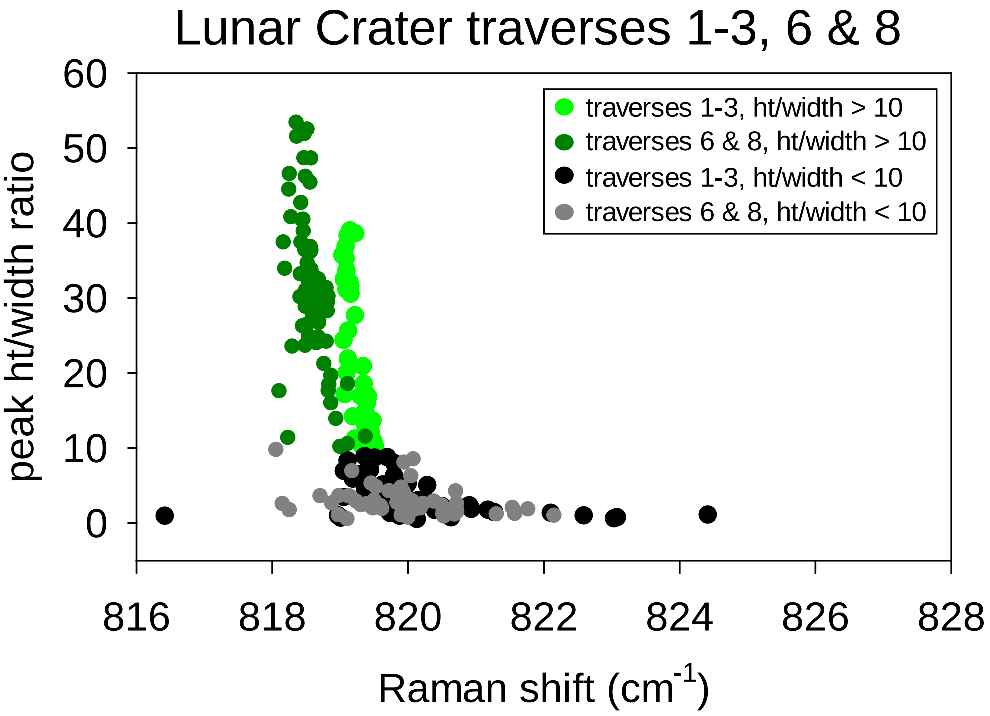

Figure 22. Peak height-to-width ratios of the 820 cm^{-1} peak vs. their Raman peak positions. Plot demonstrates that the Raman peak position of the 820 cm^{-1} peak shifts to higher peak positions as the quality of the doublet degrades through the alteration fronts of these traverses.

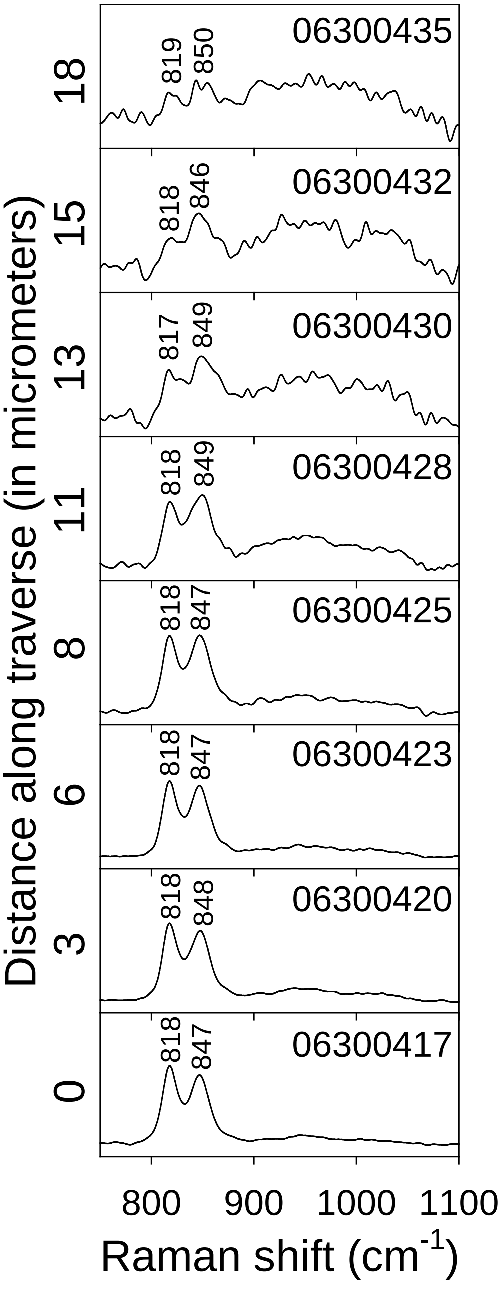

Figure 23. Spectra showing preferential alteration (i.e., preferential reduction in the peak height) of the 820 cm^{-1} peak in traverse 7 on the Lunar Crater phenocryst. The 820 cm^{-1} peak is sharper than the 850 cm^{-1} peak ahead of the alteration front but weaker than it inside the alteration.

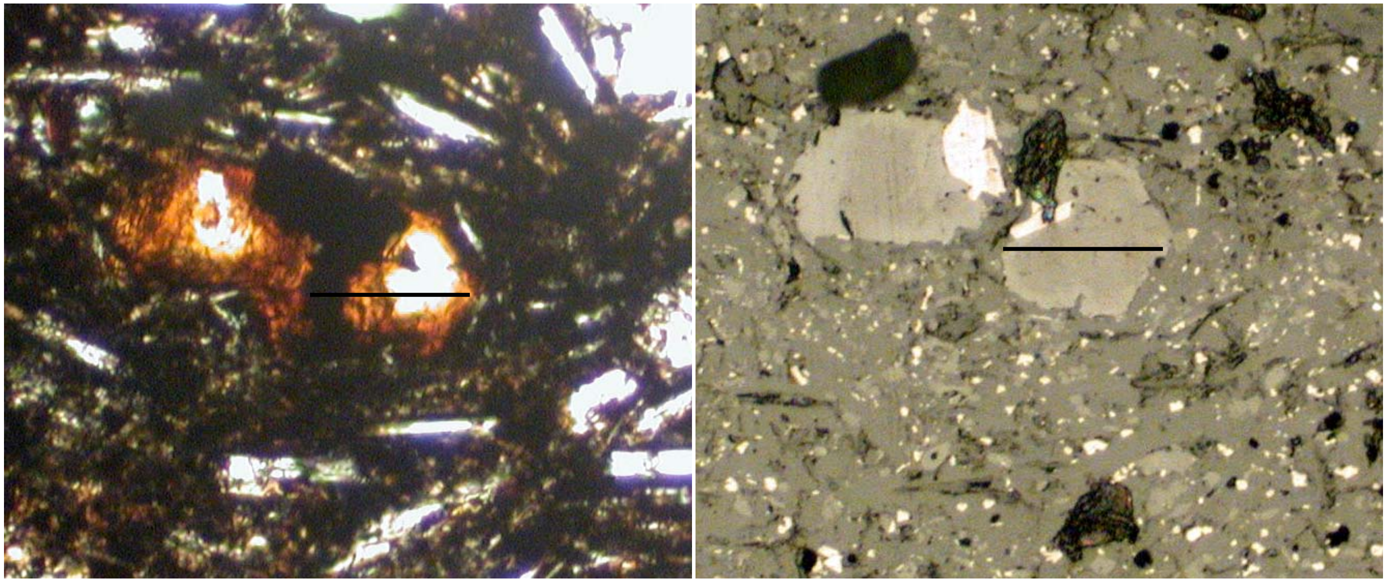

Figure 24. Image of the grains crossed by traverse 1. The traverse started at the right edge of the grain and progressed to the left edge. The reflected light image indicates only a thin rim of alteration at the upper surface of the thin section but alteration occurs at depth in the thin section and can be seen in the transmitted light photo. The alteration at depth is detected by the Raman spectra at the end of the traverse, which give the impression that the reaction occurs over a longer distance. This traverse was 74 µm long.

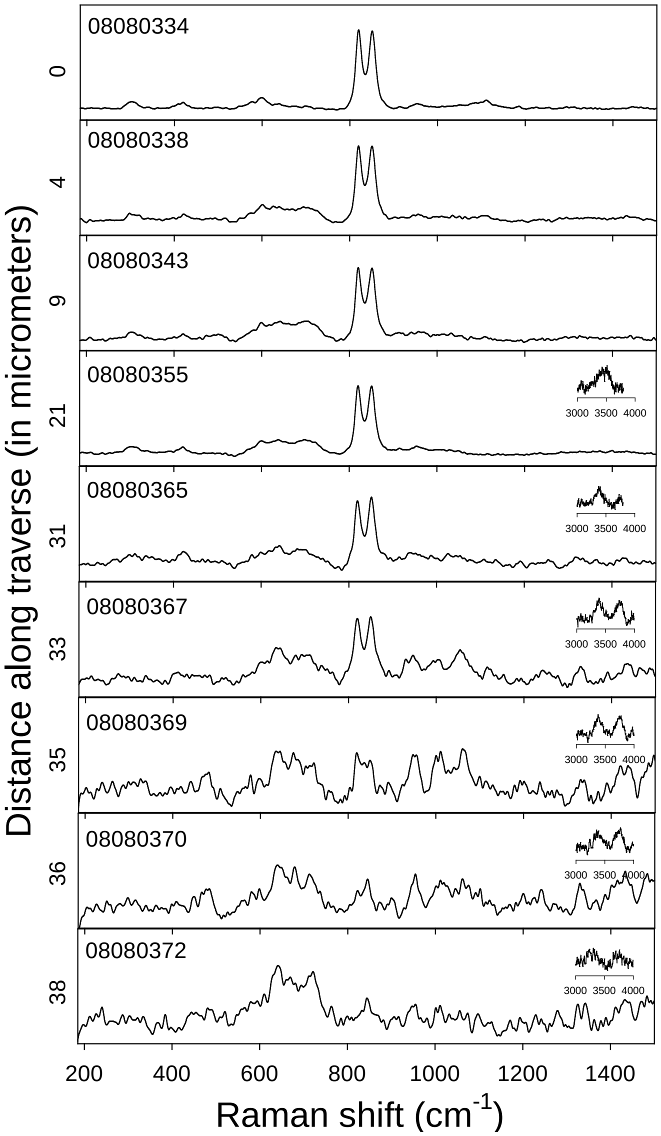

Figure 25. Spectra from the end of traverse 1 on a small Mauna Kea olivine with alteration at depth in the thin section. Figure demonstrates how the distance over which the alteration reaction appears to occur is extended when the alteration phases are detected at depth. The alteration front occurs at spectrum 08080369 according to reflected light microscopy (see Fig. 22) but the alteration phases begin to appear in the spectra 35 µm ahead of the alteration front. OH peaks are shown as insets.

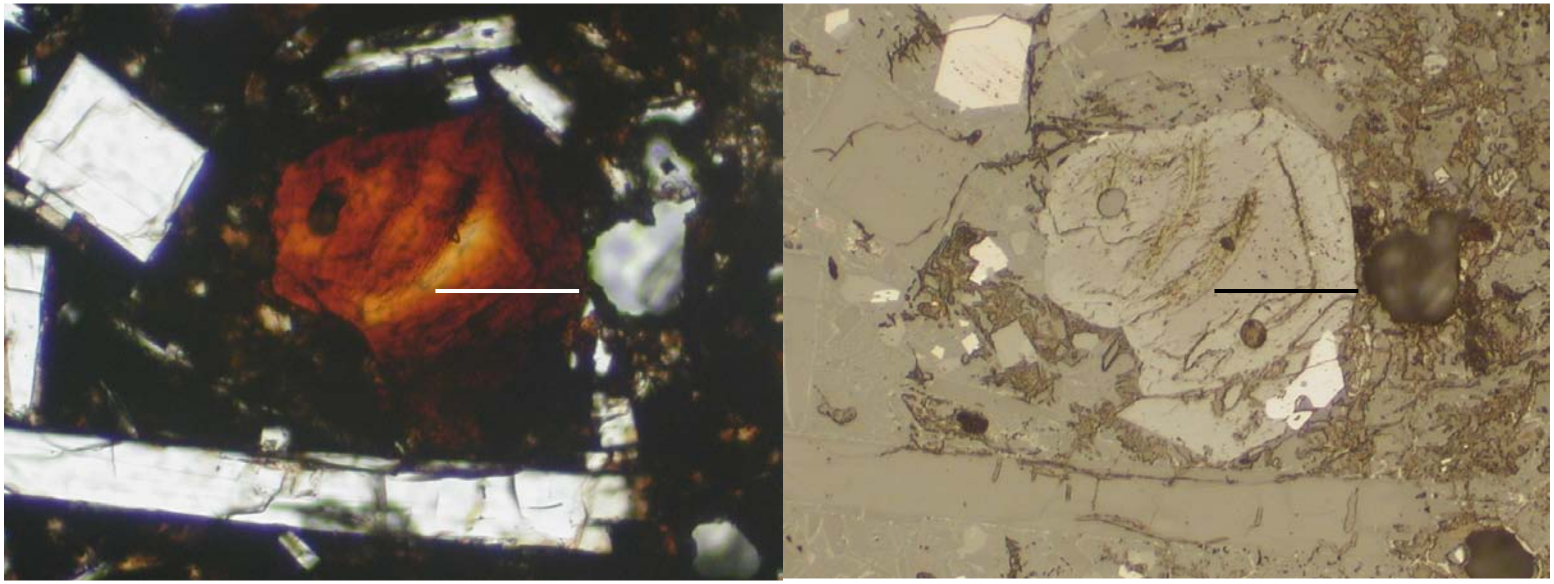

Figure 26. Transmitted light and reflected light photos of the heavily-altered olivine examined in traverse 6. The traverse began at the edge of the grain and progressed into the core. In reflected light olivine can be seen at the surface of the thin section but the transmitted light image demonstrates that alteration occurs at depth in the section. This explains why peaks of the alteration phases continue to be detected even after the traverse has passed through the alteration front into the olivine. Traverse is 118 µm long.

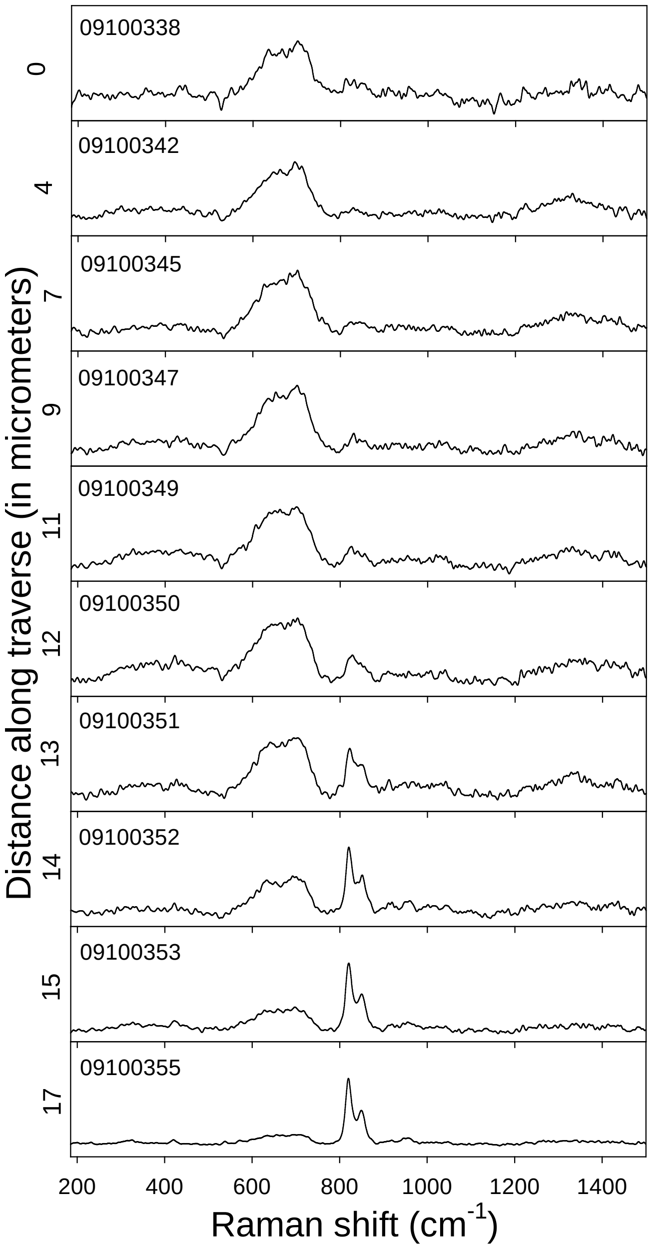

Figure 27. Traverse 6 started at the altered rim of a heavily altered olivine and traversed into the unaltered core as shown in Fig. 22. This is a stack of spectra from across the alteration front of traverse 6. The alteration front occurs at spectrum 09100350 but peaks of the polymerized silicate are observed in the olivine spectra from the core due to the presence of alteration at depth in the thin section.